721 | November 2020

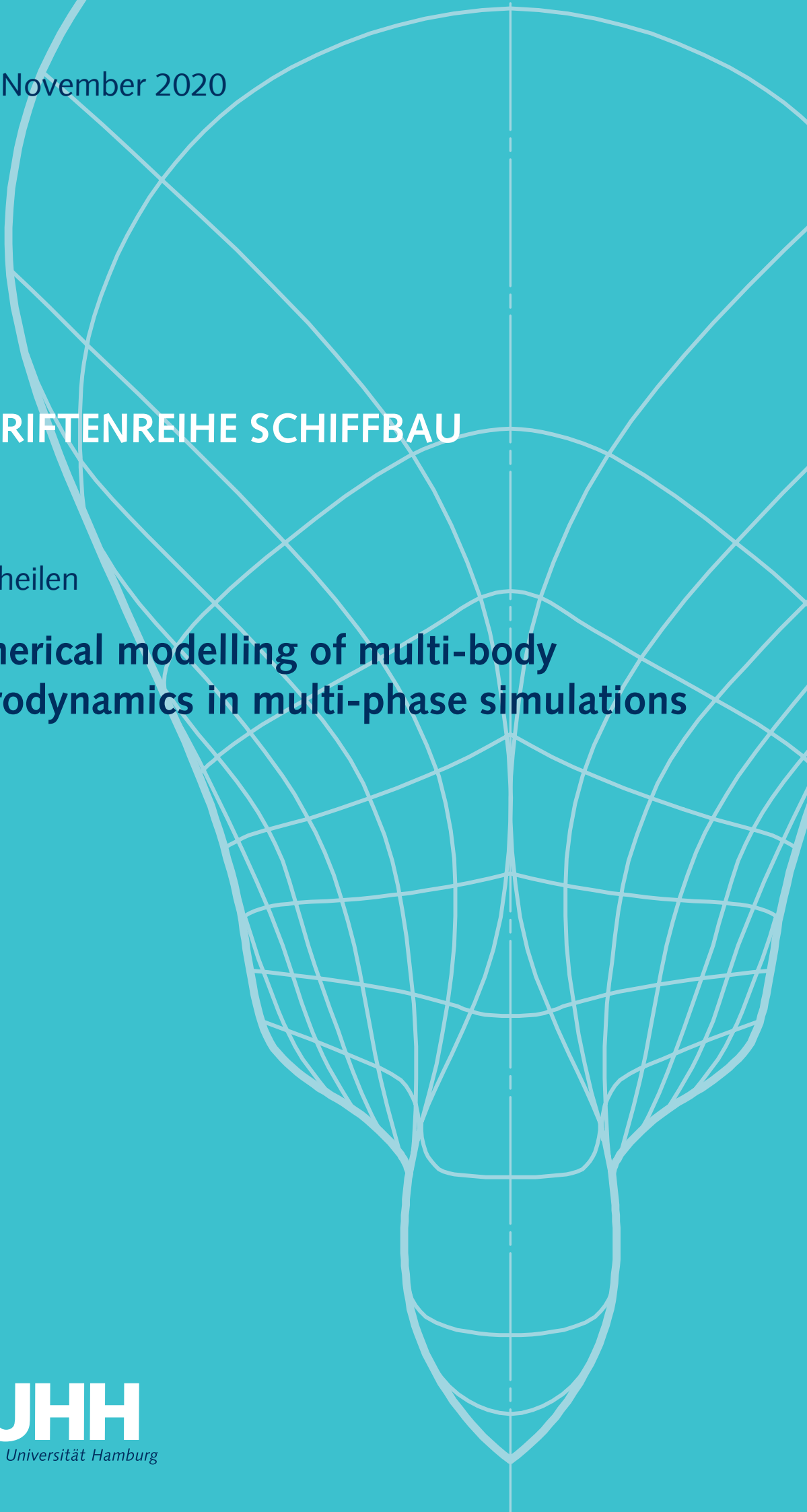

SCHRIFTENREIHE SCHIFFBAU

Elin Theilen

Numerical modelling of multi-body hydrodynamics in multi-phase simulations

TUHH
Technische Universität Hamburg

Numerical modelling of multi-body hydrodynamics in multi-phase simulations

Vom Promotionsausschuss der
Technischen Universität Hamburg

zur Erlangung des akademischen Grades

Doktor-Ingenieurin (Dr.-Ing.)

genehmigte Dissertation

von
Elin Theilen

aus
Shanghai

2020

Gutachter:

1. Gutachter: Prof. Dr.-Ing. Thomas Rung
2. Gutachter: Prof. Dr.-Ing. habil. Alexander Düster

Tag der mündlichen Prüfung:

10. Juli 2020

Vorsitzender des Prüfungsausschusses:

Prof. Dr.-Ing. Robert Seifried

Digital Object Identifier (DOI): https://doi.org/10.15480/882.3081

Publisher

Technische Universität Hamburg
Schriftenreihe Schiffbau
Am Schwarzenberg-Campus 4
D-21073 Hamburg
http://www.tuhh.de/vss

Bericht Nr. 721
ISBN 978-3-89220-721-4

Abstract

This thesis is concerned with the simulation of mechanically coupled bodies in a multi-phase environment. While the applications of such cases are very wide, they are of particular interest for offshore wind parks, where numerical investigations can support the safety margins of an operation. The computational focus of the present study is to supplement a viscous three-phase fluid-soil solver featuring the overset-grid technique by appropriate mechanical models to analyse the hydrodynamics of complex systems composed of multiple mechanically coupled bodies. A quaternion-based motion modeller featuring several basic joint elements is used to model their influence in a multi-body arrangement or the mechanical interaction between different moving parts of a structure, which can be seen as a multi-body system. Implicit seaway boundary conditions allow the use of compact domain sizes and variable headings of incident waves. Validation examples included refer to rigid links, ropes, fenders or guide frames restricting the motion in experiments, which aim to illustrate the predictive capabilities of the procedure. Finally, investigations on the simulation of a floating tug in waves, boatlanding for safe transfer, grounding of gravity foundations for wind turbines and the installation process of jack-up rigs in seaway involving structure-seabed interactions have been considered for application purposes while utilizing all features of the computational framework.

Acknowledgements

Special gratitudes go to my supervisor Prof. Dr.-Ing. Thomas Rung for the scientific supervision of my work at the Institute of Fluid Dynamics and Ship Theory of the Hamburg University of Technology. With his continuous support, guidance and enthusiasm I was always encouraged to overcome difficult challenges. I am also very grateful for the opportunity he offered me to gain various experiences during my time at the institute.

I would like to thank Michael Palm from Voith Turbo GmbH, with whom I was able to work on very interesting projects and thus was inspired to my research topic.

Many thanks go to my colleagues at the institute, who were always helpful and with whom I spent a very valuable time, in which I learned a lot about myself - professionally and personally. As an mathematician by education, the engineering approach was not always easy for me to understand. For this and for more reasons I am very happy to have always received support from my colleagues.

Further, I thank Prof. Dr.-Ing. habil. Alexander Düster and Prof. Dr.-Ing. Robert Seifried for their advice on the thesis and the interesting discussions during the defence.

Last but not least, I would like to express my special thanks to my parents, who have supported and encouraged me over all years. With their care and faith in me, I could always be confident on every path I took.
Finally, my greatest gratitude goes to Lasse, who I appreciate not only professionally as my former colleague, but above all as my husband for his love, patience and support in every possible way. I am very happy to have him and our wonderful children Frido and Phileas at my side.

Contents

Nomenclature

The general notation in this thesis for vectors is presented in bold and lower-case letters, whereas matrices are described in bold and upper-case letters. Time derivatives and second time derivatives are denoted by $\dot{()}$ and $\ddot{()}$, respectively. Subscripts are applied in different ways and will be defined in each chapter. The symbols not defined in this list, will be denoted where they appear.

Latin

A_p	matrix coefficient of the cell center variable
A_{nb}	matrix coefficient of the neighbouring variable
A_{wl}	water line area
$\boldsymbol{b}$	vector
B	ship breadth
$\boldsymbol{B}$	coupled system matrix
c	concentration
c_2	concentration of additional fluid phase
$\tilde{c}$	concentration of suspension
C	cohesion
C	spring stiffness
C_f	friction coefficient
C_m	amidships section coefficient
C_W	resistance coefficient
$\boldsymbol{d}$	distance vector
dx_{cp}	displacement of contact point
D	ship draught
D	damping coefficient

$\boldsymbol{f}$	force vector
$\boldsymbol{f}^c$	constraint reaction forces
$\boldsymbol{f}_n$	vector of normal force
$\boldsymbol{f}_{rope}$	vector of rope force
f_i	volume force coordinate
f_f	friction force
f_n	normal force
f_{max}	maximum reaction force
F_z	external z-force
$\boldsymbol{g}$	vector of external forces and moments
$\boldsymbol{g}^c$	vector of additional constraint forces and moments
$\dot{\boldsymbol{h}}$	vector of accelerations
H_s	significant wave height
k_j	wave number
l	length
eight	
H_w	wave height
$\boldsymbol{J}$	inertia tensor
J_2	second invariant of the viscous stress
k	kinetic energy
L	ship length
$\boldsymbol{L}$	matrix
m	mass
m_s	mass of vessel
m_0	initial mass
$\boldsymbol{m}'^c$	constraint reaction moments
$\boldsymbol{n}$	rotation axis
$\boldsymbol{n}$	unit vector
$\boldsymbol{n}$	normal vector
$O(h)$	truncation error
p	pressure
$\boldsymbol{p}, \boldsymbol{p}_k$	Euler parameter
$\bar{p}$	mean pressure
p'	pressure fluctuation
p'	pressure correction
p^*	intermediate pressure
p^*	initial estimation of pressure within SIMPLE

p_0	quaternion component
$p_{1,2,3}$	component of Euler parameter
P, P'	arbitrary point in space
$\mathcal{P}$	quaternion
q	source term
$\boldsymbol{q}, \boldsymbol{q}_k$	vector of Euler parameters
Q_p	source term
$\boldsymbol{r}, \boldsymbol{r}_k$	translation vector
$\boldsymbol{s}, \boldsymbol{s}'$	position vector
$\boldsymbol{s}_A$	connection vector
$\boldsymbol{s}_B$	connection vector
S	volume boundary
$\boldsymbol{S}$	rotation matrix
S_i	cell face
S_ζ	wave spectrum
t	time
t^n, t^{n-1}	current time step, previous time step
T_s	significant wave period
u_i, u_j	velocity coordinate
$\hat{u}_i$	velocity coordinate relative to the control volume velocity
u_i^g	grid velocity coordinate
$\bar{u}_i$	mean velocity coordinate
u_i'	velocity fluctuation coordinate
u_i'	velocity correction coordinate
u_i^*	intermediate velocity coordinate
u_i^*	velocity coordinate after initial estimation of pressure within SIMPLE
$\boldsymbol{v}_{cp}$	velocity of contact point
V	control volume
w_i	off-diagonal coefficients
x_i, x_j	spatial coordinate
z	vertical position

Greek

α	friction angle in the soil model
α	shape function in the seaway bounds

α	closure coefficient of the turbulence model
α	damping coefficient in the stabilization method
β	blending factor
β	magnitude of forcing
β	damping coefficient
β, β^*	closure coefficient of the turbulence model
β	resonant frequency in the stabilization method
γ	peak enhancement factor
γ	under-relaxation factor
γ	imposition coefficient
$\gamma^{\#}$	coupling term
Γ	diffusion coefficient
δ	damping ratio
δ	parameter for additional terms
δ_{ij}	unity tensor, Kronecker delta
Δt	time step interval
Δx	fender deformation
ΔS_i	cell face
ΔV_p	volume of cell
$\Delta\mu$	change of wave encounter angle
$\Delta\phi$	deflection angle
$\Delta\omega$	frequency band
ϵ	dissipation of turbulent kinetic energy
ϵ_{ij}	strain tensor
ϵ_j	wave phase
ζ	wave elevation
ζ	heave motion
ζ_{fen}	vertical motion of fender
$\hat{\zeta}_j$	wave amplitude
θ	pitch motion
θ_{cat}	pitch motion of catamaran
λ	Lagrange multiplier
λ	wave length
$\boldsymbol{\lambda}$	vector of Lagrange multipliers
Λ	scaling factor
μ	friction coefficient

μ	dynamic viscosity
μ, μ_j	wave encounter angle
μ^*	variable viscosity
μ_0	main wave direction
μ_G	viscosity of granular soil
μ_S	viscosity of the suspension layer
μ_W	viscosity of water
ν_T	turbulence eddy viscosity
ρ	density
ρ_G	density of granular soil
ρ_w	density of water
σ, σ^*	closure coefficient of the turbulence model
σ_{ij}	stress tensor
τ_{ij}	viscous stress deviator
τ_f	yield stress
τ_w	shear stress
φ	rotation angle
φ_i	generic field values
φ_t	target values
$\varphi_{1,2,3}$	wave phase
ϕ	generic variable
ϕ^n, ϕ^{n-1}	generic variable of current time step and previous time step
ϕ_p	cell center value
ϕ_{nb}	neighbouring cell value
$\bar{\phi}$	inviscid value
$\bar{\phi}_p$	inviscid value at cell center
$\phi_{1,2}$	initial deflection
Φ	constraint condition
$\mathbf{\Phi}$	vector constraint conditions
ω	specific dissipation rate of the turbulence
ω, ω_j	wave frequency
$\boldsymbol{\omega}$	angular velocity
$\boldsymbol{\omega}'_k$	local angular velocity

Operators and symbols

$\nabla_{\boldsymbol{q}} = \frac{\partial}{\partial \boldsymbol{q}}$	partial differential
$O(h)$	Landau
Fr	Froude number
Re	Reynolds number

Abbreviations and acronyms

3D	three dimensional
6DoF	six degree of freedom
BiCG	biconjugate gradient method
BiCGStab	biconjugate gradient stabilized method
BL	breaking load
CDS	Central Differencing Scheme
CEL	Coupled Eulerian-Lagrangian
CFD	Computational Fluid Dynamics
CPU	Central Processing Unit
EG	elongation
FB	Flux-Blending
FEM	Finite Element Method
FreSCo+	Free Surface Code (in-house tool)
FVM	Finite Volume Method
GMRES	generalized minimal residual method
GPGPU	General Purpose Computation on Graphics Processing Unit
HOC	High-Order Convection schemes
JONSWAP	Joint North Sea Wave Project - wave spectra
LSODE	Livermore Solver of Ordinary Differential Equations
ParMETIS	Parallel Graph Partitioning and Fill-reducing Matrix Ordering
PETSC	Portable, Extensible Toolkit for Scientific Computation
RANSE	Reynolds-Averaged Navier-Stokes equations
RAO	Response Amplitude Operator
SIMPLE	Semi Implicit Method for Pressure Linked Equations
UDS	Upwind Differencing Scheme
VCG	vertical distance from baseline to center of gravity

VoF	Volume-of-Fluid

List of Figures

List of Tables

1 Introduction

The subject matter of multi-body hydrodynamics can be widely discovered in the maritime industry. Since wind energy is one of the most promising renewable energy resources, particular attention is devoted to offshore operations in farms of wind energy plants.

Figure 1.1: *Towing, stabilizing and installation of gravity foundations (Source: Seatower AS).*

Figure 1.2: *Left: Jack-up rig elevated in sea (©Magnus Reinke). Right: boat-landing for safe transfer (Source: Turbine Transfers Ltd).*

Many related hydrodynamic application cases refer to the interplay of multiple vessels or structures. An example refers to an assessment of the offshore capability of ships, where it is important to consider their behaviour when

operating in seaway as well as in close proximity of other vessels or structures.

Another illustrative example refers to the installation of gravity foundations for offshore wind turbines, which require their towing to a desired location, subsequent flooding and sinking to seabed (see Fig. 1.1). The latter involves the interaction of the structure and multiple fluid phases, i.e. air, water and soil. Towing or escorting vessels and stabilizing structures (Fig. 1.1 middle) with towing hawsers by tugs are well-known operations, which refer to multi-body hydrodynamics [Luo et al., 2012], [Luo-Theilen and Rung, 2017], [Rung et al., 2013a]. For the final step, i.e. setting the wind turbine, jack-up rigs or self-elevating units are essential, see Fig. 1.2 left.

These offshore installations not only enable explorations of mineral deposits deep down the ground, they are also used for the installation, maintenance and removal of offshore wind farms. Many steps of construction work are carried out by means of jack-up vessels. But in the first instance, the complex procedure of installation of jack-up barges itself is considered. They are usually employed $10km - 50km$ away from the coast and in shallow water depths between $15m$ and $50m$. The mobile service platforms consist of a buoyant hull fitted with a number of movable legs. The hull of jack-up rigs enables transportation of the unit to a desired location. During transit, manoeuvring and positioning, the legs are in a raised position. To lift up the hull, the legs are lowered and penetrate into the seabed. Supported by the ground and stabilized by its own weight, jack-up rigs are able to carry out seaway- and current-tolerant operations. To ensure the performance, efficiency and safety at work, a comprehensive analysis including an assessment of operational limits has to be provided.

Next to performance issues, there also often exists an enhanced interest in the safety margins in hazardous operating conditions for multiple bodies. Elevated sea states, for example, can restrict or endanger the installation of offshore structures or even the access to them for maintenance and repair purposes. Technical staff and equipment are transferred by service vessels which often simply push their bow fender against the structure to limit the relative motion between the vessel and the foundation. A boatlanding manoeuvre is depicted in Fig. 1.2 right. A sudden slip of the fender due to wave loads can

seriously endanger a save transfer.

Accordingly, research is required to develop sound computational modelling practices which provide reliable answers at feasible numerical expenses.

1.1 Previous work

Inviscid boundary element methods are predominantly employed for transient hydrodynamic simulations. Due to the significantly smaller computational effort and the superior geometric flexibility, they are an ideal candidate for parameter studies or long term simulations at small time to solutions. For the same reasons, they are also predominantly used in industry for complex hydrodynamic multi-body simulations.

Potential flow methods for coupled rigid bodies can be found in [Nair and Kanso, 2007]. Dealing with hydrodynamic coupled multi-body systems, the response of bodies is determined by impulse response functions in [Wang et al., 2005], [Tajali and Shafieefar, 2011] and their convolutions in [Clauss and Jacobsen, 2005], [Jacobsen, 2005]. Steady-state application calculations of the prediction of towline forces in escort operations are published by [Artyszuk, 2014] and [Jahra et al., 2015]. Research publications concerning landing manoeuvres are presented in [Josse et al., 2011] and [Feikens et al., 2011], in which the methods are based on computations in frequency domain in conjunction with the impulse response function method in time domain simulations. There are only few publications on multi-body hydrodynamics using non-linear three-dimensional potential flow methods in time-domain. Simulations regarding offshore service ships based on Boundary Element methods were carried out by [González et al., 2015a] and [González et al., 2015b].
The performance and operational limits of jack-up platforms have been subject of several research activities, e.g. [DNV, 1996], [DNV, 2012], [Jensen and Capul, 2006], [Bienen and Cassidy, 2006] and [Mirzadeh et al., 2016], which usually cover either elevated or floating conditions. In [Kang et al., 2016] the towed condition of a jack-up can be found. The grounding of jack-ups or gravity foundations were analysed in [Kreuzer et al., 2014], [Qiu and Grabe, 2012] and [Bienen et al., 2015]. While many authors investigated selected parts of

an offshore installation procedure, the analysis of the entire process has not yet attracted much scientific interest which motivates the present research.

1.2 Present contributions

Even though inviscid or potential methods offer shorter analysis periods, some effects of importance for the prediction of forces and motions are either neglected or misrepresented by these approaches. The aim is to develop a procedure, which should address the following challenges:

- to reproduce realistic physical processes based upon viscous (turbulent) flow simulations.
- to support investigations on sea-keeping and manoeuvring in seaways with transient heading using compact computational and physical domains.
- to mimic the hydrodynamic and the mechanical interaction of multiple floating bodies.
- to perform monolithic simulations for three phase problems, i.e., air, water and seabed (soil).

When attention is devoted to these issues, viscous (turbulent) flow investigations are a valuable source of information. With regards to viscous flow-simulation approaches, the present research incorporates the following features

- special seaway boundary conditions follow a coupled viscous/inviscid approach, which enables prescribing boundary values by known inviscid methods to avoid wave reflections.
- a motion module based on a quaternion formulation to avoid motion singularities, known as Gimbal Lock. Rigid bodies are spatially constrained due to mechanical joints.
- the overset-grid technique provides the ability to treat large and flexible relative movements of different body (parts).

- application purposes are assigned to offshore operations including interactions within multi-phase environments.

The present study aims to convey the benefits of a mesh-based three-phase finite-volume RANS method with the numerical procedures mentioned above. All hydrodynamic and mechanical effects of a multi-body arrangement in complex offshore operations should be analysed within a monolithic simulation environment.

1.3 Layout of the thesis

The structure of the thesis is divided into the following chapters:

Chapter 2 presents the governing equations and their numerical treatment, which are used to calculate incompressible flow problems. A description of the multi-phase flow model including irregular seaway simulations is also given. The introduced seaway boundary condition enables computations on small compact domain.

Chapter 3 outlines the motion model for coupled multi-body systems. The equations of motion supplemented with additional constraint conditions are derived for basic mechanical joints. Furthermore, the overset-grids technique for large relative body motions is presented. Finally, the overall solution algorithm involving the flow solver as well as the motion modeller is illustrated.

Chapter 4 shows validation and verification cases to demonstrate the functionality and the quality of the implemented models. Examples refer to overset simulations in compact domains involving multi-body systems with combinations of mechanical couplings and three-phase flow problems.

Chapter 5 focuses on offshore application cases for wind farm industries involving the investigations of the hydrodynamic performance of tugs in seaway, boatlanding on monopiles for repair and maintenance purposes, as well as the installation of gravity foundations for wind turbines and the hydrodynamic effects during jack-up operations. All methods developed in the previous chapters are combined within a single simulation to mimic realistic ambient conditions. Furthermore, the whole dynamic operation process is of interest, in which the fluid-structure interaction and structure-soil interaction are taken into account.

Chapter 6 gives a final resume of the thesis. A summary is outlined and future research topics are suggested.

2 Flow Simulation

The numerical methods described in chapters two and three are implemented in the in-house code FreSCo+ [Rung et al., 2009], [Hafermann, 2007], which is used for the simulations presented in this thesis. The procedure solves the Reynolds-averaged Navier-Stokes equations (RANSE) for incompressible fluids using the Finite Volume Method. Multiple immiscible phases, i.e. air, water and soil, can be simulated by the Volume-of-Fluid method [Hirt and Nichols, 1981]. Computations can be carried out on unstructured, overlapping, adaptive and dynamical moving grids. The pressure is obtained from a pressure-correction scheme based on the SIMPLE algorithm. Preconditioned solvers for symmetric and non-symmetric sparse-matrix systems, e.g. GMRES, BiCG or BiCGStab, are employed from the PETSC library [Balay et al., 1997]. The parallelisation of the procedure is based on a domain-decomposition technique of usually 30 000 cells per process and can be efficiently performed up to multiple hundreds of processes. Inter-processor communication employs the MPI communication protocol and load balancing is achieved by using the ParMETIS partitioning software.

2.1 Governing equations

The computational methods are based on the integral formulations of the Navier-Stokes equations to describe the momentum of incompressible, viscous Newtonian fluids and the conservation of mass.

Continuity equation

The conservation of mass, also referred to as the continuity equation, states that the rate of the mass change in a moving (Eulerian) control volume V is

equal to the mass fluxes across the volume boundary S for solenoidal fields

$$\int_V \frac{\partial \rho}{\partial t}\, dV + \oint_S (\rho \hat{u}_i)\, dS_i = 0 \quad . \tag{2.1}$$

Herein, ρ denotes the density and $\hat{u}_i$ represents the components of the velocity for the Cartesian coordinates $i = 1, 2, 3$ relative to the control volume velocity, viz.

$$\hat{u}_i = u_i - u_i^g \quad , \tag{2.2}$$

where u_i^g denotes grid velocity.

Momentum equation

The conservation of linear momentum states that the sum of the time variation of momentum and the flux convection of momentum across the volume's surface is caused by the sum of the external acting forces. For $i, j = 1, 2, 3$ reads

$$\int_V \frac{\partial (\rho u_i)}{\partial t}\, dV + \oint_S (\rho u_i \hat{u}_j)\, dS_j = \oint_S \sigma_{ij}\, dS_j + \int_V f_i\, dV \quad , \tag{2.3}$$

where σ_{ij} is the surface stress tensor and f_i describes the volume specific forces acting on the fluid. The stress tensor can be expressed in terms of the hydrostatic pressure $p\delta_{ij}$ and a viscous deviator τ_{ij}

$$\sigma_{ij} = \tau_{ij} - p\delta_{ij} \quad . \tag{2.4}$$

Using the dynamic viscosity μ and the strain rate $\dot{\epsilon}_{ij}$ for incompressible fluids, which is trace free and thus, consists only of the symmetric part of the velocity gradient, Eq. (2.4) reads

$$\sigma_{ij} = \mu(\frac{\partial u_i}{\partial x_j} + \frac{\partial u_j}{\partial x_i}) - p\delta_{ij} \quad . \tag{2.5}$$

The viscous stresses of Newtonian fluids are modelled dependent on the strain-rate tensor sij and the dynamic viscosity m. and hence, the viscous stress coordinates are expressed by

Generic Transport equation

Using the conservation equations above, the laminar flow of viscous incompressible fluids can be described. For additional (modelled) phenomena, e.g. turbulence, additional transport equations have to be solved. The generic transport equation for a variable ϕ employs a diffusive flux (Γ denotes the diffusion coefficient) and a source term q, i.e.

$$\int_V \frac{\partial(\rho\phi)}{\partial t}\, dV + \oint_S (\rho\phi\hat{u}_j)\, dS_j = \oint_S \Gamma \frac{\partial\phi}{\partial x_j}\, dS_j + \int_V q\, dV \quad . \tag{2.6}$$

Mind, that the momentum and the continuity equation can be also expressed through (2.6). This fact is employed by the sequential numerical procedure by discretizing only one type of equation.

Turbulence model

In case of turbulent flows, e.g. high-Re flows around ships, the velocity and the pressure are frequently decomposed into a time-averaged and a statistically fluctuating part (Reynolds decomposition)

$$u_i = \bar{u}_i + u_i' \quad , \quad p = \bar{p} + p' \quad . \tag{2.7}$$

The mean values are denoted by $\bar{()}$ and fluctuations are marked with $()'$. Introducing Eq. (2.7) into the governing equation and subsequently averaging yields unclosed nonlinear correlations $\overline{u_i'\phi'}$, which are modelled by generalized Boussinesq viscosity models in the present thesis, e.g.

$$\overline{u_i'u_j'} = \frac{2}{3}k\delta_{ij} - \nu_t\left(\frac{\partial\overline{u_i}}{\partial x_j} + \frac{\partial\overline{u_j}}{\partial x_i}\right) \quad . \tag{2.8}$$

Herein, ν_T is the turbulence eddy viscosity and $k = \frac{1}{2}\overline{u_i'u_i'}$ denotes the turbulence kinetic energy. This yields statistically averaged equations, which are called Reynolds-averaged Navier-Stokes equations (RANSE). This appraoch was first proposed by Reynolds [Reynolds, 1895] and is based on the statistic properties of the turbulence.

In this thesis the $k-\omega$ turbulence model is used as the closure for the RANSE. This model predicts the turbulent properties by two additional scalar transport equations to determine k and ω, with the first being the kinetic energy of the turbulence and the second represents the specific kinetic energy dissipation rate

$$\frac{\partial k}{\partial t} + \bar{u_i}\frac{\partial k}{\partial x_i} = \tau_{ij}\frac{\partial \bar{u_i}}{\partial x_i} - \beta^* k\omega + \frac{\partial}{\partial x_i}\left[(\nu + \sigma^*\nu_T)\frac{\partial k}{\partial x_i}\right] \tag{2.9}$$

$$\frac{\partial \omega}{\partial t} + \bar{u_i}\frac{\partial \omega}{\partial x_i} = \alpha\frac{\omega}{k}\tau_{ij}\frac{\partial \bar{u_i}}{\partial x_i} - \beta\omega^2 + \frac{\partial}{\partial x_i}\left[(\nu + \sigma\nu_T)\frac{\partial \omega}{\partial x_i}\right] \quad , \tag{2.10}$$

using the closure coefficients and auxiliary relations

$$\alpha = \frac{5}{9}, \quad \beta = \frac{3}{40}, \quad \beta^* = \frac{9}{100}, \quad \sigma = \frac{1}{2}, \quad \sigma^* = \frac{1}{2} \quad . \tag{2.11}$$

The eddy viscosity follows from $\nu_T = k/\omega$. For the derivation and further details of this model, see [Wilcox, 1988].
Note, that most investigations of this thesis refer to body motions in waves, in which the flow forces are mainly pressure dominant. Thus, turbulence plays a minor part in these simulations.

2.2 Finite-Volume method

The numerical method solving the conservation equations are adopted from the Finite-Volume method (FVM). The computational domain is discretized by a finite number of contiguous and arbitrary shaped control volumes, which can move with their grid origin. All transported quantities are stored in the volume/cell center and a collocated variable arrangement is employed.
In the following, the subscript p indicates the cell center, the corresponding faces are denoted by the f and the neighbouring cell center of the faces are marked by nb.

Approximation of time derivatives

To obtain time derivatives, the A-stable implicit backward Euler method is used. The approximation is obtained by the differential quotient of the current time step t^n and the previous time steps t^{n-1}, t^{n-2} divided by time interval $h := \Delta t$. The field variable ϕ is evaluated in the volume centre p.
A first-order accurate approach is given by

$$\frac{\partial \phi}{\partial t} = \frac{\phi^n - \phi^{n-1}}{h} + O(h) \quad . \tag{2.12}$$

For a second-order accurate approximation the implicit three-time-level

$$\frac{\partial \phi}{\partial t} = \frac{3\phi^n - 4\phi^{n-1} + \phi^{n-2}}{2h} + O(h^2) \tag{2.13}$$

is considered.

Approximation of integrals

The volume integrals are approximated by the second-order accurate mid-point rule, in which the integral is calculated by the multiplication of the cell center value ϕ_p and the volume ΔV_p of the cell

$$\int_V \phi \, dV = \phi_p \cdot \Delta V_p + O(h^2) \quad . \tag{2.14}$$

Surface integrals are composed of the sum over all faces, which are also approximated by the mid-point rule

$$\oint_S \phi \, dS_i = \sum_f \left(\int_{S_f} \phi \, dS_i \right) = \sum_f \phi_f \cdot \Delta S_{i,f} + O(h^2) \quad . \tag{2.15}$$

Approximation of convective fluxes

For the calculation of the convective term, the value of ϕ at the center of the cell face has to be determined. Since the convection has a direction, there are different ways to approximate ϕ_f from the cell center values. Basically, there are symmetric and upwind based schemes. The following linear symmetric interpolation scheme provides second-order accuracy and is usually referred to as Central-Differencing-Scheme (CDS)

$$\phi_f^{CDS} = \phi_{nb} \frac{x_{i,f} - x_{i,p}}{x_{i,nb} - x_{i,p}} + \phi_p \left(1 - \frac{x_{i,f} - x_{i,p}}{x_{i,nb} - x_{i,p}}\right) + O(h^2) \quad . \tag{2.16}$$

Upwind based interpolation schemes consider the directionality of the transport mechanism, in which the upstream value is more dominant. The Upwind-Differencing-Scheme (UDS) is a well-known method by using the cell center value on the upwind side of the face

$$\phi_f \, \dot{m}_f = \phi_p \cdot \max[\dot{m}_f, 0] - \phi_{nb} \cdot \max[-\dot{m}_f, 0] + O(h) \quad . \tag{2.17}$$

Mind that this scheme is only first-order accurate. To regain the accuracy, the second-order CDS can be blended with the first-order UDS by using the blending factor $\beta \in [0, 1]$, which leads to the Flux-Blending-Scheme (FB)

$$\phi_f^{FB} = \beta \, \phi_f^{CDS} + (1 - \beta)\phi_f^{UDS} = \phi_f^{UDS} + \beta(\phi_f^{CDS} - \phi_f^{UDS}) \tag{2.18}$$

This is applied by means of a deferred correction approach, which consists of an implicitly treated UDS contribution and an explicit correction by the second addend.
Higher-order schemes (HOC) based on the same deferred correction technique can be summarised in the compact κ-scheme notation (cf. [Rung, 2008])

$$\phi_f^{HOC} = \phi_f^{UDS} + \frac{1}{2}\left[\kappa(\phi_{nb} - \phi_p) + (1 - \kappa)\, d_i \left(\frac{\partial \phi}{\partial x_i}\right)_p\right] \tag{2.19}$$

for $\kappa \in [-1, 1]$, where the right hand side terms inside the brackets are evaluated explicitly from the previous iteration or time step. Herein, d_i denotes the

i-th component of the direction vector pointing from the cell center p towards the neighbouring cell center nb. Depending on values of κ different approximation concepts can be achieved, i.e. CDS using $\kappa = 1$ or UDS for $\kappa = -1$. $\kappa = 0.5$ yields the QUICK scheme, which considers a three-point upstream quadratic interpolation [Leonard, 1979].

Approximation of diffusive fluxes

To calculate the diffusive flux, an approximation of the gradient at the cell face is required. Since the diffusion has no directionality, a second-order accurate approximation is used

$$\left(\frac{\partial \phi}{\partial x_i}\right)_f = \frac{\phi_{nb} - \phi_p}{x_{i,nb} - x_{i,p}} \quad . \tag{2.20}$$

Final algebraic equation system

By summarising the approximation equations, an algebraic equation system can be obtained for each quantity and control volume. The dependent variable ϕ at the cell centers is composed of the values at the neighbouring control volumes by using the matrix coefficients A_p, A_{nb} and the source term Q_p, viz

$$A_p \cdot \phi_p = \sum_{nb} A_{nb} \cdot \phi_{nb} + Q_p \quad . \tag{2.21}$$

Further details of the approximation schemes can be found in [Rung, 2008] and [Ferziger and Peric, 2002].

Pressure calculation using SIMPLE

While the calculation of velocity for incompressible flow problems is quite obvious, the determination of the pressure needs extra treatment. The difficulty is that the pressure is coupled to the velocity by its gradient and there

is no equation, which contains the pressure itself. Therefore, the SIMPLE-algorithm (Semi-Implicit Method for Pressure Linked Equations) [Patankar, 1980], [Ferziger and Peric, 2002] is used to solve this problem. The idea is to obtain the velocity by the momentum equation using an initial estimation p^* of the pressure field or the pressure distribution from the previous iteration. Since the resulting velocities u_i^* do not satisfy the continuity equation, p^* needs to be corrected. Therefore, following correction equations for the pressure and the velocity are introduced

$$p = p^* + p', \quad u_i = u_i^* + u_i' \quad . \tag{2.22}$$

Herein, $()^*$ denotes the intermediate field which is updated by a correction term of $()'$. The iterative process is terminated, if the corrections p' and u_i' approach zero.

2.3 Multi-phase simulation

The free-surface between two immiscible phases (e.g. air and water) is determined by the Volume-of-Fluid (VoF) method [Hirt and Nichols, 1981]. This popular technique is based on the conservation equation of the fraction $c \in [0, 1]$, which defines the volume concentration of a fluid phase in the control volume, i.e. $c = \frac{V_c}{V}$, and tracks c.

2.3.1 Equations of state

Assuming constant phase properties for two or three-phase flows the density ρ and the dynamic viscosity μ are computed by

$$\rho = \rho_1 c_1 + \rho_2 c_2 + \rho_3 c_3 \tag{2.23}$$

$$\mu = \mu_1 c_1 + \mu_2 c_2 + \mu_3 c_3 \quad , \tag{2.24}$$

where c_1, c_2, c_3 are the local volume concentrations, i.e.

$$c_1 = \frac{V_1}{V}, \quad c_2 = \frac{V_2}{V}, \quad c_3 = \frac{V_3}{V} \quad . \tag{2.25}$$

Due to

$$\sum_{i=1}^{3} V_i = V \quad \Rightarrow \quad \sum_{i=1}^{3} c_i = 1 \tag{2.26}$$

and using a simple, linear equation of state, one obtains

$$\rho = \rho_1 c_1 + \rho_2 c_2 + \rho_3 (1 - c_1 - c_2) \tag{2.27}$$

$$\mu = \mu_1 c_1 + \mu_2 c_2 + \mu_3 (1 - c_1 - c_2) \quad . \tag{2.28}$$

Substituting Eq. (2.27) into the differentiation form of Eq. (2.1) yields

$$\left[\frac{\partial c_1}{\partial t} + u_i \frac{\partial c_1}{\partial x_i}\right](\rho_1 - \rho_3) + \left[\frac{\partial c_2}{\partial t} + u_i \frac{\partial c_2}{\partial x_i}\right](\rho_2 - \rho_3) = \rho \frac{\partial u_i}{\partial x_i} \quad . \tag{2.29}$$

For immiscible fluid phases the integral form of the conservation equation states

$$\frac{\mathrm{D}c_1}{\mathrm{D}t} = 0 \quad , \frac{\mathrm{D}c_2}{\mathrm{D}t} = 0 \tag{2.30}$$

which yields the conventional simple phase volume conservation

$$\frac{\partial u_i}{\partial x_i} = 0 \quad . \tag{2.31}$$

Thus, the governing equations employed herein follow a conservative form

$$\int_V \frac{\partial c}{\partial t}\, dV + \oint_S c\, u_i\, dS_i = 0 \tag{2.32}$$

for $c = c_1$ and $c = c_2$, cf. [Völkner, 2013].

2.3.2 Soil model

The granular soil phase is modelled as a visco-plastic fluid with a variable viscosity [Völkner et al., 2015], [Ulrich et al., 2013]. The transition between the static and the visco-plastic behaviour follows from a yield criterion. If a certain yield stress is achieved, the material manifests a related plastic, strain-rate driven deformation. The soil viscosity model used for this study is based on

a combined Mohr-Coulomb and von Mises yield criterion for granular materials. According to the von Mises yield criterion for cohesive materials, yielding occurs for

$$J_2(\tau_{ij}) = 0.5\tau_{ij}\tau_{ij} = \tau_f^2 \tag{2.33}$$

with J_2 being the second invariant of the viscous stress $\tau_{ij} = 2\mu^*\dot{\epsilon}_{ij}$ with the strain rate tensor $\dot{\epsilon}_{ij}$ and τ_f denotes the yield stress. To obtain the yield stress, the Mohr-Coulomb criterion

$$\tau_f = p^* \sin(\alpha) + C\cos(\alpha) \tag{2.34}$$

for cohesive and viscous materials is applied, which depends on the relative pressure p^*, the cohesion C and the internal friction angle α. Thus, an isotropic local viscosity μ^* can be determined by the combination of both criteria, which leads to

$$\mu^* = \frac{p^* \sin(\alpha) + C\cos(\alpha)}{\sqrt{4J_2(\dot{\epsilon}_{ij})}} \quad . \tag{2.35}$$

When the strain rate vanishes in Eq. (2.35), the resulting soil viscosity gets singular and the static mode should be recovered. Therefore, an upper viscosity limit has to be introduced into the model ([Ulrich and Rung, 2012], [Ulrich et al., 2013]) and is usually assigned to $\mu_{max} = 5000 Pa\,s$. If this limitation is exceeded, non-physical material creeping can occur. This appearance can be prevented by a visco-static approach where the accelerations and velocities of affected soil particles are simply assigned to zero.

Additionally, the fluid state of the soil model is combined with a suspension layer to treat the soil-water interface. The suspension is assumed to be in the grain collisional regime, where experiments and predictions indicate a quadratic, turbulent-like relation between the shear stress and the velocity. In the limit of a vanishing suspension layer thickness the viscous stress can be treated as wall shear stress τ_w, which can be expressed in terms of the empirical friction coefficient C_f, the density of the granular soil phase ρ_G and the velocity u_i

$$\tau_w = C_f\, \rho_G\, u_i\, u_i \quad . \tag{2.36}$$

According to [Fraccarollo and Capart, 2002], C_f should be chosen from the interval of $[0.007, 0.03]$. In this range there is no remarkable difference of the suspension behaviour. Following [Ulrich et al., 2013] though, the empirical friction coefficient is defined to be $C_f = 0.01$. Finally, the viscosity of the suspension layer μ_S can be derived in the same manner as the variable viscosity of the granular soil phase

$$\mu_S = \frac{C_f \, \rho_G \, u_i \, u_i}{\sqrt{4 J_2(\dot{\epsilon}_{ij})}} \quad . \tag{2.37}$$

For the identification of the suspension layer, the suspension concentration $\tilde{c}$ is introduced [Völkner, 2013], [Völkner et al., 2015]. $\tilde{c}$ is derived from the volume fraction of the granular soil and is defined in the range of $0.3 < \tilde{c} < 0.6$ within the suspension layer (cf. [Ulrich et al., 2013]). Using the following linear interpolation, the transition from the viscosity of the suspension layer to either water's viscosity μ_W or the viscosity of the granular soil μ_G can be modelled

$$\mu^* = \begin{cases} \mu_W + \frac{\mu_S - \mu_W}{0.3} \tilde{c} & \text{for } \tilde{c} \leq 0.3 \\ \mu_S & \text{for } 0.3 < \tilde{c} < 0.6 \\ \mu_S + \frac{\mu_G - \mu_S}{1 - 0.6} (\tilde{c} - 0.6) & \text{for } 0.6 \leq \tilde{c} \leq 0.99 \end{cases} \quad . \tag{2.38}$$

Mind, that $\tilde{c}$ should not exceed 0.99. In this case the viscosity of the granular soil would be calculated by the suspension model. Obviously, the viscosity of the suspension layer is physically limited by the viscosity of the water and and the granular soil.

2.3.3 Irregular seaway

One way to obtain natural seaways in numerical simulations is achieved by superposing harmonic wave components of different amplitudes and frequencies. Since the phases of each wave component varies in space and time, an irregular wave field can be developed. Using the wave number k_j, the amplitude $\hat{\zeta}_j$, the frequency ω_j, the encounter angle μ_j and the phase ϵ_j, the wave elevation ζ can be defined by the time t as following

$$\begin{aligned}\zeta(x,y,t) &= \sum_{j=1}^{N} \mathrm{Re}\left[\hat{\zeta}_j\, e^{i(\omega_j t - k_j(x\cos\mu_j + y\sin\mu_j)+\epsilon_j)}\right] \\ &= \sum_{j=1}^{N} \hat{\zeta}_j\, \cos(\omega_j t - k_j(x\cos\mu_j + y\sin\mu_j) + \epsilon_j)\end{aligned} \tag{2.39}$$

The formula (2.39) requires the specification of the unknown parameters of each single wave components, i.e. amplitudes of the frequencies $\hat{\zeta}_j(\omega_j)$, the phases k_j and wave encounter angles μ_j.

The whole process exhibits a stochastic and an empirical part. The amplitudes of the frequencies are derived empirically from the seaway characteristics. Usually, they are provided by seaway spectra using empirical data. The spectra describe the wave energy distribution over the wave frequencies and encounter angles. However, they do not provide any informations about the phases and the frequencies. To describe the wave elevation of Eq. (2.39) the phases have to be chosen randomly in the range of $[0, 2\pi]$. Thus, various sea states can be generated, that have the same essential characteristics due to the same underlying spectrum.

The JONSWAP spectrum was formulated based on wide measurements at the German North Sea coast. Following [Clauss et al., 1988], the spectrum is defined as

$$\begin{aligned} S_\zeta(\omega) &= \frac{5.32\xi}{\pi}\,\frac{H_s^2}{\omega}\,\exp\left\{\frac{-32.29}{\pi}\,\xi\right\}\cdot\gamma^p, \\ \xi &= \left(\frac{\pi}{T_s\,\omega}\right)^4, \qquad p = \exp\left\{-(\omega T_s/5.32-1)^2/(2b^2)\right\} \\ b &= 0.07 \text{ for } \omega\,T_s < 5.32 \;\;,\;\; b = 0.09 \text{ for } \omega\,T_s \geq 5.32 \end{aligned} \tag{2.40}$$

Herein, H_s and T_s denote the significant wave height and the significant wave period, respectively. γ defines the peak enhancement factor and for $\gamma = 3.3$ the JONSWAP seaway is fully developed.

The Pierson-Moskowitz-spectrum

$$S_\zeta(\omega) = \frac{5.57\xi}{\pi}\,\frac{H_s^2}{\omega}\,\exp\left\{\frac{-22.28}{\pi}\,\xi\right\} \tag{2.41}$$

is an alternative to the JONSWAP spectrum which is also implemented in FreSCo+. In Fig. 2.1 a comparison of the two wave spectra is illustrated.

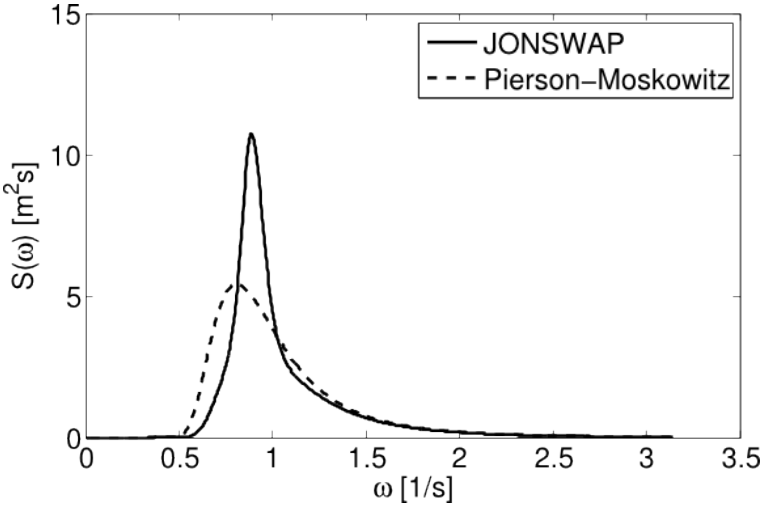

Figure 2.1: *Illustration of the implemented wave spectra based on JONSWAP and Pierson-Moskowitz.*

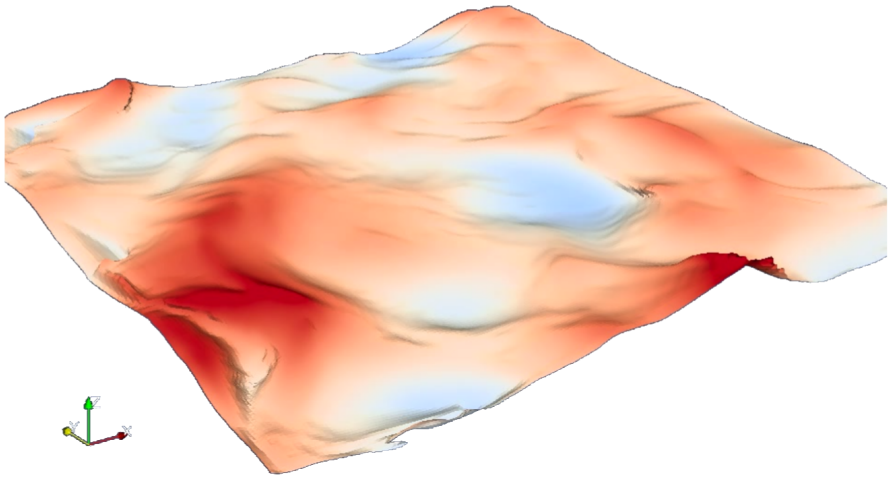

Figure 2.2: *Application of the JONSWAP spectrum (200 wave components; $H_s = 7m, T_s = 6s$).*

The distribution of the wave energy over the different encounter angles μ can be achieved by applying a $\cos^2$-distribution of the energy in a range of $[\mu_0 - \pi/2, \mu_0 + \pi/2]$ about the main wave direction μ_0. Thus, the wave spectrum for each wave direction can be formulated as

$$\mathcal{S}_\zeta(\omega, \mu) = S_\zeta(\omega) \cdot \frac{2}{\pi} \cdot \cos^2 \{\mu_0 - \mu\}, \text{ for } -\pi < \mu < \pi \quad . \tag{2.42}$$

Using S_ζ as the averaged wave energy for each range of wave frequency and encounter angle, the wave elevation can be obtained by the superposition of every single seaway component

$$\zeta(x, y, t) = \sum_{j=1}^{N} \sqrt{2\mathcal{S}_\zeta(\omega_j, \mu_j)\Delta\omega\Delta\mu}\, \cos(\omega_j t - k_j(x \cos\mu_j + y \sin\mu_j) + \epsilon_j) \quad . \tag{2.43}$$

The application of at least 40 wave components is recommended for the simulation of a natural seaway. Furthermore, the wave frequencies need to have an irrational ratio to each other to avoid replications. Therefore, the wave frequencies as well as the wave phases are chosen arbitrarily within the uniformly distributed frequency bands of $\Delta\omega$ and $[0, 2\pi]$ for each wave component. Fig. 2.2 exemplifies a natural seaway based on a fully developed JONSWAP spectrum ($\gamma = 3.3$) using a significant wave height of $H_s = 7m$ and a significant period of $T_s = 6s$. 20 different wave frequencies are distributed over 10 different wave directions which leads to 200 different wave components.

2.3.4 Seaway boundary condition

The accurate prediction in the viscous manoeuvring and seakeeping simulations of floating bodies in waves requires appropriate dissolved computation meshes which are able to capture the incident wave field towards the body. For transient problems the time-step is limited due to the Courant number and has to be even decreased for grid refinements. Due to computation efficiency, seekeeping simulations on small and physically compact domain are of interest.

Another essential challenge of viscous computations is the appropriate definition of the seaway boundary condition. The wave field downstream of the body is reflected at the outlet boundary of the domain and thus, cause wave disturbance close to the body. To improve the quality of result and suppress these reflections at the far field, numerical damping is required. A common way of damping downstream of the body is achieved by the introduction of a damping zone, also referred to as numerical beach. Usually, the grid is stretched towards the boundary. The idea is to damp the waves by numerical diffusion before they reach the boundary. In this case, a simple boundary condition, e.g. hydrostatic pressure condition for calm water, can be applied. Since the magnitude of grid stretching is wave dependent and thus unknown, long damping zones need to be applied.

When attention is drawn to offshore operations, the involved manoeuvring vessels, i.e. tugs or jackups, are exposed to waves which change their direction in time. In these cases inlet and outlet boundaries can no more be distinguished from each other. Since the grid-based damping method is inherent directionally, it is not applicable for offshore operation simulations. A remedy to this problem is given by [Gentaz et al., 2004]. They proposed a coupled viscous/inviscid method, which assigns the incident wave field to an inviscid description. The technique used in this thesis assumes that viscous and diffraction effects are negligible in the vicinity of the far-field boundaries. Thus, viscous methods for the computation of the wave field close to the body can be coupled to inviscid approaches for the simulation of the far-field, see [Wöckner et al., 2010]. The coupling of both methods employs an implicit manipulation of the coefficient matrix by forcing the viscous solution field ϕ to be imposed by known inviscid values $\overline{\phi}$ for large values $\beta\alpha^2$, viz.

$$\left[1+\beta\alpha^2\right] A_p\phi_p = \sum_i^{nb} A_i\phi_i + S_\phi + A_p\,\beta\alpha^2\,\overline{\phi}_p \quad . \tag{2.44}$$

In Eq. (2.44) A_p denotes the diagonal coefficients, A_i refers to the contributions of the neighbouring cells and S_ϕ describes the source term. At the transition of the viscous and inviscid area, two non-dimensional parameters β and α are employed to manage the imposition. The shape function α restricts the manipulation to a buffer-zone of usually half wave length. As illustrated

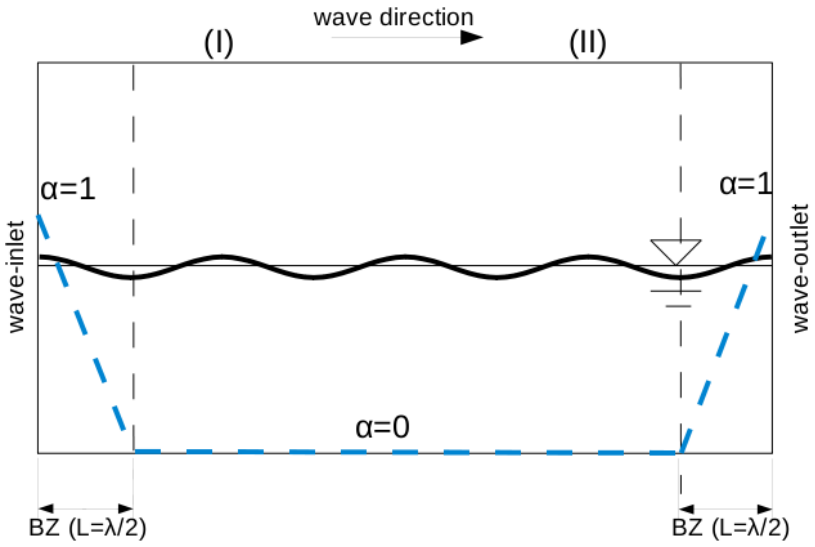

Figure 2.3: *Illustration of the buffer-zone (BZ) and the shape function parameter α, [Wöckner et al., 2010].*

by the blue dashed line in Fig. 2.3, α is zero within the computational domain and increases to unity at the boundaries. The parameter β represents the magnitude of forcing which is usually of order $\beta \approx 10^{-3}$. Further details on this coefficient is described in [Wöckner et al., 2010].

This method is applied to all far-field boundaries of the domain and utilizes Dirichlet-conditions for the momentum and the free surface equations based on the prescribed values $\overline{\phi}$. The latter can be easily obtained from linear wave theories, i.e. Airy-theory.

Generally, this coupled method has no directionality and can be applied for sea-keeping simulations of floating bodies featuring wave directions which change in time, e.g. in turning test cases.
Mind, that the neglect of the wave diffraction is only acceptable at sufficient distances from the body. The inviscid solution is time-dependant regarding wave direction and amplitude. Using the linear wave theory, different wave components can be superposed for the simulation of natural seaway. According to our experiences, the linearity does not affect the quality of the solution, since non-linear effects are quickly recaptured by the Navier-Stokes equations in the inner part of the domain.

3 Multi-body Systems

Floating bodies and their motions have a significant influence on the surrounding wave field and vice versa. In this chapter the equations of motions are presented. Special attention is drawn towards mechanically coupled multi-body systems. Various mechanical joints and their constraint conditions are presented, which can be applied to an arbitrary number of bodies. Furthermore, the overset-grid technique is described. The solution algorithm of the flow solver FreSCo+ including the motion model is given at the end.

3.1 Rigid motion

The most common way to describe the angular orientation of a rigid body in a three dimensional space is the use of Euler angles. They represent three composed elementary rotations of a body-fixed local coordinate system referring to an initial global system. Each elementary rotation allows one degree of freedom. In such an arrangement the effect of a Gimbal Lock can occur, see Fig. 3.1, when two axes are driven into a parallel configuration, which "locks" the system into a rotation in a degenerate two-dimensional space. To avoid this singularity and ensure that each motion is uniquely defined, quaternions are employed for the motion modeller and will be discussed in the following. Constraint forces due to mechanical couplings are also derived using quaternions.

3.1.1 Euler parameter

According to Euler's theorem, the general displacement of a body can be accomplished by a single rotation about a suitable axis over a certain an-

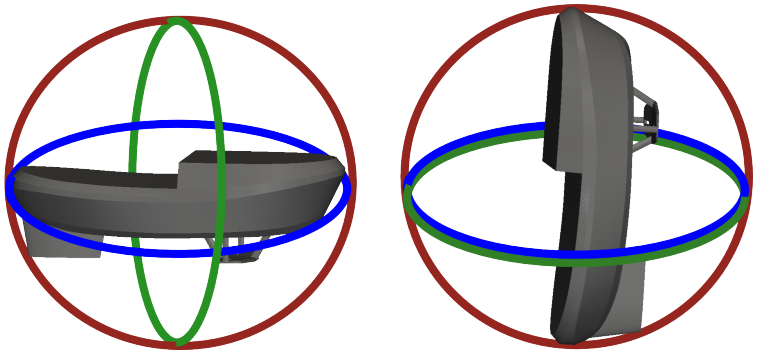

Figure 3.1: *Left: no Gimbal Lock. Right: Gimbal Lock.*

gle [Nikravesh, 1988], [Goldstein, 2006]. Therefore, it is reasonable to use a representation of the coordinate transformation in terms of the parameters of this single rotation, i.e. the angle of rotation and the direction cosines of the orientational axis of rotation. A quaternion is a collection of four real parameters, of which the first is considered as a scalar and the other three as components of a vector in three-dimensional space:

$$\mathcal{P} = (p_0 \;\; \boldsymbol{p}) = (p_0 \;\; p_1 \;\; p_2 \;\; p_3)^T \in \mathbb{R}^4 \tag{3.1}$$

Denoting $\boldsymbol{n}$ in Fig. 3.2 as the rotation axis and φ as the rotation angle, the transformation of vector $\boldsymbol{s}'$ into $\boldsymbol{s}$ represents a rotation from P' to P

$$\boldsymbol{s} = \boldsymbol{s}' \cos\varphi + \boldsymbol{n}(\boldsymbol{n} \cdot \boldsymbol{s}')(1 - \cos\varphi) + \boldsymbol{n} \times \boldsymbol{s}' \sin\varphi \; . \tag{3.2}$$

Introducing the following Euler parameters [Bauchau, 2011], [Nikravesh, 1988]

$$p_0 = \cos\frac{\varphi}{2}, \;\; \boldsymbol{p} = (p_1 \;\; p_2 \;\; p_3)^T = \boldsymbol{n} \cdot \sin\frac{\varphi}{2} \quad \text{and} \quad \|\boldsymbol{n}\| = 1 \tag{3.3}$$

a rotation matrix $\boldsymbol{S}$, according to [Wittenberg, 2008], can be derived from Eq. (3.2), which obeys to

$$\boldsymbol{s} = (2\,p_0^2 - 1)\,\boldsymbol{s}' + 2\,\boldsymbol{p}\,(\boldsymbol{p} \cdot \boldsymbol{s}') + 2\,p_0\,\boldsymbol{p} \times \boldsymbol{s}' = \boldsymbol{S} \cdot \boldsymbol{s}' \tag{3.4}$$

and reads

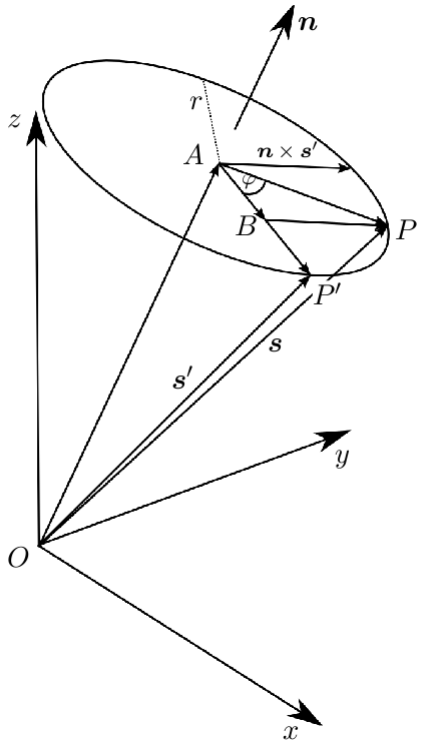

Figure 3.2: *Rotation from P' to P.*

$$\boldsymbol{S} = 2 \begin{bmatrix} (p_0^2 + p_1^2) - \frac{1}{2} & (p_1\,p_2 - p_0\,p_3) & (p_1\,p_3 + p_0\,p_2) \\ (p_1\,p_2 + p_0\,p_3) & (p_0^2 + p_2^2) - \frac{1}{2} & (p_2\,p_3 - p_0\,p_1) \\ (p_1\,p_3 - p_0\,p_2) & (p_2\,p_3 + p_0\,p_1) & (p_0^2 + p_3^2) - \frac{1}{2} \end{bmatrix} .$$

Based on Eq. (3.3), it is

$$\mathcal{P}^T\mathcal{P} = \cos^2\frac{\varphi}{2} + \boldsymbol{n}^T\boldsymbol{n}\sin^2\frac{\varphi}{2} = 1 \quad . \tag{3.5}$$

Hence, $\boldsymbol{S}$ consists of unit quaternions. Thus, the resulting vector $\boldsymbol{s}$ is a unitary transformation of $\boldsymbol{s}'$, see Eq. (3.4). To state the angular velocity vector $\boldsymbol{\omega}$ in the same manner, the following relation can be obtained from time derivative of $\mathcal{P}$ (cf. [Nikravesh, 1988]):

$$\dot{\mathcal{P}} = \frac{1}{2}\,\boldsymbol{L}^T \cdot \boldsymbol{\omega}' \tag{3.6}$$

with

$$\boldsymbol{L} = \begin{bmatrix} -p_1 & p_0 & p_3 & -p_2 \\ -p_2 & -p_3 & p_0 & p_1 \\ -p_3 & p_2 & -p_1 & p_0 \end{bmatrix} .$$

By means of the obtained relations above, a body's equations of motion can be easily transformed into quaternions and thus avoid Gimbal Locks.

3.2 Multi-body interaction

An equation system of k unconstrained bodies is achieved by stringing together all six equations of motion for the translation and rotation of single unconstrained bodies:

$$\begin{aligned} m\,\ddot{\boldsymbol{r}} &= \boldsymbol{f} \\ \boldsymbol{J}' \cdot \dot{\boldsymbol{\omega}}' + \boldsymbol{\omega}' \times (\boldsymbol{J}' \cdot \boldsymbol{\omega}') &= \boldsymbol{m}' \end{aligned} \tag{3.7}$$

into the $6k$ system

$$\boldsymbol{A} \cdot \dot{\boldsymbol{h}} + \boldsymbol{b} = \boldsymbol{g} \ . \tag{3.8}$$

Herein, the $6k \times 6k$ matrix $\boldsymbol{A}$ contains all masses m and local inertia tensors $\boldsymbol{J}'$. The acceleration vector $\dot{\boldsymbol{h}}$ inherits the second derivative of the translation vector $\boldsymbol{r}$ of the body-fixed coordinate system relative to the global frame and the local angular accelerations $\dot{\boldsymbol{\omega}}'$. External forces $\boldsymbol{f}$ and local external moments $\boldsymbol{m}'$ are combined in vector $\boldsymbol{g}$. The vector $\boldsymbol{b}$ reads $(0,\ \boldsymbol{\omega}'_1 \times (\boldsymbol{J}'_1 \cdot \boldsymbol{\omega}'_1), \cdots,\ 0,\ \boldsymbol{\omega}'_k \times (\boldsymbol{J}'_k \cdot \boldsymbol{\omega}'_k))$ and comprises all quadratic velocity terms of each body 1 to k.

In a multi-body system, the bodies are coupled to each other or to their surroundings by mechanical joints. A mechanical joint constraints the motion of an attached body and consequently influences the movement of the adjacent bodies in a coupled system. Thus, the equations of motion are supplemented by additional constraint conditions. In this thesis, focus is given to scleronomic and holonomic constraints, in which constraint conditions are not formulated

as inequalities. Furthermore, they are independent on time and independent on velocity or acceleration variables. Hence, the constraint equations are formulated in terms of the spatial position variables of the body.

3.2.1 Coupled bodies

Since spatial position vectors are expressed by quaternions, each condition equation Φ is a function of a combined vector containing the translation $\boldsymbol{r}_k$ and the Euler parameters $\boldsymbol{p}_k$ of each body $k = 1, 2, .., n$:

$$\boldsymbol{q} = \begin{bmatrix} \boldsymbol{q}_1 \\ \boldsymbol{q}_2 \\ \vdots \\ \boldsymbol{q}_n \end{bmatrix} \in \mathbb{R}^{7n}, \quad \boldsymbol{q}_k = \begin{bmatrix} \boldsymbol{r} \\ \mathcal{P} \end{bmatrix}_k = (x \;\; y \;\; z \;\; p_0 \;\; p_1 \;\; p_2 \;\; p_3)_k^T \quad . \tag{3.9}$$

For n bodies, m constraint conditions can be formulated as

$$\boldsymbol{\Phi} \equiv \boldsymbol{\Phi}(\boldsymbol{q}) = \begin{bmatrix} \Phi_1(\boldsymbol{q}) \\ \vdots \\ \Phi_m(\boldsymbol{q}) \end{bmatrix} = \boldsymbol{0} \quad , \tag{3.10}$$

which leads to a coupled system of $6n - m$ degrees of freedom. Each constraint equation also has to be fulfilled on velocity and acceleration levels, i.e.

$$\dot{\Phi} = \boldsymbol{\nabla}_{\boldsymbol{q}} \Phi \cdot \dot{\boldsymbol{q}} \qquad = \boldsymbol{0}\,, \tag{3.11}$$

$$\ddot{\Phi} = \boldsymbol{\nabla}_{\boldsymbol{q}} \Phi \cdot \ddot{\boldsymbol{q}} + \boldsymbol{\nabla}_{\boldsymbol{q}} \left(\boldsymbol{\nabla}_{\boldsymbol{q}} \Phi \cdot \dot{\boldsymbol{q}} \right) \cdot \dot{\boldsymbol{q}} \qquad = \boldsymbol{0}\,. \tag{3.12}$$

Herein, it is

$$\boldsymbol{\nabla}_{\boldsymbol{q}} \Phi \equiv \begin{bmatrix} \boldsymbol{\nabla}_{\boldsymbol{q_1}} \Phi & \cdots & \boldsymbol{\nabla}_{\boldsymbol{q_n}} \Phi \end{bmatrix} = \begin{bmatrix} \frac{\partial \Phi_1(\boldsymbol{q})}{\partial \boldsymbol{q}_1} & \cdots & \frac{\partial \Phi_1(\boldsymbol{q})}{\partial \boldsymbol{q}_n} \\ \vdots & \ddots & \vdots \\ \frac{\partial \Phi_m(\boldsymbol{q})}{\partial \boldsymbol{q}_1} & \cdots & \frac{\partial \Phi_m(\boldsymbol{q})}{\partial \boldsymbol{q}_n} \end{bmatrix} \in \mathbb{R}^{m \times 7n} \quad . \tag{3.13}$$

To be consistent with system (3.8), a transformation from $\ddot{\boldsymbol{q}} = (\ddot{\boldsymbol{r}}\ \ddot{\mathcal{P}})^T$ into $\dot{\boldsymbol{h}} = (\ddot{\boldsymbol{r}}\ \dot{\boldsymbol{\omega}}')^T$ is necessary and by using the relation

$$\ddot{\mathcal{P}} = \frac{1}{2}\boldsymbol{L}^T\dot{\boldsymbol{\omega}}' - \frac{1}{4}(\boldsymbol{\omega}'^T\boldsymbol{\omega}')\mathcal{P} \tag{3.14}$$

Eq. (3.12) yields to

$$\underbrace{\left[\boldsymbol{\nabla}_{\boldsymbol{r_1}}\Phi\ \ \tfrac{1}{2}(\boldsymbol{\nabla}_{\boldsymbol{p_1}}\Phi)\boldsymbol{L}_1^T\ \ \cdots\ \ \boldsymbol{\nabla}_{\boldsymbol{r_n}}\Phi\ \ \tfrac{1}{2}(\boldsymbol{\nabla}_{\boldsymbol{p_n}}\Phi)\boldsymbol{L}_n^T\right]}_{\boldsymbol{B}:=} \cdot \begin{bmatrix}\ddot{\boldsymbol{r}}_1\\ \dot{\boldsymbol{\omega}}'_1\\ \vdots\\ \ddot{\boldsymbol{r}}_n\\ \dot{\boldsymbol{\omega}}'_n\end{bmatrix} - \boldsymbol{\gamma}^{\#} = \boldsymbol{0} \quad , \tag{3.15}$$

with $\boldsymbol{\gamma}^{\#}$ being a coupling term specified on the mechanical joint between the bodies and defined as

$$\boldsymbol{\gamma}^{\#} = \begin{bmatrix}\boldsymbol{0}\\ \frac{1}{4}({\boldsymbol{\omega}'_1}^T\boldsymbol{\omega}'_1)\boldsymbol{\nabla}_{\boldsymbol{p_1}}\Phi\cdot\boldsymbol{p}_1\\ \vdots\\ \boldsymbol{0}\\ \frac{1}{4}({\boldsymbol{\omega}'_n}^T\boldsymbol{\omega}'_n)\boldsymbol{\nabla}_{\boldsymbol{p_n}}\Phi\cdot\boldsymbol{p}_n\end{bmatrix} - \boldsymbol{\nabla}_{\boldsymbol{q}}\left(\boldsymbol{\nabla}_{\boldsymbol{q}}\Phi\cdot\dot{\boldsymbol{q}}\right)\cdot\dot{\boldsymbol{q}} \quad . \tag{3.16}$$

Thus, the constraint conditions (3.11) and (3.12) can be summarized in the following relations:

$$\dot{\Phi} = \boldsymbol{\nabla}_{\boldsymbol{q}}\Phi\cdot\dot{\boldsymbol{q}} \qquad = \boldsymbol{B}\boldsymbol{h} \qquad = \boldsymbol{0} \tag{3.17}$$

$$\ddot{\Phi} = \boldsymbol{\nabla}_{\boldsymbol{q}}\Phi\cdot\ddot{\boldsymbol{q}} + \boldsymbol{\nabla}_{\boldsymbol{q}}\left(\boldsymbol{\nabla}_{\boldsymbol{q}}\Phi\cdot\dot{\boldsymbol{q}}\right)\cdot\dot{\boldsymbol{q}} \qquad = \boldsymbol{B}\dot{\boldsymbol{h}} - \boldsymbol{\gamma}^{\#} \qquad = \boldsymbol{0}\,, \tag{3.18}$$

with $\boldsymbol{B}$ being the coupled system matrix defined in Eq. (3.15).

Moreover, reaction forces and moments caused by mechanical joints have to be considered. Lagrange multipliers λ are often used to fuse the governing

equations with constraint conditions. The additional vector $\boldsymbol{g}^c$ containing constraint reaction forces $\boldsymbol{f}^c$ and moments $\boldsymbol{m}'^c$, which is simply added to the right hand side of the system (3.8), can be derived as

$$\boldsymbol{g}^c = \begin{bmatrix} \boldsymbol{f}_1^c \\ \boldsymbol{m}_1'^c \\ \boldsymbol{f}_2^c \\ \boldsymbol{m}_2'^c \end{bmatrix} = \begin{bmatrix} \boldsymbol{\nabla}_{\boldsymbol{q_1}}^T \Phi \\ \boldsymbol{\nabla}_{\boldsymbol{q_2}}^T \Phi \end{bmatrix} \cdot \begin{bmatrix} \lambda_1 \\ \lambda_2 \end{bmatrix} = \begin{bmatrix} (\boldsymbol{\nabla}_{\boldsymbol{r_1}}^T \Phi)\lambda_1 \\ \frac{1}{2}\boldsymbol{L}_1(\boldsymbol{\nabla}_{\boldsymbol{p_1}}^T \Phi)\lambda_1 \\ (\boldsymbol{\nabla}_{\boldsymbol{r_2}}^T \Phi)\lambda_2 \\ \frac{1}{2}\boldsymbol{L}_2(\boldsymbol{\nabla}_{\boldsymbol{p_2}}^T \Phi)\lambda_2 \end{bmatrix} = \boldsymbol{B}^T \boldsymbol{\lambda} \quad . \tag{3.19}$$

Finally, following equation system describes the motion of n mechanically coupled bodies using quaternions to describe spatial positions:

$$\begin{bmatrix} \boldsymbol{A} & \boldsymbol{B}^T \\ \boldsymbol{B} & \boldsymbol{0} \end{bmatrix} \begin{bmatrix} \dot{\boldsymbol{h}} \\ -\boldsymbol{\lambda} \end{bmatrix} + \begin{bmatrix} \boldsymbol{b} \\ \boldsymbol{0} \end{bmatrix} = \begin{bmatrix} \boldsymbol{g} \\ \boldsymbol{\gamma}^{\#} \end{bmatrix} \quad . \tag{3.20}$$

3.2.2 Basic constraint conditions

In this section some basic mechanical couplings with their associating constraints are presented. Generally, these joints restrict the bodies in one or two degrees of freedom, but they can be combined to each other for more complex joints and if less degrees of freedom are desired. More types of mechanical joints can be found in [Nikravesh et al., 1985a], [Nikravesh et al., 1985b] and [Woernle, 2011].

Rigid link

To model a rigid link of two coupled bodies, the distance $\boldsymbol{d}$ between two points i and j of each body has to be restricted to a constant length l. As indicated by Fig. 3.3, it can be expressed in terms of global coordinates $\boldsymbol{s}_i$ and $\boldsymbol{s}_j$ and replaced by transformation into local coordinates $\boldsymbol{s}_i'$ and $\boldsymbol{s}_j'$ as follows

$$\begin{aligned} \boldsymbol{d} &= (\boldsymbol{r}_j + \boldsymbol{s}_j) - (\boldsymbol{r}_i + \boldsymbol{s}_i) \\ &= \boldsymbol{r}_j + \boldsymbol{S}_j \cdot \boldsymbol{s}_j' - \boldsymbol{r}_i - \boldsymbol{S}_i \cdot \boldsymbol{s}_i' \quad . \end{aligned} \tag{3.21}$$

Thus, the constant distance constraint for the rigid link can be acquired through

$$\Phi(q) = \boldsymbol{d} \cdot \boldsymbol{d} - l^2 = 0 \quad . \tag{3.22}$$

To obtain the coupled system matrix $\boldsymbol{B}$ and the associating term $\boldsymbol{\gamma}^{\#}$ for the system (3.20), the additional constraints (3.17) and (3.18) have to be acquired for this link. A detailed composition of matrix $\boldsymbol{B}$ and $\boldsymbol{\gamma}^{\#}$ are given in Tab. 3.1 and 3.2, respectively. Herein, $\boldsymbol{S}_i$ and $\boldsymbol{\omega}_i'$ for $i = 1, 2$ denote the rotation matrix and the local angular velocity of the body i.

Table 3.1: *Detailed components of matrix $\boldsymbol{B}$ of the rigid link.*

Φ	$\boldsymbol{\nabla}_{\boldsymbol{r_1}}\Phi$	$\frac{1}{2}(\boldsymbol{\nabla}_{\boldsymbol{p_1}}\Phi)\boldsymbol{L}_1^T$	$\boldsymbol{\nabla}_{\boldsymbol{r_2}}\Phi$	$\frac{1}{2}(\boldsymbol{\nabla}_{\boldsymbol{p_2}}\Phi)\boldsymbol{L}_2^T$
$\boldsymbol{d} \cdot \boldsymbol{d} - l^2 = 0$	$-2\boldsymbol{d}^T$	$2\boldsymbol{d}^T\boldsymbol{S}_1\boldsymbol{s}_1'$	$-2\boldsymbol{d}^T$	$-2\boldsymbol{d}^T\boldsymbol{S}_2\boldsymbol{s}_2'$

Table 3.2: *Composition of $\boldsymbol{\gamma}^{\#}$ for the rigid link.*

Φ	$\boldsymbol{\gamma}^{\#}$
$\boldsymbol{d} \cdot \boldsymbol{d} - l^2 = 0$	$-2\boldsymbol{d}^T\boldsymbol{d} + 2\boldsymbol{d}^T(\boldsymbol{\omega}_1' \times \dot{\boldsymbol{s}}_1{}' - \boldsymbol{\omega}_2' \times \dot{\boldsymbol{s}}_2{}')$

Translational joint

As indicated by Fig. 3.4, the translational joint constraints two bodies to move along a common axis. Chose two arbitrary points on each body, which are all located on the same joint axis, i.e. P_A and Q_A on body A and P_B and Q_B on body B. To derive constraint equations, the connection vectors $\boldsymbol{s}_A$, $\boldsymbol{s}_B$ and $\boldsymbol{d}$ between these points have to acquire the following constraints

$$\Phi_1(\boldsymbol{q}) = \boldsymbol{s}_A \times \boldsymbol{s}_B = \boldsymbol{0} \tag{3.23}$$

$$\Phi_2(\boldsymbol{q}) = \boldsymbol{s}_A \times \boldsymbol{d} \quad = \boldsymbol{0} \quad . \tag{3.24}$$

In other words, these vectors have to be parallel to each other at all times. Thus, there are two relative degrees of freedom between bodies connected by

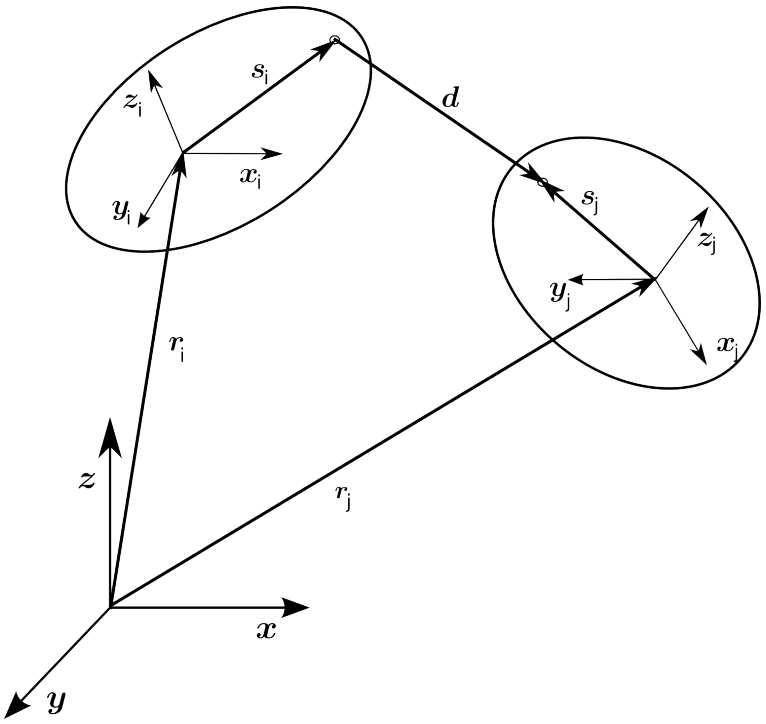

Figure 3.3: *Spatial positions in a multi-body system.*

this translational joint. Note, that body B can still rotate about the joint axis, which is non-relevant for the application purposes in the present studies.

If no relative rotation between the bodies is desired, i.e. just one relative degree of freedom, an additional constraint is required. Define two perpendicular vectors, e.g. $\boldsymbol{h}_A$ and $\boldsymbol{h}_B$ on Bodies A and B, which have to remain perpendicular to each other: $\Phi_3(q) = \boldsymbol{h}_A^T \boldsymbol{h}_B = 0$. But for the application purposes in this paper, constraints (3.23) and (3.24) are sufficient.

The required matrix $\boldsymbol{B}$ and $\boldsymbol{\gamma}^{\#}$ for solving the system (3.20) can be derived in the same manner as above and are given in Tab. 3.3 and 3.4, in which $\boldsymbol{S}_A$ and $\boldsymbol{S}_B$ represent the rotation matrix of body A and B, respectively.

Rope model

The physical characteristics of springs and dampers are very versatile in their application. These basic mechanical elements can be used to model the elastic behaviour of ropes. Since the rope is only applying tension forces to a body,

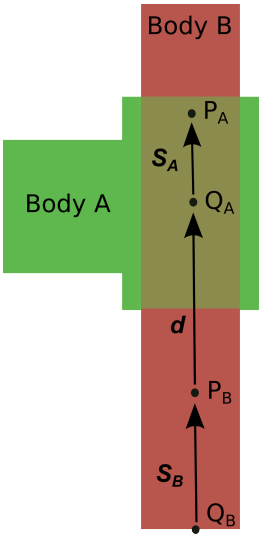

Figure 3.4: *A translational joint.*

constraint forces are simply added to Eq. (3.7) as external forces. If the distance $|\boldsymbol{d}|$ between the points i and j is below the defined relaxed rope length l, no constraint forces are taken into account and the equations of motion will be solved separately for each body. As soon as d exceeds l, the additional external force

$$\boldsymbol{f}_{rope} = C\,(|\boldsymbol{d}| - l)\frac{\boldsymbol{d}}{|\boldsymbol{d}|} + D\,\dot{\boldsymbol{d}} \tag{3.25}$$

is applied to both of the coupled bodies with opposite signs. Herein, C and D denote to spring and damping coefficients.

The choice of the coefficients C and D is crucial for the rope's behaviour. Typical classifications of ropes are based on their maximum breaking load and their elongation at 50% breaking load.

Fig. 3.5 exemplifies two ropes with different characteristics. The stiff rope

Table 3.3: *Detailed components of matrix* $\boldsymbol{B}$ *for the translational joint.*

Φ	$\nabla_{\boldsymbol{r_1}}\Phi$	$\frac{1}{2}(\nabla_{\boldsymbol{p_1}}\Phi)\boldsymbol{L}_1^T$	$\nabla_{\boldsymbol{r_2}}\Phi$	$\frac{1}{2}(\nabla_{\boldsymbol{p_2}}\Phi)\boldsymbol{L}_2^T$
$\boldsymbol{s}_A \times \boldsymbol{s}_B = \boldsymbol{0}$	$\boldsymbol{0}$	$(\boldsymbol{s}_B \times \boldsymbol{s}_A)^T\boldsymbol{S}_A$	$\boldsymbol{0}$	$-(\boldsymbol{s}_A \times \boldsymbol{s}_B)^T\boldsymbol{S}_B$
$\boldsymbol{s}_A \times \boldsymbol{d} = \boldsymbol{0}$	$-\boldsymbol{s}_A$	$(\boldsymbol{d} \times \boldsymbol{s}_A)^T\boldsymbol{S}_A$	$\boldsymbol{s}_A$	$-(\boldsymbol{s}_A \times \boldsymbol{s}_B)^T\boldsymbol{S}_B$

Table 3.4: *Composition of $\boldsymbol{\gamma}^{\#}$ for the translational joint.*

Φ	$\boldsymbol{\gamma}^{\#}$
$\boldsymbol{s}_A \times \boldsymbol{s}_B = \boldsymbol{0}$	$-2(\dot{\boldsymbol{s}}_A \times \dot{\boldsymbol{s}}_B) + (\boldsymbol{s}_B \times \boldsymbol{\omega}_A)\dot{\boldsymbol{s}}_A - (\boldsymbol{s}_A \times \boldsymbol{\omega}_B)\dot{\boldsymbol{s}}_B$
$\boldsymbol{s}_A \times \boldsymbol{d} = \boldsymbol{0}$	$-2(\dot{\boldsymbol{s}}_A \times \dot{\boldsymbol{d}}) + \boldsymbol{s}_A \times (\boldsymbol{\omega}_A \times \dot{\boldsymbol{s}}_A - \boldsymbol{\omega}_B \times \dot{\boldsymbol{s}}_B) + \boldsymbol{d} \times (\boldsymbol{\omega}_A \times \dot{\boldsymbol{s}}_A)$

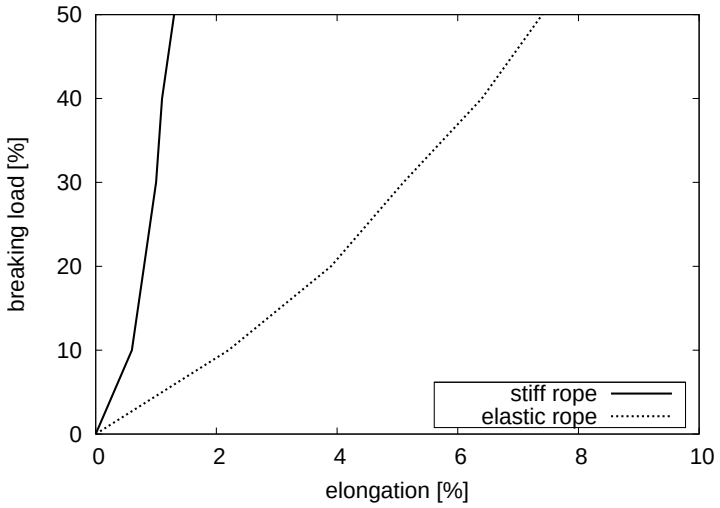

Figure 3.5: *Load-Elongation diagram of a stiff and an elastic rope.*

manifests an elongation of 1.3% at 50% breaking load. The elastic rope features an elongation of 7.4% at the same breaking load, which corresponds to a length deviation of $6.1m$ for a $100m$ rope.
Different rope characteristics can be modelled by choosing appropriate parameters in Eq. (3.25). As Hooke's law relates the spring force f to a length deviation $(|\boldsymbol{d}| - l)$, a $100m$ rope with a maximum breaking load of $200t$ and an elongation of 1.3% at 50% breaking load would have a spring coefficient of $755kN/m$.
To obtain the damping coefficient, a frequently employed damping measure is used and is given by the damping ratio

$$\delta = \frac{D}{2\sqrt{C \cdot m}} \ , \tag{3.26}$$

which is dependent on the attached body's mass m. Realistic ropes exhibit an

under-damped behaviour, which refers to $0 < \delta < 1$.

Fender model

Another important mechanical device in ship operations is the fender. To mimic its property, two models are presented.

The first model (I) is also based on the spring-damper system outlined by Eq. (3.25). As opposed to the rope, the fender applies repellent forces to a body, if a predefined minimum distance, i.e. the fender thickness, cannot be maintained due to the body's motion. The effective direction of fender normal forces are dependent on the fender's geometrical extent and are usually applied radial to the longitudinal axes of the fender geometry. If the fender gets compressed, normal forces can be determined by

$$\boldsymbol{f}_n = C \cdot \Delta x \cdot \boldsymbol{n} + D \cdot \dot{\boldsymbol{n}} \ , \tag{3.27}$$

where Δx is the fender deformation and $\boldsymbol{n}$ denotes the unit vector in radial direction of the fender.

Additionally, friction forces have to be taken into account. To determine the friction between the fender and the floating body, the dynamic motion of the body has to be considered. The fender can either stick to or slip against the body. Given by Coulomb's law of friction, the relation between normal force f_n and tangential friction force f_f is defined by

$$|f_f| \leq \mu \, |f_n| \ . \tag{3.28}$$

Herein, μ is a (constant) friction coefficient. Since Eq. (3.28) is an inequality, the actual acting friction force can be significantly lower than the maximum friction force

$$|f_{f,max}| = \mu \, |f_n| \ , \tag{3.29}$$

which at the same time defines the limit of stiction forces. While the normal force can be obtained by Eq. (3.27), the required friction force has to be derived from the equations of motion. The dynamic tangential motion at the contact point between body and fender is neutralized, if the sum of all forces acting on that specific point is less than $f_{f,max}$. Therefore, the spring-damper system

$$\boldsymbol{f}_{fr} = C \cdot dx_{cp} \cdot (-\frac{\boldsymbol{v}_{cp}}{|\boldsymbol{v}_{cp}|}) + D \cdot \boldsymbol{v}_{cp} \tag{3.30}$$

is used to model the friction force $\boldsymbol{f}_{fr}$. Here, $\boldsymbol{v}_{cp}$ and dx_{cp} denote the tangential velocity and the associated tangential displacement of the contact point. This modelling is suited for implicit calculations, since large tangential force impacts on the contact point are detected as opposing accelerations and will be counterbalanced in the implicit iteration. If there is no velocity of the contact point, no friction force will be applied.

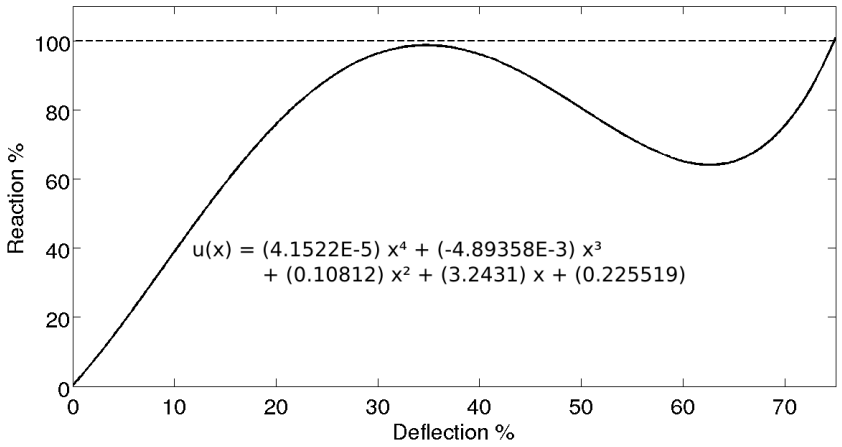

Figure 3.6: *Non-linear characteristic curve of the fender's reaction force.*

In the second fender model (II) the characteristic behaviour of the fender is predefined by a non-linear characteristic function as shown in Fig. 3.6. This specific type of fender has the feature of self protecting from over-compression. In Fig. 3.6 the percentage of the reaction force is given over the percental deflection of the fender. The force close to the maximum load is already achieved at 33% of compression. Followed by a region of decreased forces ($\sim$ 60% reaction force), the maximum reaction load reaches to $\sim$ 75% of compression.

Choosing an appropriate maximum reaction force f_{max}, the fender normal force $\boldsymbol{f}_n$ can be obtained using the characteristic curve $u(x)$ as following

$$\boldsymbol{f}_n = 0.01 \cdot u(x) \cdot f_{max} \cdot \boldsymbol{n} \ , \tag{3.31}$$

where x defines the deformation of the fender. For the associated friction force

$$\boldsymbol{f}_{fr} = 0.01 \cdot u(dx_{cp}) \cdot f_{max} \cdot (-\frac{\boldsymbol{v}_{cp}}{|\boldsymbol{v}_{cp}|}) \tag{3.32}$$

the argument of the characteristic function $u(dx)$ refers to the vertical displacement of the contact point.
The friction condition at the contact point in both fender models refers either to stick or slip, based on the comparison of the forces defined in Eq. (3.29) and (3.30) or (3.32) respectively:

$$f_f = \begin{cases} f_{f,max} \ , & \text{if} \quad f_{f,max} \leq |\boldsymbol{f}_{fr}| \quad \text{(slip)} \\ |\boldsymbol{f}_{fr}| \ , & \text{else} \qquad\qquad\quad \text{(stick)} \end{cases} \tag{3.33}$$

3.2.3 Stabilization method

To suppress the error-growth during the numerical integration process, a feedback controller is needed to achieve stable results. A violation of residuals in the state and velocity condition equations, i.e. $\Phi \neq 0$ and $\dot{\Phi} \neq 0$, can be dampened by Baumgarte's constraint violation stabilization method [Baumgarte, 1972]:

$$\ddot{\Phi} + 2\alpha\dot{\Phi} + \beta^2\Phi = 0 \tag{3.34}$$

herein, $\alpha, \beta > 0$ are related to the damping coefficient and the resonant frequency respectively. Using following identity

$$\ddot{\Phi} = \boldsymbol{B}\dot{\boldsymbol{h}} - \boldsymbol{\gamma}^{\#} = 0 \tag{3.35}$$

and inserting $\ddot{\Phi}$ from Eq. (3.34) into Eq. (3.20), the final equation systems reads

$$\begin{bmatrix} \boldsymbol{A} & \boldsymbol{B}^T \\ \boldsymbol{B} & \boldsymbol{0} \end{bmatrix} \begin{bmatrix} \dot{\boldsymbol{h}} \\ -\boldsymbol{\lambda} \end{bmatrix} + \begin{bmatrix} \boldsymbol{b} \\ \boldsymbol{0} \end{bmatrix} = \begin{bmatrix} \boldsymbol{g} \\ \boldsymbol{\gamma}^{\#} - 2\alpha\dot{\Phi} - \beta^2\Phi \end{bmatrix}. \tag{3.36}$$

For $\alpha = \beta = 0$, there is no stabilization and the system's response can diverge from the exact solution. Usually, solving system (3.36) for $\alpha, \beta \neq 0$ the numerical response oscillates around the exact solution value, see Fig. 3.7. However, in some application cases this oscillation can distort the actual dynamics of the mechanical system. According to [Woernle, 2011], β should not exceed the lowest resonance frequency on the one hand, but on the other hand too small values can lead to a rigid system. [Nikravesh, 1988] recommends values of $\alpha, \beta \in [1, 10]$. In this thesis reasonable results were achieved by using values of $\alpha = \beta = 10$. However, universal convenient values for α and β are not established.

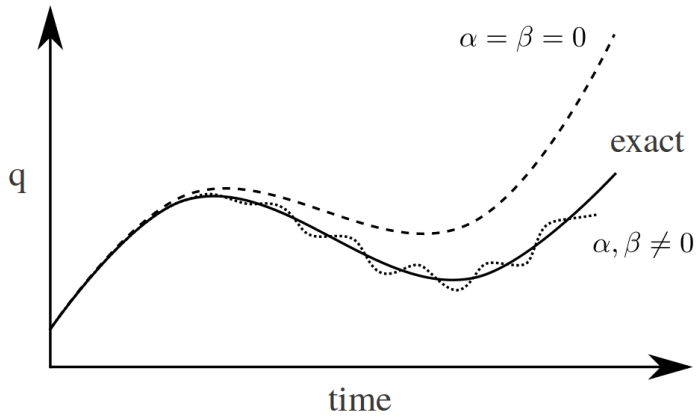

Figure 3.7: *Schematic representation of the exact and numerical solution to a typical dynamic response [Nikravesh, 1988].*

3.3 Overset-grid method

The overset-grid technique, also known as overlapping/chimera grid method, is well suited for numerical simulations of large relative motions involving multiple bodies. The idea of the method is to cover the computational domain by a

number of grids which overlap with each other. Usually, the background mesh defines the extents of a fixed domain of interest and the foreground meshes are attached to each moving body. This grid arrangement has two major advantages. On the one hand, the grid generation process of complex geometries can be improved and employed in higher quality. Furthermore, grid components can be added or removed as desired. On the other hand, body parts which move close to each other or even intersect with each other can be modelled easily. Though, the implementation of this technique is rather complex regarding the interpolation/coupling between/of the grids, especially when it comes to parallel computations. Still this method seems to represent a very good balance between computational flexibility and technical feasibility.

The overset-grid technique implemented in the simulation tool FreSCo+ is assigned to a mass-conservative, strongly coupled and fully parallelised approach as described by [Brunswig and Rung, 2011], [Rung et al., 2009] and [Völkner et al., 2015]. To couple the grids at the overlapping region, the cell value on a target grid is interpolated by field values φ from a donor grid by using the following generic interpolation equation:

$$\varphi_t = \sum_{i=1}^{n} w_i \varphi_i + \delta \tag{3.37}$$

φ_i are the field values at the n donor cells for the target value φ_t, w_i denote the associated interpolation weights and the parameter δ contains additional terms, e.g. functions of gradients of higher order methods. Since all grid equations have to be solved by one global equation system, the grid coupling can be treated in an implicit (strong coupling) way, see Fig. 3.8. Here, the coefficients of the system matrix are the weighted sum of the field values and the right-hand side contains the explicit part δ.

For the solving algorithm, the RANS equations are replaced by Eq. (3.37) for those cells which are interpolated from values of the donor grid. The target field values φ_t are interpolated implicitly by replacing the corresponding row of the equation system by a row of unities as coefficient of the main diagonal (marked as red entries in Fig. 3.8) and the respective off-diagonal coefficients obeying $\sum w_i = 1$ (marked as green entries in Fig. 3.8). Different interpolation orders can be chosen: interpolation by a single donor cell value (order 0), trilinear

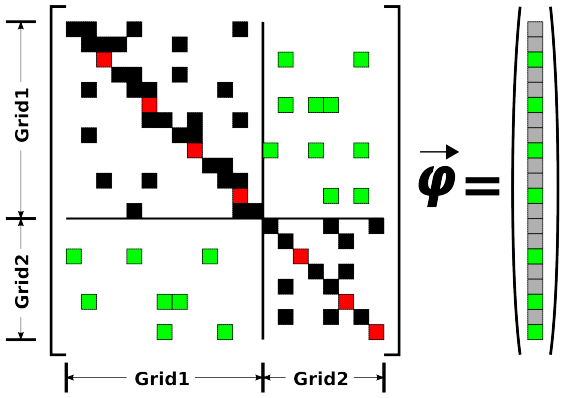

Figure 3.8: *Global equation system using strong grid coupling, [Luo et al., 2012].*

interpolation from a donor tetrahedron (1st order) or the 1st order method in addition to the donor cell gradients (2nd order). A direct evaluation of Eq. (3.37) leads to an explicit interpolation between two grids. The gradients at the interpolation cells are calculated in that manner.

Next to implementation techniques for cell search and interpolation, there are three other overset treatments of interest: pressure correction, mass conservation and dynamic cell status/priority management.

Pressure correction for overset-grids

A special treatment is required for the pressure correction equation. In contrast to the other dependent variables, pressure cannot be solved directly, it has to be obtained by its correction. If there are no interpolation errors, the interpolation scheme (3.37) leads to the same pressure correction field on both donor and target grid. Thus, pressure variations, e.g. due to relative grid motions, will remain disregarded and have to be taken into consideration. The interpolation of the pressure correction is derived from the inter-grid coupling of the pressure

$$p_t = \sum_{i=1}^{n} w_i p_i + \delta(p) \tag{3.38}$$

and treated as following, where $(^*)$ and $(')$ denoting the current and the correction value, respectively:

$$p_t^* + \gamma\, p_t' = \sum_{i=1}^{n} w_i (p_i + \gamma\, p_i') + \delta(p^*) \; . \tag{3.39}$$

Herein, p_i' and p_t' are the pressure correction on the donor and target grid, whereas γ denotes the under-relaxation factor. Mind that the explicit part of the interpolation equation is restricted to the pressure field from the previous iteration p^*. To obtain the modified interpolation equation, the pressure corrections are organized separately from the values of the old pressure field:

$$p_t' - \sum_{i=1}^{n} w_i p_i' = \frac{1}{\gamma} \left[\sum_{i=1}^{n} w_i\, p_i^* + \delta(p^*) - p_t^* \right] \; . \tag{3.40}$$

Obviously, the incorporation of the interpolation schemes into the global equation system leads to a non-symmetric system matrix. Thus, common linear solvers for symmetric matrices are not suited for these problems.

Mass conservation for overset-grids

The finite-volume method is based on flux balancing over each cell volume and thus, is inherently conservative for transported quantities. This approach is not conservative anymore, especially for the mass, if direct field interpolation from one to another grid is considered. Due to the violation of the global mass conservation, the pressure correction loses its consistency and therefore diverges. This problem can be reduced and minimized by using a higher-order interpolation scheme for the velocity field. Furthermore, an additional flux correction is implemented, where the sum of all mass fluxes through the interpolation section on each grid are forced to zero.

Cell status

The overset-grid technique needs to determine the status of each cell, which can be changed dynamically during the computation process. Knowing the

cell status, the solving algorithm can decide and control if a cell needs to be interpolated, used as a donor cell, to be ignored or solved in the common way. For the solution process four cell status are of interest:

- SOLVE
  - the RANS equations are solved for this cell
- INTERPOLATE
  - the values are interpolated by donor cell values from another grid
- DONATE
  - the value is donated for interpolation to a target cell on another grid
- IGNORE
  - this cell is blanked and is not considered in the computation

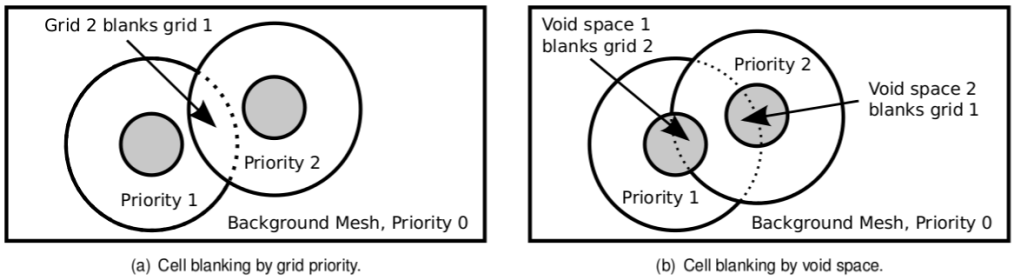

Figure 3.9: *Priority management by cell blanking, [Brunswig and Rung, 2011].*

To enable the employment of an arbitrary number of overlapping grids, the cell status determination process has to follow a priority structure, which can be predefined and assigned to each grid. If two overlapping grids provide donor cells for the interpolation to the same location, the cells of the grid of lower priority will be blanked (status IGNORE), since this part of the computational domain is covered already by a grid of higher priority, see Fig. 3.9a. Another reason for cell blanking is the location outside of the computational domain, or if cells are located in the void space - which is usually the meshed body - of other grids, see Fig. 3.9b. Regions of enabled cells, i.e. SOLVE-, INTERPOLATE- and DONATE-cells, are located in overlapping regions with grid coupling. In certain circumstances, the priority can be changed dynamically for cells of lower grid priority, which feature a higher grid quality than the cells of the higher grid priority due to grid movements, see Fig. 3.10.

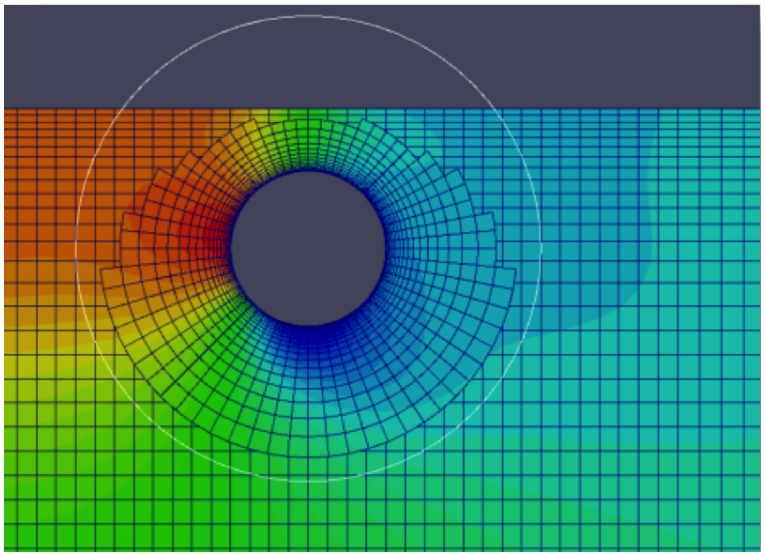

Figure 3.10: *Illustration of the variable cell priority for a cylinder in a channel: The void space of the background grid, [Brunswig and Rung, 2011].*

3.4 Solution algorithm

The overall solution algorithm, illustrated in Fig. 3.11, consists of two main procedures - the flow solver and the motion solver. If no body motion is enabled, the flow solving algorithm focuses on the conservation equations. Herein, the three velocity components u_i, $i = 1, 2, 3$ are computed by the momentum equation (2.3) in the first place. Then, the pressure can be determined using the continuity equation (2.1) and the SIMPLE-algorithm. In case of turbulent flows, the turbulence variables are established and afterwards, the volume fractions c and c_2 for multi-phase flow simulations are obtained by Eq. (2.32). Basically, there are two iteration procedures. The inner iterations are concerned with each equation system of the dependent variable, whereas the outer iterations are assigned to the solution steps over all equation systems. The termination of each iteration procedure is defined by either the maximum iteration step or the compliance of a desired convergence. This algorithm is repeated for every time step in an unsteady calculation.

In case of body motions, the solution algorithm addresses the motion solver before solving the conservation equations. The bidirectional fluid-structure interaction is implemented within an expanded iteration procedure. If explicit

time integration is desired, just the values of the last time step are required. Thus, the motion solver is just called once in the first outer iteration of each time step. For implicit time integration the values of the current time step are needed for the determination of the body's position and velocity. Therefore, the motion modeller has to be called in every outer iteration.

At first, the motion modeller accumulates the hydrodynamic forces and moments acting on each body. These values arise from the pressure and sheer stresses established by the Navier-Stokes-equations and are set to zero in the initialization step. In conjunction with the mechanical forces due to coupling joints in a multi-body system, the equations of motions for each body can be obtained by the equation system (3.36). Finally, the updated body motion values of position and velocity can be transferred into a new grid position and thus, induce new hydrodynamic forces on the body.

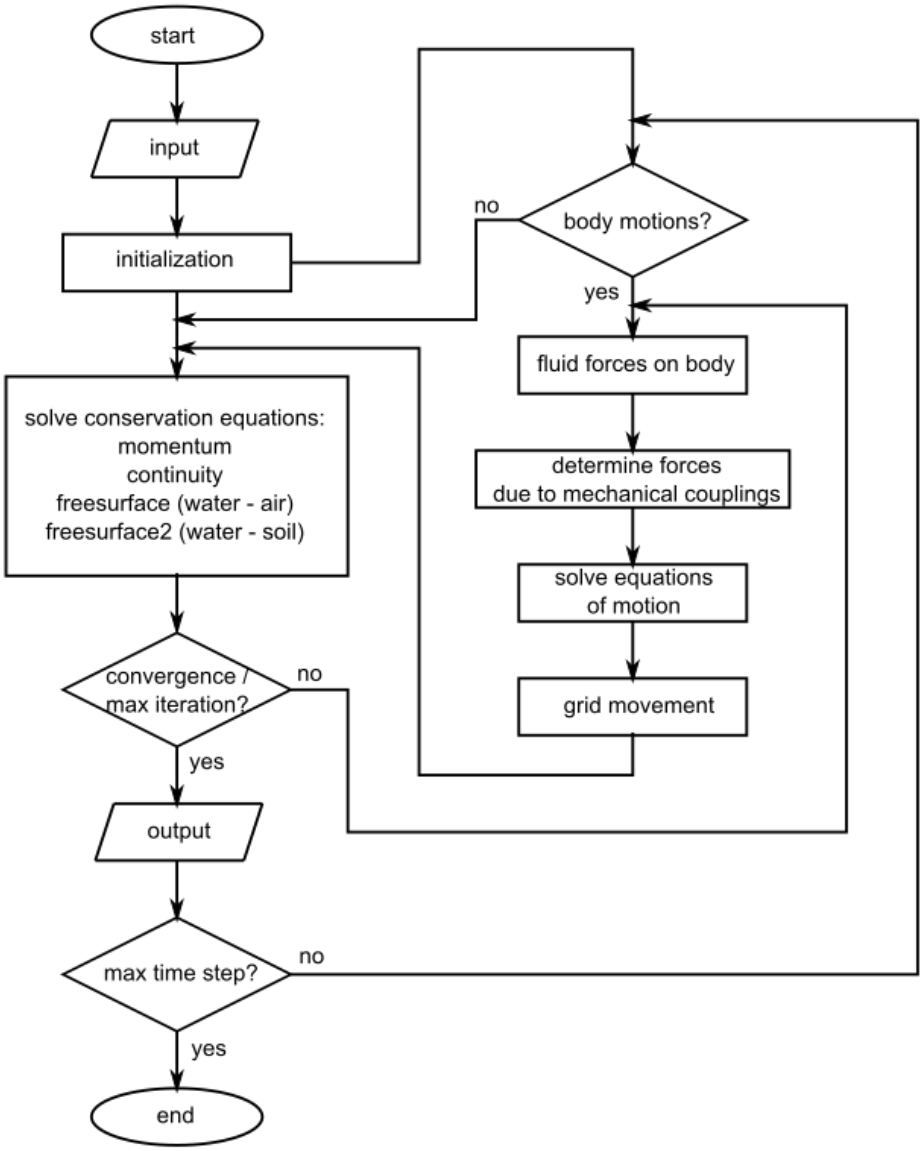

Figure 3.11: *Flow chart of the solution algorithm using implicit coupling of flow solution and body motions.*

4 Verification and Validation

In this chapter different verification and validation cases are presented. The simulations were carried out by the simulation tool FreSCo+ based on the described methods in Chapter 2 and 3. Herein, simulations using mechanical joints are of particular interest. By reason of efficiency all computations are conducted on a physically compact computation domain.

4.1 Water-impact of a cube

For the study of the behaviour of a cube impacting into a water tank, results obtained from the overset-grids approach have been verified against single-grid results. The aim of this test case is to present the functionality and the quality of the overset-method. A cube with edge length $0.15m$ is falling into a $0.25m \times 1m \times 1m$ tank. Notice that the lateral and bottom boundaries of the tank refer to walls in accord with the experiment reported by [Kraskowski, 2009]. The cube's centre of gravity is displaced by 7 mm to one side which causes a complex angular (roll-over) motion inside the water. The results of an overset-grid simulation with $3.6 \cdot 10^5$ background cells and $1.4 \cdot 10^5$ foreground cells are compared to images of [Kraskowski, 2009] and to the results of a single-grid computation with $6.7 \cdot 10^5$ cells, see Fig. 4.1. The floating-body motion was computed using the quaternion-based motion modeller for the cube using an implicit coupling procedure between the motion modeller and the fluid solver.

Fig. 4.2 reveals an impressive agreement between both simulations and experimental observations for three time instants, i.e. $t = 0.4s, t = 0.6s$ and $t = 0.7s$ after the first contact of the cube with the free surface. Fig. 4.3 compares the predicted vertical accelerations returned by the overset-grids and the single

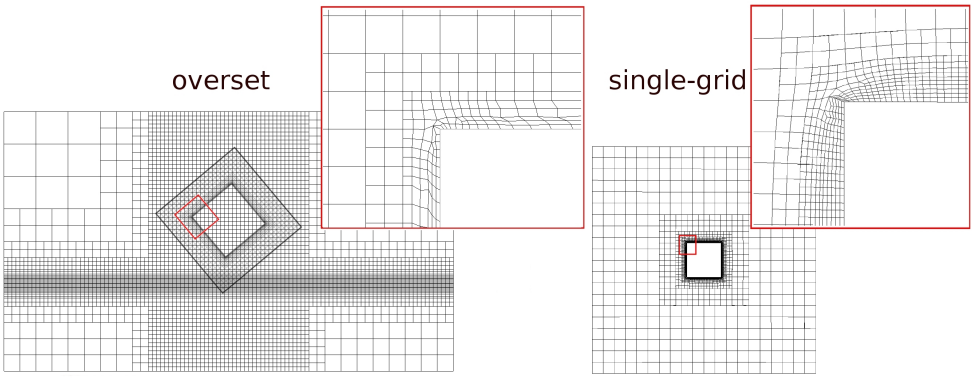

Figure 4.1: *Comparison of numerical grids employed for the water impact of a cube case.*

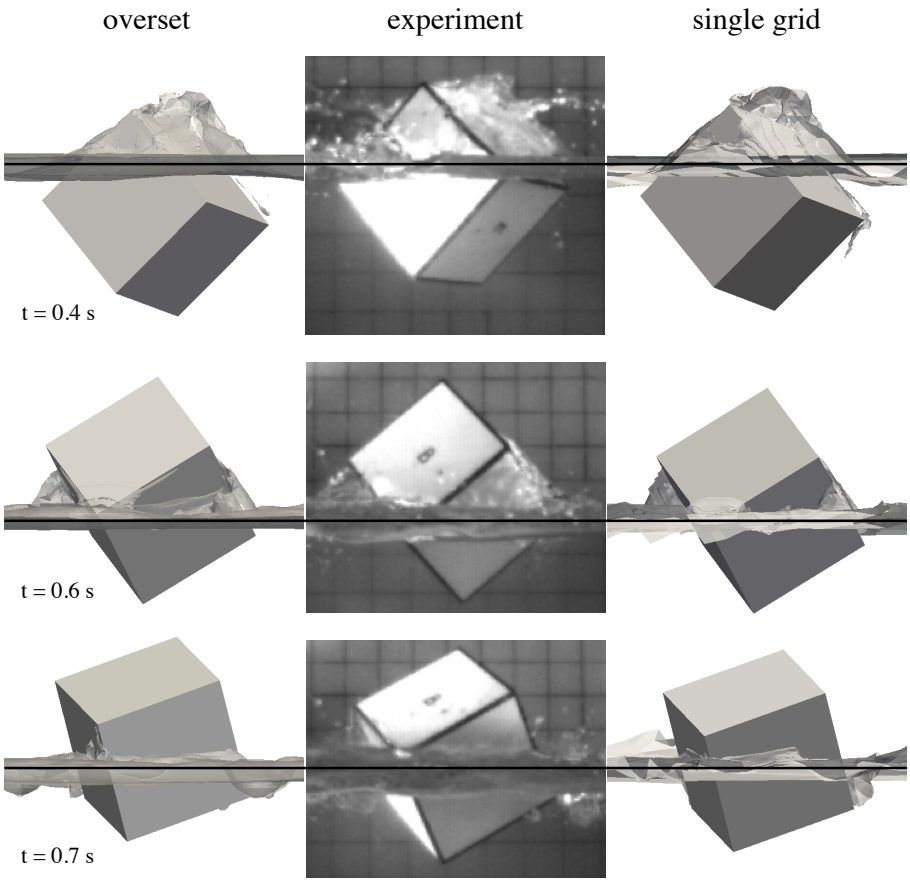

Figure 4.2: *Comparison of cube position and orientation for different points in time. The left pictures refer to overset-grids simulations, the middle ones depict experimental photographs and the right pictures show snapshots from single-grid simulations.*

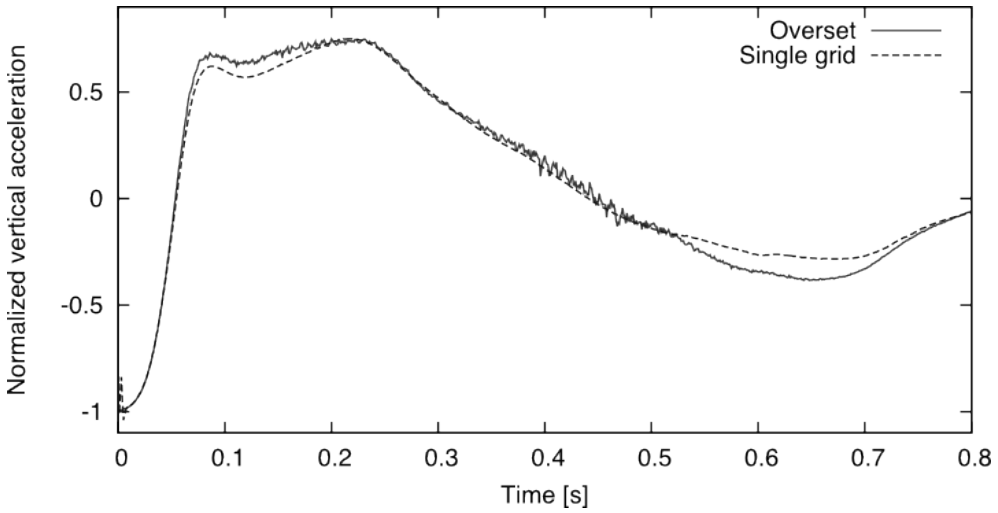

Figure 4.3: *Vertical accelerations impacting on the cube for the overset-grids and the single grid simulations. The accelerations are normalized by earth gravitation.*

grid method. Again an encouraging predictive agreement is seen. Further single grid results for this case can be found in [Koliha, 2011]. For more overset validation cases in FreSCo+, see [Brunswig et al., 2014], [Brunswig and Rung, 2011] or [Völkner et al., 2015].

4.2 Resistance calculation using a rigid link

The next verification case was concerned with the resistance of a Wigley vessel in turbulent flow at Froude number $Fr = 0.20$ and Reynolds number $Re = 5.6 \cdot 10^7$ using a rigid link connection. The dimension of the vessel referred to a length-to-breadth ratio of $L/B = 5$, a draught-to-length ratio of $D/L = 1/16$ and a displacement of and an amidships section coefficient of $C_m = 0.909$. The employed grid consists of $7 \cdot 10^5$ nodes. Results obtained for fixing all degrees of freedom were compared to the simulation of a vessel, which was free to surge with its bow connected to a wall by a rigid link. The rigid link aimed at preventing the vessel from moving backwards. Both single grid simulations used the seaway model described in Sec. 2.3.4 for calm water conditions.

A comparison of the resultant wave pattern is illustrated in Fig. 4.4. Results for the fixed position simulation are displayed in the upper part of the figure

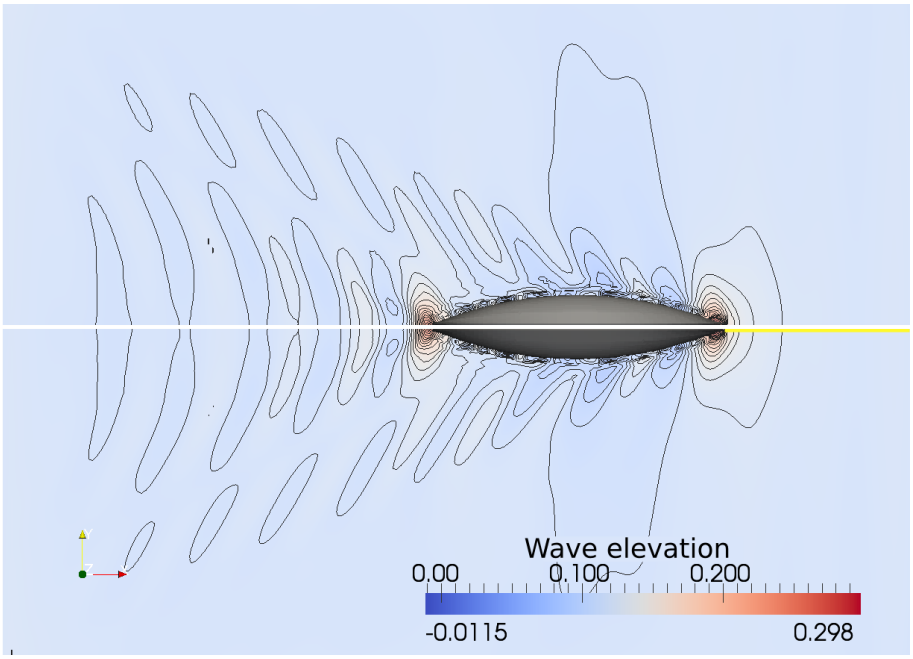

Figure 4.4: *Wave pattern of the resistance test with a fixed vessel (top of figure) and a vessel held by a rigid link (bottom of figure).*

and agree with the wave pattern returned by the rigid link simulation shown in the bottom. An identical total resistance value was obtained for both cases and the relative length change of the rigid link remained in the order of 10^{-4} during the whole simulation, which is deemed negligible.
Other verification and validation cases for this joint model can be found in [Mierke, 2012] and [Luo et al., 2012].

4.3 Falling cube fixed to a rope

This case refers to a test of the rope model by analysing the vertical motion of a free falling 3D-cube with a mass of $10kg$ and an edge length of $1m$ under gravity. As depicted in Fig. 4.5, the cube was attached to a rope of $5m$, which was fixed to a horizontal wall. In the beginning of the simulation, the cube was initialised at a vertical distance of $0.5m$ to the wall (see Fig. 4.5). For this test, a rope that has $20kg$ maximum breaking load (BL) and an elongation (EG) of 2% at half breaking load was considered. Due to Hooke's law and choosing $\delta = 0.5$ in Eq. (3.26) for convenience, one obtains the rope parameters listed

in Tab. 4.1.

Table 4.1: *Rope parameters of the falling cube case.*

EG [%]	**BL** $[kg]$	**C** $[\frac{N}{m}]$	**D** $[\frac{N}{m}s]$
2	20	981	99.045

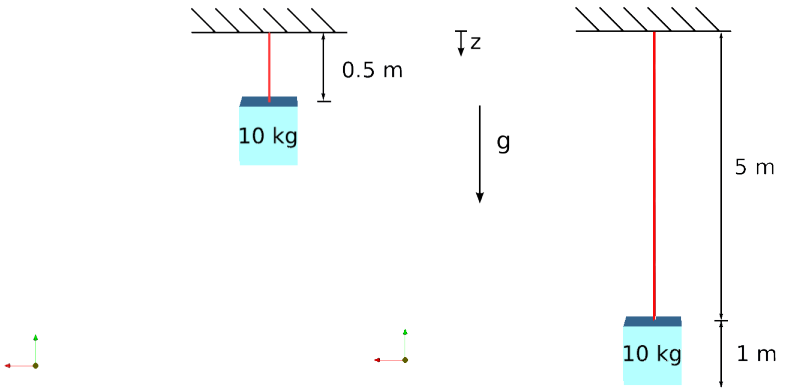

Figure 4.5: *Illustration of the falling cube fixed to a rope. Left: initial position, right: final position.*

The result of the simulation is illustrated in Fig. 4.6. The left diagram displays the temporal evolution of the vertical position and the right chart reveals a history of forces acting on the cube. As the length of the overstretched rope is decreased towards the relaxed length, the cube is accelerated in negative z-direction, cf. close-up in Fig. 4.6 (left), and upward pointing fluid forces up to approximately $25N$ occur in line with the induced hydrodynamic masses. As soon as the contact point distance settled to the predefined rope length of $5m$, the rope forces reduced and finally held the cube under gravitational force. The rope length displayed an overshoot of $5.38m$ and maintained a final length of $5.09m$. Compared to the expected final length according to the rope parameters in Tab. 4.1 of $5.1m$, this corresponded to a relative error of 0.2%. Furthermore, the sum of the rope forces and the fluid forces yield to the weight of the cube, which is in line with the theory. The overshoot is an effect related to the spring-damper-model. The magnitude of the peak can be affected by adjusting the damping behaviour, but has no influence on the final elongation value of the rope. Further details are discussed in section 4.4.

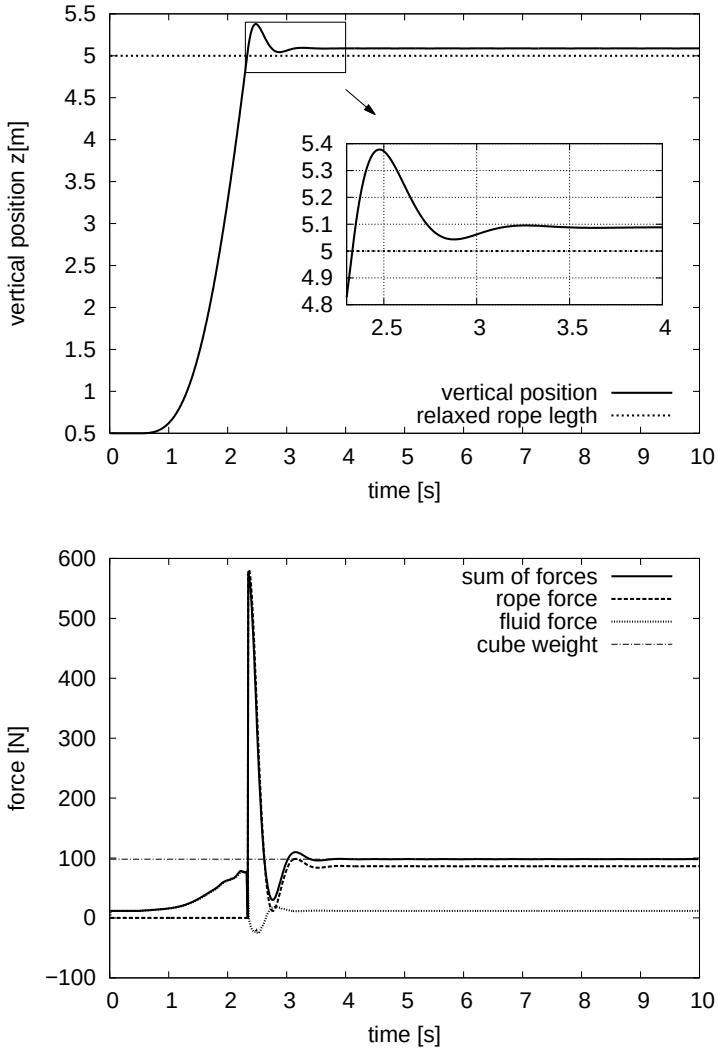

Figure 4.6: *Simulation results of rope length (left) and forces acting on the falling cube (right).*

Results showed that the implemented rope model is able to mimic realistic rope characteristics.

4.4 Rope parameter study

The behaviour of the rope in its overshooting region was investigated for different rope parameters using the simulation set-up of the Wigley vessel from the previous section. Instead of the rigid link connection, a rope was attached

to the vessel's bow. In the initial position of the Wigley, the rope was not tightened. Induced by the incoming current, the vessel moved backwards until the predefined rope length was achieved. The vessel was able to move $0.3m$ in the direction of the current until the rope got tight and held the vessel in place. For the comparison of various rope's characteristics, two different coefficients of extension were paired with different damping parameters as outlined in Tab. 4.2. In each simulation the relaxed rope length referred to $100m$. The spring coefficient can be obtained by Hooke's law and the elongation magnitude of the rope. According to Eq. (3.26) the dependent variable for calculating the damping parameter is the mass m. Since towing operations involve different body masses as well as the relevant hydrodynamic masses, the damping coefficient D can be seen as a function of the vessel's mass m_s.

Table 4.2: *Parameter sets of two different rope types (i.e. stiff and elastic) used in the study.*

EG [%]	**BL** $[t]$	**C** $[\frac{N}{m}]$	**D** $[\frac{N}{m}s]$	$D = D(m)$
1.3 (stiff rope)	100	$3.8 \cdot 10^5$	$5.5 \cdot 10^4$	$D(0.25 \cdot m_s)$
			$7.8 \cdot 10^4$	$D(0.5 \cdot m_s)$
			$1.1 \cdot 10^5$	$D(m_s)$
			$1.6 \cdot 10^5$	$D(2 \cdot m_s)$
			$2.2 \cdot 10^5$	$D(4 \cdot m_s)$
7.4 (elastic rope)	100	$6.6 \cdot 10^4$	$2.3 \cdot 10^4$	$D(0.25 \cdot m_s)$
			$3.2 \cdot 10^4$	$D(0.5 \cdot m_s)$
			$4.6 \cdot 10^4$	$D(m_s)$
			$6.5 \cdot 10^4$	$D(2 \cdot m_s)$
			$9.2 \cdot 10^4$	$D(4 \cdot m_s)$

The resistance coefficients and wave pattern resultant from each computation agreed with the data obtained in the previous case using the rigid link. Figure 4.7 demonstrates the percental length deviation from the rope's relaxed length by observing the normalised distance between the two end points of the rope. Due to the initial position of the vessel, the displayed curves started at -0.3%. The upper figure shows the result for the stiff rope, which had a breaking load of $100t$ and 1.3% elongation. The lower diagram depicts the results for the elastic rope, which had the same breaking load and an elongation of 7.4%.

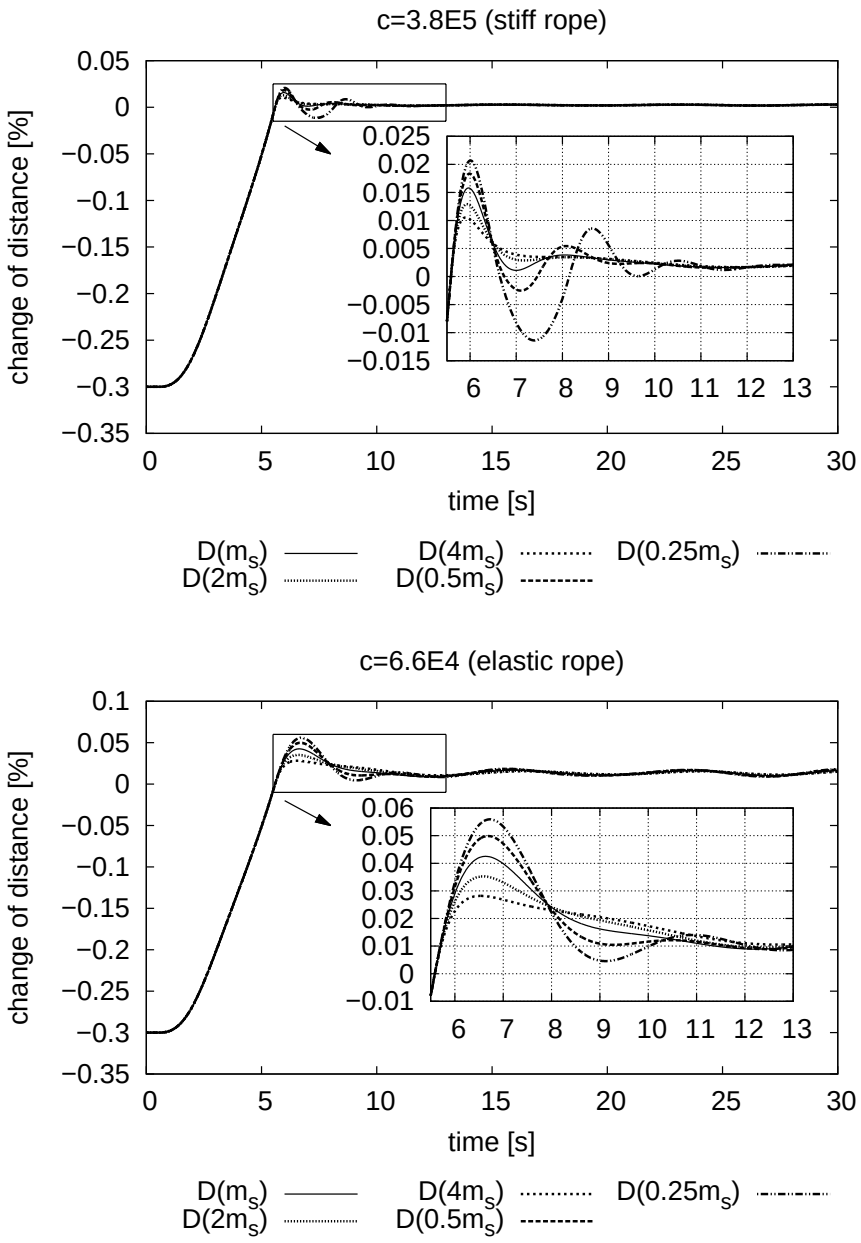

Figure 4.7: *Change of distance of the rope for different damping coefficients and* $100t$ *BL. Top:* 1.3% *EG (stiff rope), bottom:* 7.4% *EG (elastic rope).*

Every simulation manifested a result close to the expectations. Modelled ropes were flexible, and as expected, the ropes with the higher flexible quality - indicated by small values in C (Fig. 4.7, bottom) - elongated more than ropes with lower flexibility - indicated by large values in C (Fig. 4.7, top). Furthermore, less stiff ropes overshot the target length more than the stiff ropes. However, all ropes with identical spring but different damping coefficients led to the same final elongation length. The magnitude of the oscillation amplitude was controlled by choosing appropriate damping parameters for the desired rope characteristic. As indicated by Fig. 4.7, independent on the spring stiffness, larger values of damping coefficients led to smaller or even no oscillations. The two dotted lines are least extended. Looking at the stiff rope with $C = 3.8 \cdot 10^5 N/m$ and $D = 2.2 \cdot 10^5 N \cdot s/m$, the elongation maximum reached 0.011% before remaining a final length of 0.002% above the relaxed rope length. Compared to Tab. 4.2, damping values should be taken from $D(n \cdot m_s)$ for $n > 1$ to avoid large oscillation amplitudes.

4.5 Runup generated by sliding wedge

This validation case was considered with experiments described in [Liu et al., 2005]. The test case studied the wave field and run-up/run-down generated by a sliding three-dimensional rigid wedge and illustrates the attainable accuracy for mechanically coupled simulations of free-surface flows using overset grids. Figure 4.8 shows a sketch of the experimental setup. Simulations were performed for turbulent flows using the $k - \omega$ model and no-slip boundary conditions. Free-surface elevations were measured at different locations, two of which are depicted on the bottom of Fig. 4.8.

In the present study, the motion of the wedge was computed by the 6DoF motion modeller and was mechanically coupled to the ramp by translational joint described in Sec. 3.2.2. In other words: This joint serves as a sleeve bearing for the sling wedge and the motion is calculated numerically in each time step under the mechanical joint condition. Thus, the motion is not predefined. The considered forces are confined to gravitational and fluid dynamic forces, i.e. contact or friction forces between the wedge and the ground are deemed negligible. The initial emergence of the slide was $0.32cm$ and the mass of the

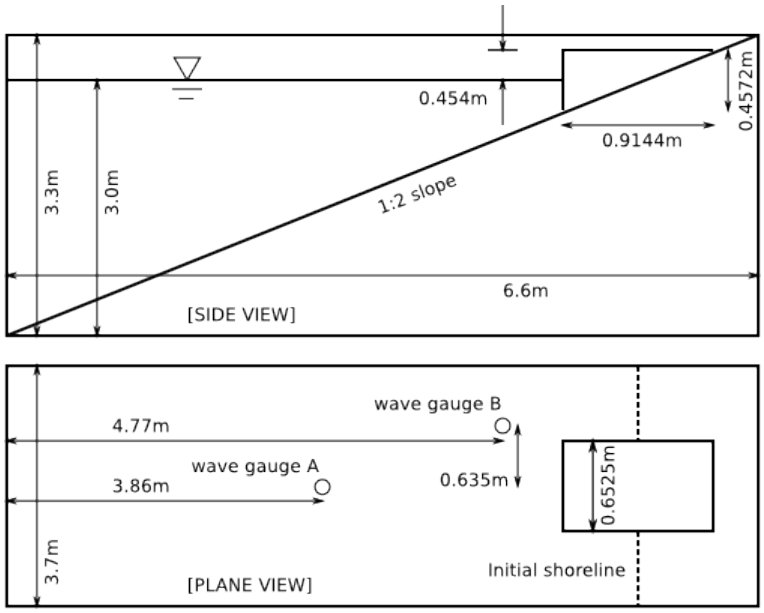

Figure 4.8: *Side view (top) and top view (bottom) with wave gauge locations.*

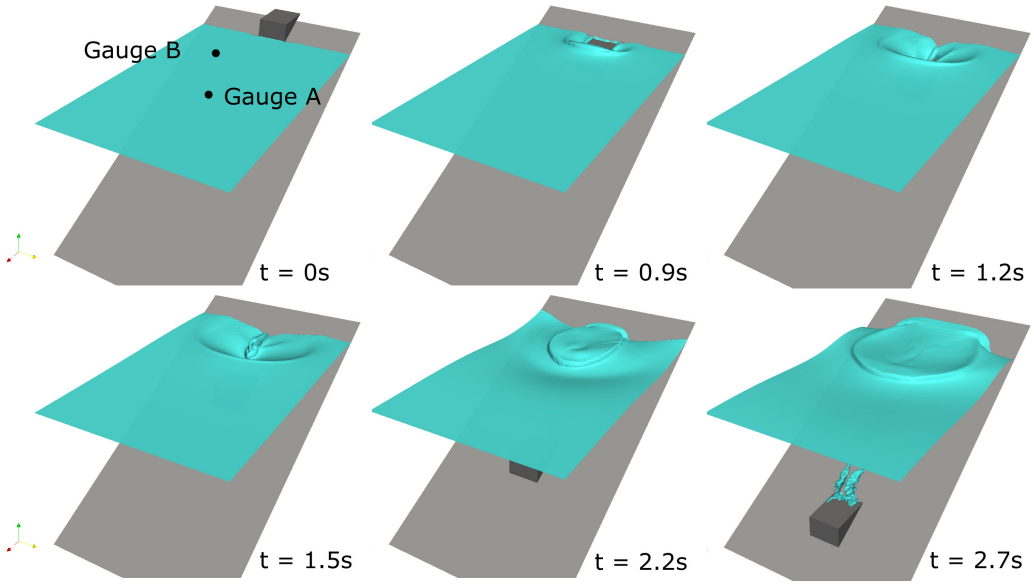

Figure 4.9: *The time evolution of the free-surface for the sliding wedge case.*

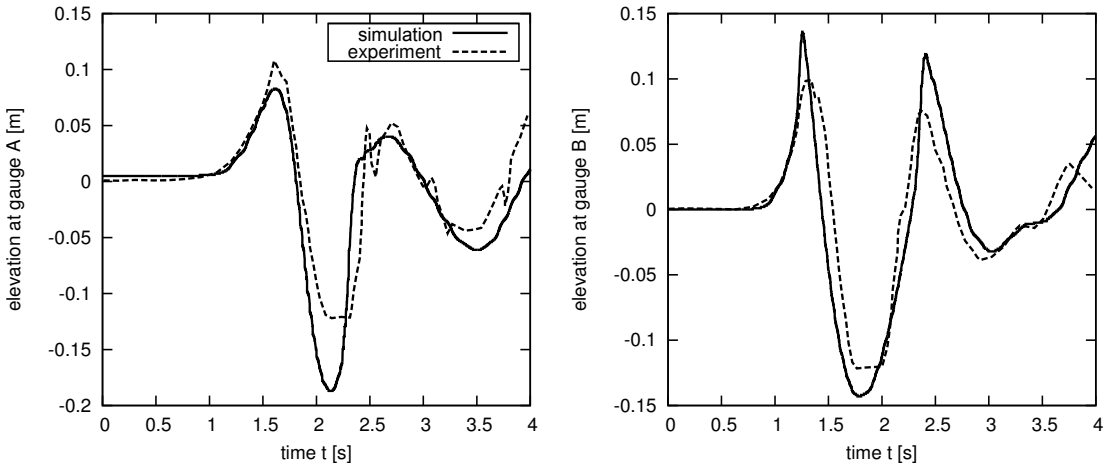

Figure 4.10: *Comparison between numerical results and experimental data reported by Liu et al. [Liu et al., 2005] for the time histories of the free-surface elevation at gauge A (left) and B (right) of the sliding wedge case.*

wedge was assigned to $467.83kg$. The numerical grids contained $5.1 \cdot 10^6$ and $1.55 \cdot 10^5$ cells for the background and the foreground grid, respectively. The simulation used a grid refinement featuring approximately 15 cells per wave height.

Figure 4.9 shows the predicted time evolution of the free-surface contour at six different time steps as the wedge moves down the incline. In this sequence, the generation and its subsequence propagation of a wave train can be observed. Figure 4.10 compares the surface elevations simulated at gauge A and B with experimental data. The wave amplitude in the simulation is slightly underestimated for gauge A and overestimated for gauge B. However, the wave phase is well predicted. Note that the experimental data were carried out by visual observation of video images supported by resistance wave gauges with unknown sampling rates. Overall, the numerical simulation revealed a fair agreement with the experimental data. Furthermore, the numerical variation of the wedge's motion to the incline of the ramp remains in the order of $1 \cdot 10^{-5}$ – and hence negligible as compared to the extent of the body ($O(m)$) – during the entire simulation, which demonstrates a reasonable functional capability of the applied mechanical joint.

4.6 Generic platform with heaving legs

The present validation case refers to a generic platform with two attached legs, which are restricted to heave perpendicularly to the platform. The aim was to verify the implementation of the mechanical joints. As depicted in Fig. 4.11, the platform was exposed to waves and therefore performed a pitch motion. Both legs were coupled to the platform by translational joints. The legs should thus pitch in accord with the platform, but were free to heave independently. The initial position of the two legs at $t = 0s$ can be seen on the right diagram of Fig. 4.12. Furthermore, a constant force was applied to both legs, which cause an additional heaving motion.

In this simulation three overlapping grids containing $2.25 \cdot 10^5$ cells for the background grid and $2 \times 5 \cdot 10^4$ for the foreground grids were used to compute the laminar flow with slip-wall boundary conditions for the verification. The platform's dimension was $15m \times 15m \times 2m$ and the dimension of each leg reads $3m \times 3m \times 15m$. The density of all three bodies was half the density of water. Thus, the three bodies were half submerged in the static calm-water conditions. The wave field was characterized by a wave height and wave length of $H_w = 1.3m$ and $\lambda = 20m$, respectively. A constant force of $F_z = 135kN$ was applied to the local z-axis of both legs. In Fig. 4.12 the pitch and heave motions of the system are presented. As expected, all three bodies performed exactly the same pitch motion. Since the buoyancy forces compensated the external forces acting on the legs, the legs' vertical displacements were gradually diminishing. The legs were initialized in different heights and therefore heaved in shifted phase. The pitch of the platform - and the attached legs - also declined gradually, as expected. Results were all in line with the expectations and indicated the capability of the mechanical model to capture complex relative motions of a coupled multi-body system.

4.7 Seabed penetration of Jackup legs

The last test case is concerned with the leg-seabed interaction. Emphasis is given to the predictive accuracy of the computed seabed reaction force during the penetration of an exemplary leg which featured a diameter of $4.5m$

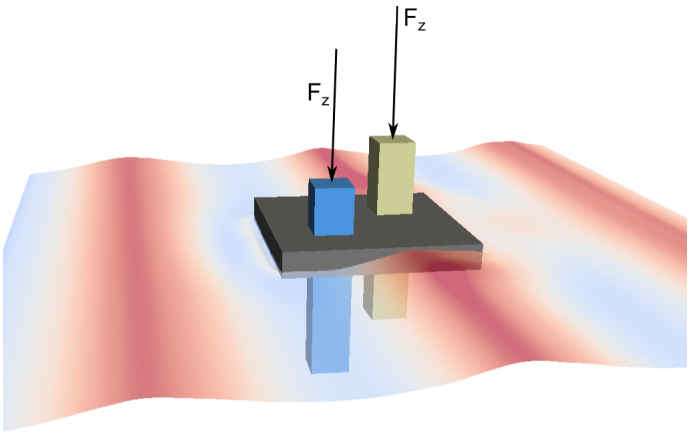

Figure 4.11: *Illustration of a generic platform with heaving legs exposed to waves.*

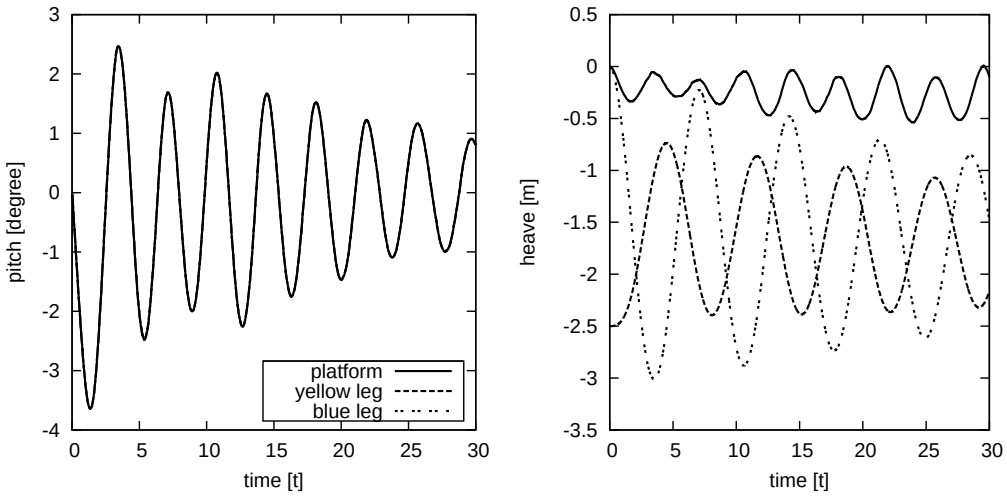

Figure 4.12: *Pitch (left) and heave (right) motion of the platform and its legs in waves.*

and a cone angle of 76°. The leg was penetrated vertically into the superfine silica sand, which is representative for many offshore locations, see Fig. 4.13. Results of the present simulation were compared to reference data taken from [Kreuzer et al., 2014], who employed a Finite Element (FE) method in a Coupled Eulerian-Lagrangian (CEL) framework to investigate the leg-seabed interaction. The CEL FE-method has been successfully used to simulate the penetration process of spudcans or legs into soils [Qiu and Grabe, 2012]. To simulate the behaviour of the soil, a comprehensive hypoplastic model [von Wolffersdorff, 1996] was used by the authors in [Kreuzer et al., 2014].

Table 4.3: *Soil and fender parameters used for the penetration simulation.*

Parameter	**Value**
soil density	$1540 kg/m^3$
internal friction angle	35°
spring stiffness 1	$1.8 \cdot 10^6 N/m$
damping coefficient 1	$1 \cdot 10^5 kg/s$
spring stiffness 2	$4 \cdot 10^6 N/m$
damping coefficient 2	$5 \cdot 10^4 kg/s$

In the present study, the soil phase was modelled as a viscoplastic, incompressible material, which featured a strain rate dependent plastic deformation, cf. 2.3.2. Inherently, the elastic and compressible properties of the soil cannot be considered in this incompressible framework. A remedy to this issue and thereby append reaction forces by reason of compression to the model, was the supplementary use of a combination of linear fenders to the penetrated leg, see Fig. 4.14. The soil resistivity manifests a similar characteristics to that of the fender model, i.e. the reaction force rise when the material gets compressed. Since the seabed reaction force is nonlinear, two fictitious fenders with different spring stiffness were combined to mimic the elastic behaviour of the sand. This way, any seabed composition or desired soil resistivity can be approximated by applying suitable fender parameters, which were assigned and tuned to mimic a certain (previously investigated) soil behaviour. Thus, both soil characteristics, i.e. compressibility and plastic deformation, were covered in this combined approach.

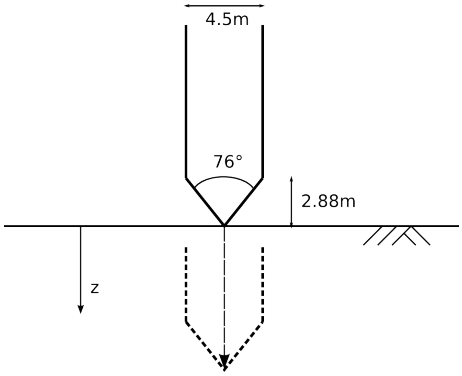

Figure 4.13: *Geometry and penetration path of the leg penetration case.*

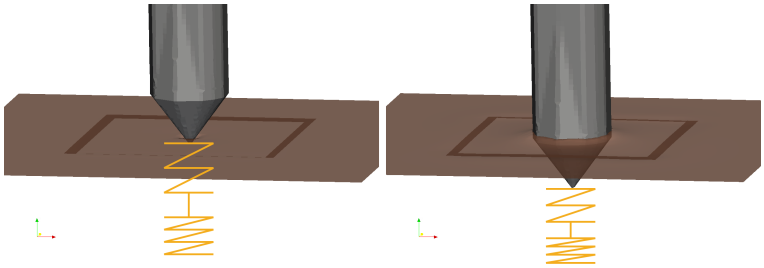

Figure 4.14: *Modelling of the compressible behaviour of the seabed using two linear fenders, which are indicated by using different spring stiffness.*

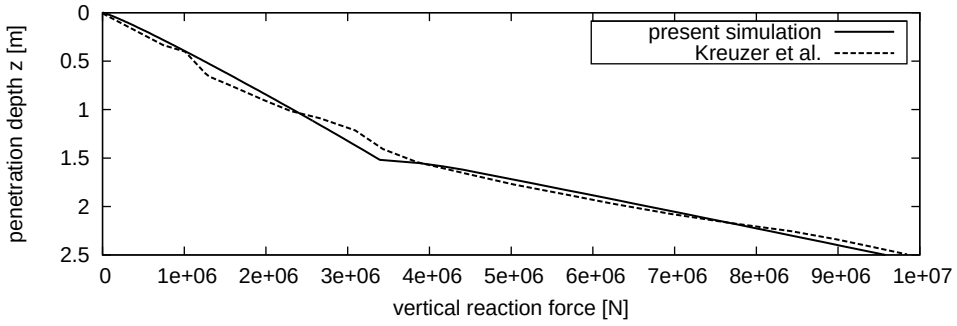

Figure 4.15: *Comparison of predicted vertical reaction forces on the penetrating leg obtained from the present simulation and the FEM-simulations [Kreuzer et al., 2014].*

Figure 4.15 displays a fair predictive agreement between the present cohesionless model (cf. Tab. 4.3) and the reference data provided by [Kreuzer et al., 2014] for vertical reaction forces of the leg. The seabed reaction force progression was thus reasonably reproduced by the combined model.

5 Applications

The application cases presented in the following chapter refer to offshore operations, especially for offshore wind park industries. All simulations were obtained by FreSCo+ using the overset technique on compact computational domains. Examples included involve three phase flows including air/water/soil interactions. A combination of various mechanical joints are employed to model realistic conditions.

5.1 Floating tug

A tug vessel (see Tab. 5.1) served for the validation and application of the coupled computational methods. Simulations of a non-propelled tug in different harmonic waves and encounter angles were compared to measured data reported by the [SVA Potsdam Model Basin, 2013] for a scaling factor of $\Lambda = 16$. Figure 5.1 exemplifies the investigated three validation cases in head, oblique and beam waves. In the computation two overlapping grids containing $5.6 \cdot 10^6$ cells for the foreground grid and $6.3 \cdot 10^6$ cells for the background grid were used for a rather compact domain of $3.5L \times 3L$ in horizontal and lateral direction. The vertical span of the domain was $1.06L$ with the free surface being centred. All degrees of freedom of the vessel other than the motion of interest, i.e. heave ζ, pitch θ and roll ϕ, were suppressed by neglecting the associated accelerations.

Table 5.1: *Dimensions of the full-scale tug.*

$L[m]$	$B[m]$	$D[m]$	$m[kg]$
37.5	14	0.836	1 244 894

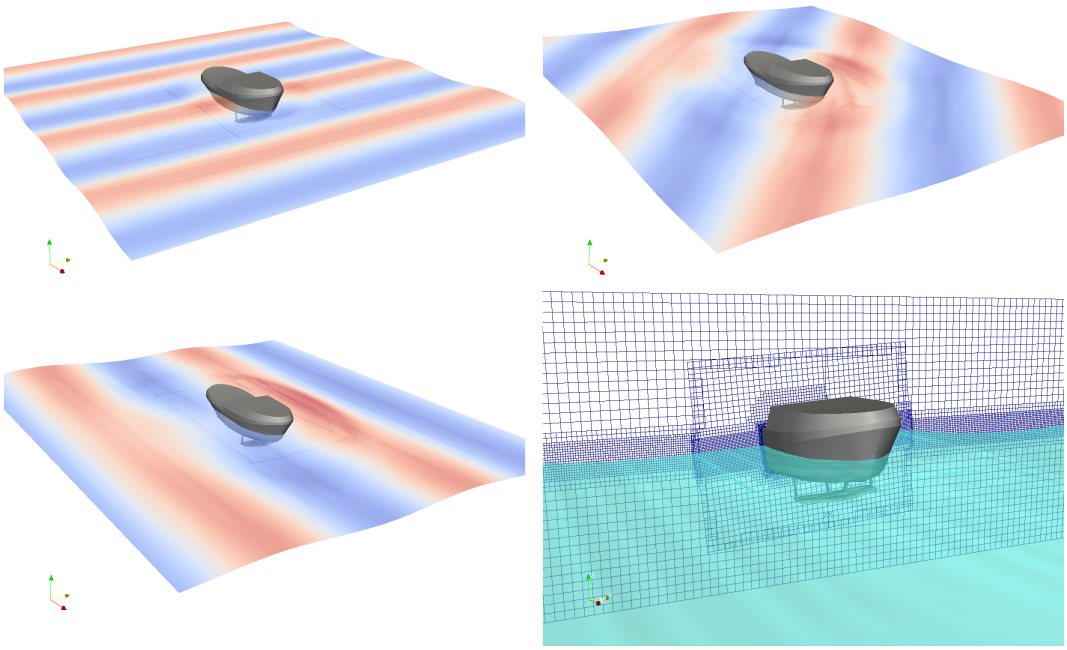

Figure 5.1: *Validation test cases of the tug in head, oblique and beam waves using overset grids.*

In Fig. 5.2 results of head ($\mu = 180°$) and beam waves ($\mu = 90°$) are assessed by a comparison to the associated response-amplitude-operator (RAO) in comparison to measured data. The comparison revealed an encouraging agreement between simulations and experiments. While the calculated heave motion in head waves for the normalised wave length $\lambda/L = 2$ was slightly over-predicted, the agreement of the other motions were much better.

It is noticed that the numerically predicted roll motion in head waves is always close to zero due to the strictly symmetric set-up, which was difficult to maintain during the experiments.

The simulations for encounter wave angles of 135° required specific treatment because of the strong coupling to the yaw motion of the tug. Due to its hull geometry, the tug turned itself into the incoming diagonal waves. Therefore, the yaw motion increased over time and an energy transfer to the other degrees of freedom was experienced. Though, the yaw was suppressed numerically, inherent properties of the quaternion model would still permit small yaw movements

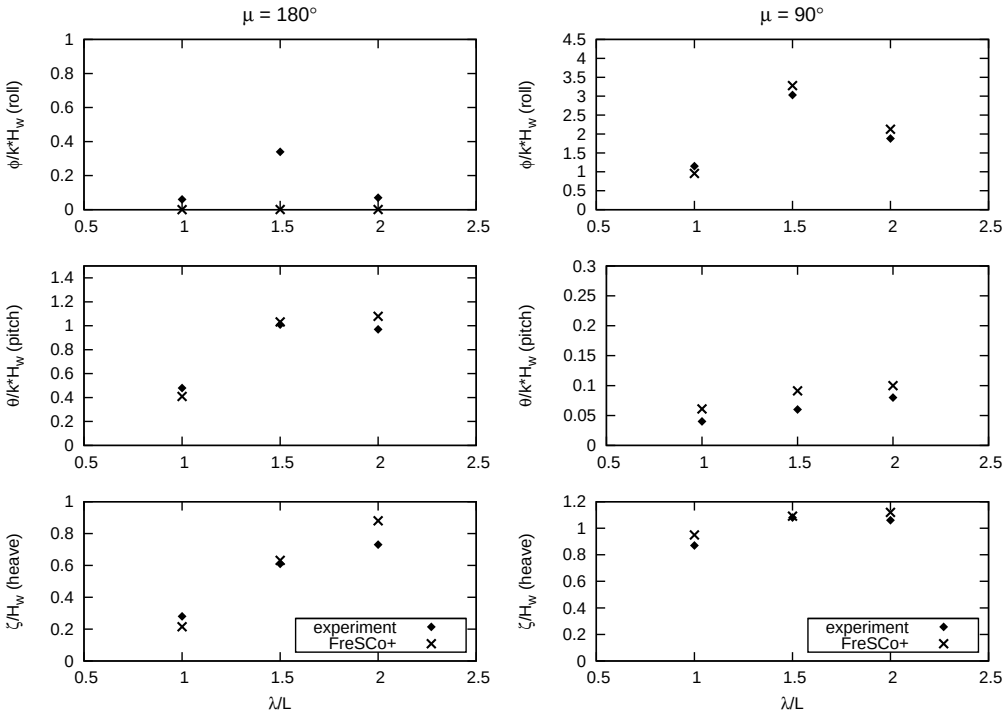

Figure 5.2: *Simulation results of floating tug compared to RAO for head and beam waves.*

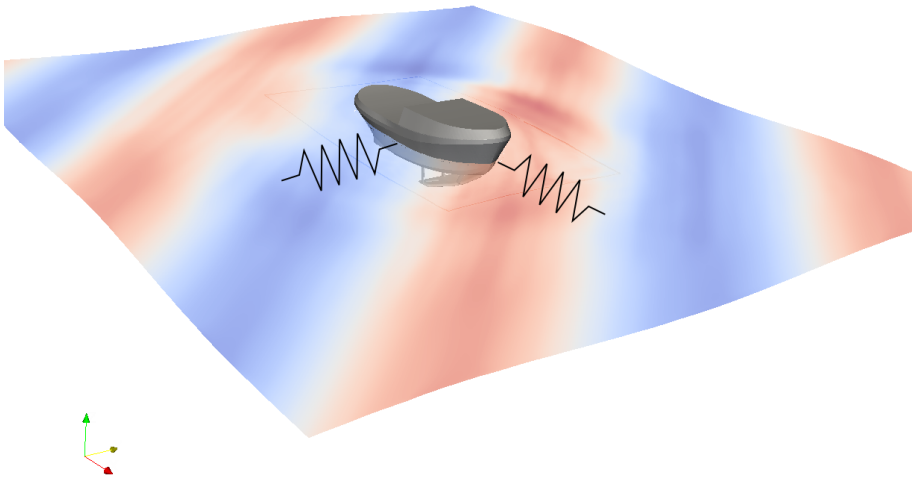

Figure 5.3: *Applying numerical ropes to avoid breaking out of the tug for wave encounter angles* $\mu = 135°$.

in every time step, which would cumulate to larger magnitudes. The experiment actually suffers from similar phenomena.

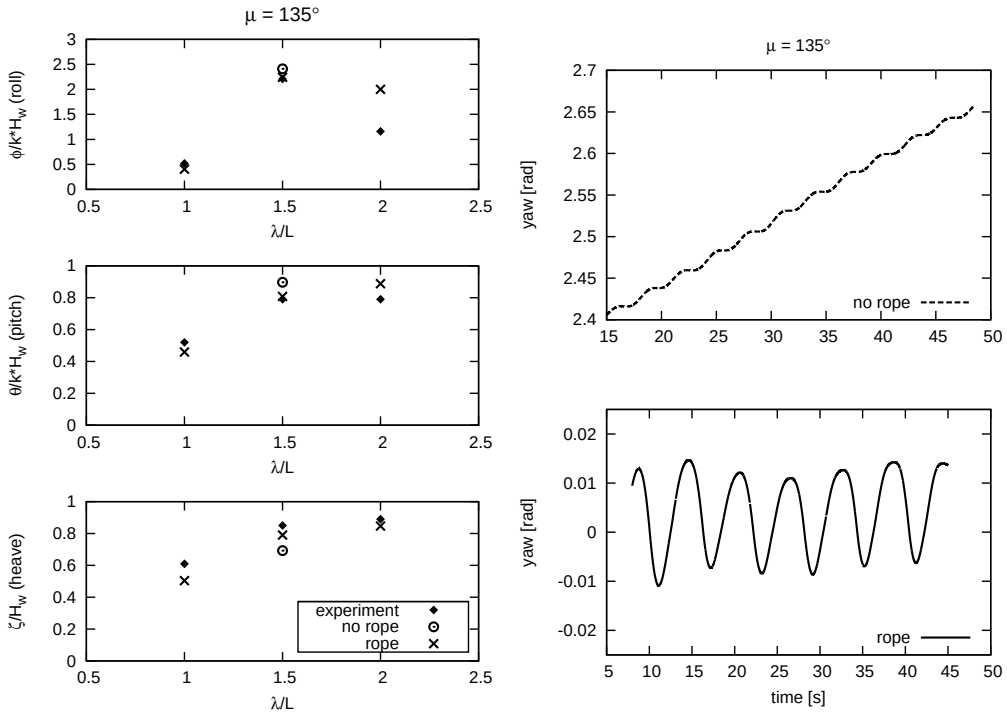

Figure 5.4: *Simulation results of floating tug for $\mu = 135°$ using guidance lines compared to RAO (left). Yaw motion with and without guidance lines (right).*

To measure the heave, pitch and roll motion, the tug was stabilised in the experimental towing tank by using guidance lines. Whenever the tug started to break out of the desired position, it was towed back immediately. For the numerical investigation the same treatment was used by attaching numerical ropes to the tug as illustrated in Fig. 5.3. Using rope parameters of $C = 6.8 \cdot 10^4 N/m$ and $D = 2.9 \cdot 10^5 N \cdot s/m$ reasonable results were obtained. Figure 5.4 (left) demonstrates the improved performance returned by the bonded configuration in comparison with the simulation results of the unbonded case. Due to the use of the numerical ropes, the yaw motion was reduced to the order of $0.01 rad \approx 0.57°$, see Fig. 5.4. Mind that the stabilization of the tug position by guidance lines in the experimental environment is the most difficult for oblique waves. Therefore, discrepancies can easily occur between

measurements and numerical results. The conspicuous deviations between measurements and predictions for the larger wave length $\lambda/L = 2$ displayed in Fig. 5.4 could also result from the combination of the compact numerical grid and the employed incident wave model, in particular the length of the buffer zone and its respective clearance from the vessel. According to [Jacobsen et al., 2012], wave reflections at the buffer zone might occur for buffer zones that are shorter than the length of the vessel, at least for explicit wave models. Other towing application cases have been published in [Rung et al., 2013a] and [Rung et al., 2013b].

5.2 Boatlanding

This application case was concerned with the landing manoeuvre of a catamaran vessel at an offshore foundation using a fender. The aim was to analyse the hydrodynamic effects on the contact between a vessel and a monopile structure. Numerical simulations were compared to experiments published by [González et al., 2015a]. The tests were carried out in a towing tank of $80m$ length, $5m$ width and $2.3m$ depth. The main particulars of the model are listed in Table 5.2, which refers to a geometric scaling factor of $\Lambda = 10$. The vessel was equipped with two propellers and a D-profile fender. As the vessel pushed against the monopile, which was achieved by keeping the thrust on a mean level, the motion of the catamaran and the fender were measured.

Table 5.2: *Dimensions of the catamaran model.*

$L[m]$	$B[m]$	$D[m]$	$m[kg]$
2.2	0.8	0.12	79.2

Table 5.3: *Model parameters used in the simulations.*

Model	$C[\frac{N}{m}]$	$D[\frac{N}{m}s]$	$f_{max}[N]$	μ
I	40 000	500	-	0.7
II	-	-	60	0.7

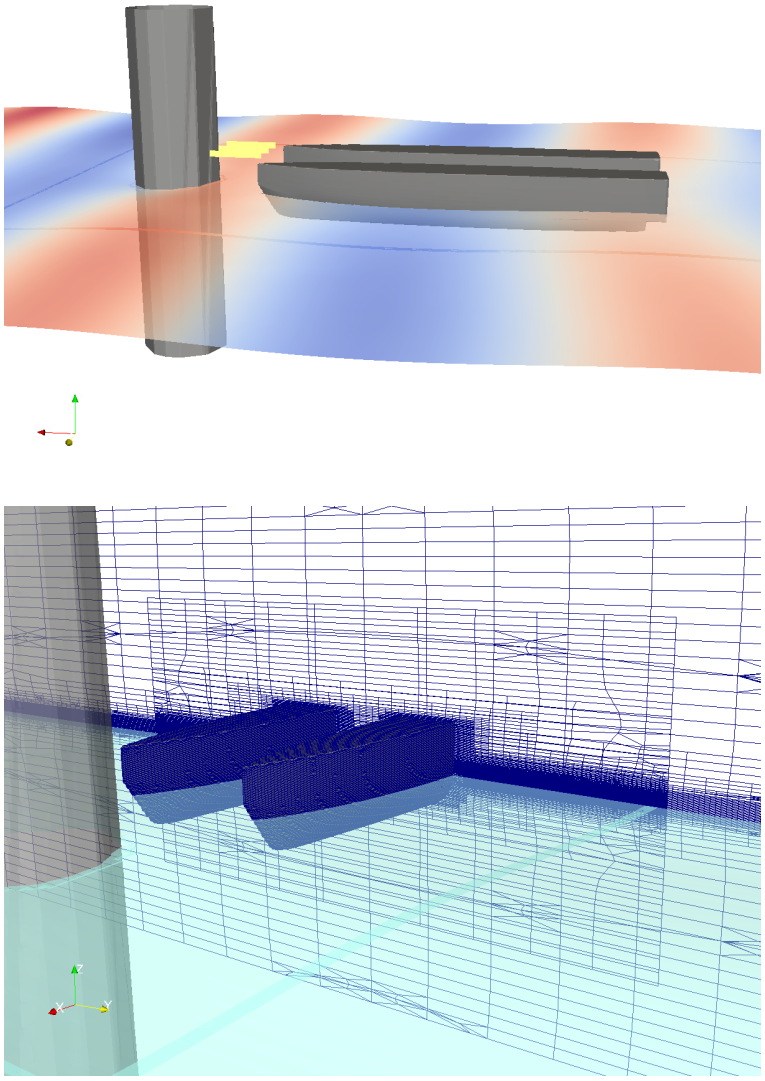

Figure 5.5: *Sketch of the simulation set-up (left) and the employed grids (right) for the boat landing case.*

Figure 5.5 illustrates the set-up and the employed overset grids. The foreground grid contains about $1.7 \cdot 10^6$ cells and the background grid amounts approximately $4.7 \cdot 10^6$ cells. The computational domain had the same size as the towing tank. The propeller thrust was modelled by applying external forces on the body and fender forces were calculated and compared by using the first and the second fender model as described in the section 3.2.2. The response-amplitude-operator for the heave and the pitch motion of the isolated, free floating catamaran is shown in Fig. 5.6.
The agreement between the numerical results and the experimental data is deemed satisfactory. Mind that results refer to a vessel which was not pushing against a monopile. Therefore its motion was not effected by any contact forces and the simulations serve to verify the adequacy of the computational model.

The model parameters of the two fender models used in the boat landing simulations are listed in Tab. 5.3. The simulated motions of the vessel were restricted to surge, heave and pitch. A constant thrust, which agreed with the average value extracted from the measurements, was applied to the body to mimic the propeller force.

Results of the landing manoeuvre in regular waves were compared to the experimental data in Fig. 5.7 for a normalised wave length of $\lambda/L = 1.12$ and a steepness of $H_w/\lambda = 0.0243$. The upper diagram shows the vertical motion ζ_{fen} of the fender and the bottom of the figure reveals the pitch motion θ_{cat} of the catamaran. Both simulations using fender model I and II displayed a good agreement of the predicted amplitudes and frequencies with experimental data.

For further demonstration of the fender's stick and slip behaviour, the manoeuvre was simulated in irregular waves. For this purpose, a JONSWAP-spectrum using a significant wave height of $H_s = 0.08m$ in model scale and a significant period of $T_s = 1.57s$ (Fig. 5.8) was used. According to [Bertram, 2000], 30-100 wave components should be employed for the simulation of the natural seaway in each incident wave direction. Three different discrete realisations of the spectrum using 20, 50 and 80 frequency bins were used for the same grid in the present study. The resolution of the free-surface was chosen in a way that waves with half significant wave height were resolved with about

20 cells, and the peak frequency has been reproduced adequately for all three seaways. Since the waves were superposed in five defined directions, each short crested seaway was therefore composed of 100 (seaway A), 250 (seaway B) or 400 (seaway C) components.

An important aspect refers to the random characteristic of the seaway simulation. To avoid recurrence, frequencies and phases of the superposed wave components were chosen randomly within each discretization and also with respect to their phase within $[0, 2\pi]$, respectively - see Sec. 2.3. Thus, despite the same underlying wave spectrum, different discretizations could lead to different results in such a short-term analysis.

The fender's vertical displacement ζ_{fen} and velocity $\dot{\zeta}_{fen}$ were compared for the three realised seaways. Results displayed in Fig. 5.9 outline that the slip occurred about every 13 seconds for a period of approximately 7 seconds in seaway A, which was attributed to the low resolution. In conjunction with seaway B, three significant slips were recorded at $t = 6s$, $t = 18s$ and $t = 49s$. In seaway C the fender rarely slipped into large amplitudes.

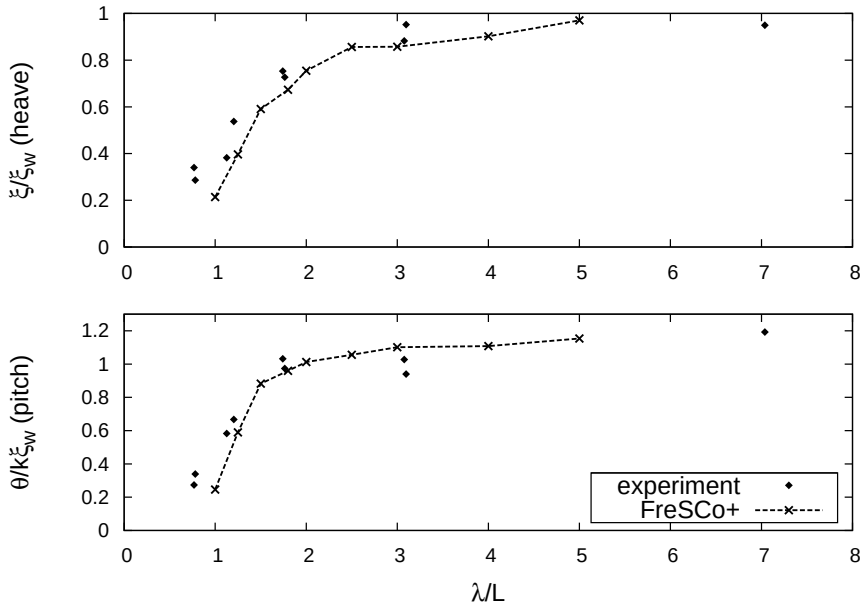

Figure 5.6: *RAO for free floating catamaran in head waves.*

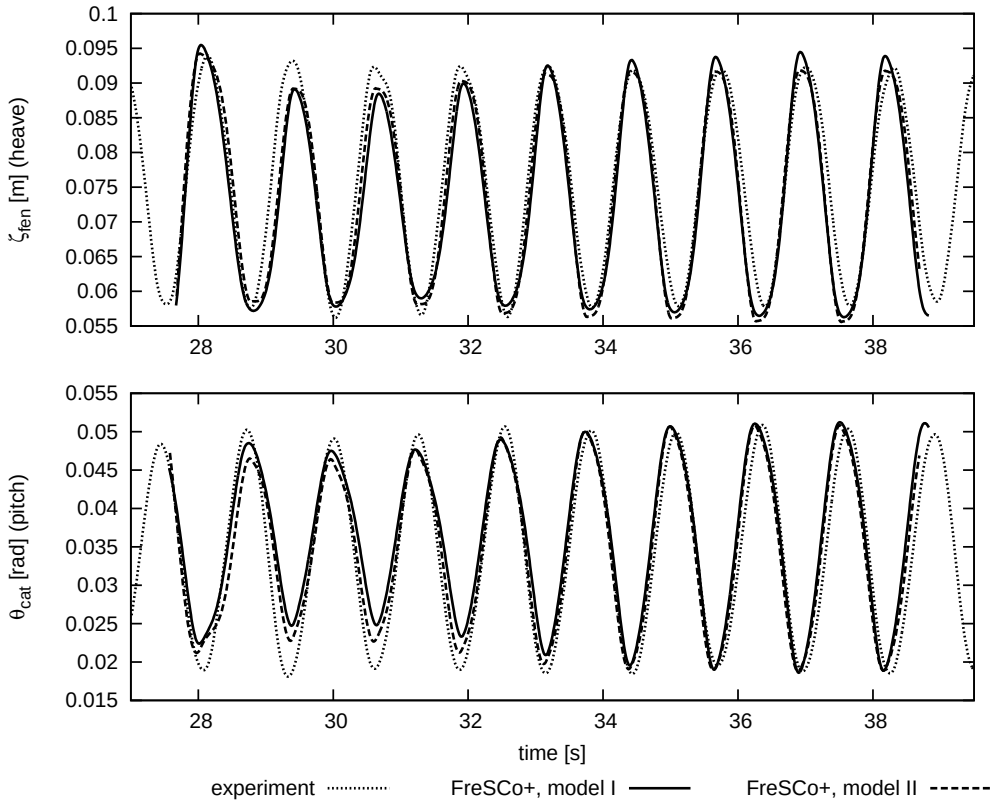

Figure 5.7: *Comparison of predicted and measured time series data of the fender heave motion (top) and catamaran pitch motion (bottom) for the boat landing simulation in regular waves* ($H_w/\lambda = 0.0243m$, $\lambda/L = 1.12$).

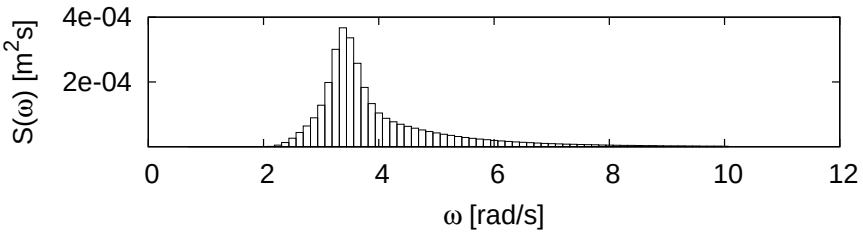

Figure 5.8: *Wave energy distribution used for the seaway generation (discretized in 80 bins).*

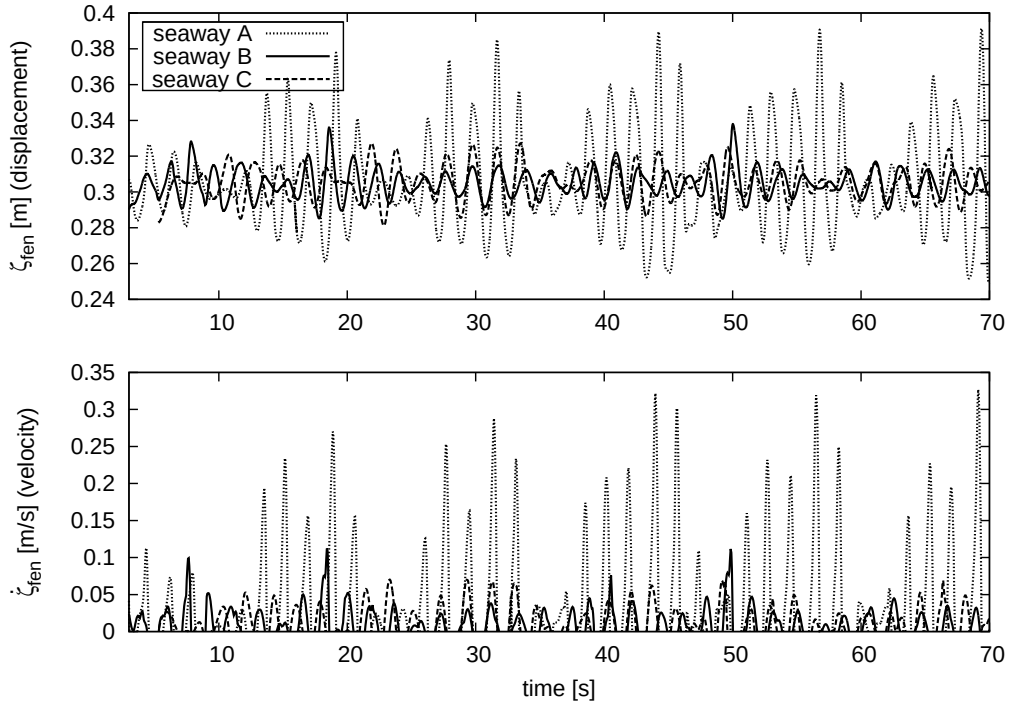

Figure 5.9: *Fender's vertical displacement (upper) and velocity (bottom) during landing manoeuvre in irregular waves.*

5.3 Grounding of gravity foundations

The following test case refers to a shallow water foundation for offshore wind turbines. The structure is usually towed to a desired location and subsequently lowered to the ground by partial flooding, see Fig. 1.1. Figure 5.10 depicts the investigated structure which featured eight symmetrically arranged flooding compartments and a mass of $7315.8\,t$. The overset grids contained $9.2 \cdot 10^5$ cells for the background and $1.35 \cdot 10^6$ cells for the foreground grid. The soil parameters were taken from Tab. 4.3 and the soil was considered to be cohesionless. To ensure a realistic sinkage depth, two fictitious fenders were applied right beneath the surface of the soil phase. Once the bottom of the foundation hit the ground, the fender will be compressed. Without loss of generality, the fender's spring stiffness is assigned to $C_1 = 32 \cdot 10^6 N/m$ and $C_2 = 64 \cdot 10^6 N/m$, the damping coefficients are defined as $D_1 = 16 \cdot 10^5 kg/s$ and $D_2 = 8 \cdot 10^5 kg/s$. Note, that in this application case the fender parameters were chosen to meet desired attributes, i.e. reasonable final sinkage depth preventing long simulation time. In fact, any desired soil resistivity can be applied here.

In the first simulation, no external forces, e.g. induced by towing hawsers were considered. As indicated by Fig. 5.11, the foundation tilted aside during the simulated flooding process. The reason for tilting was the reduction of stability during flooding and a small asymmetry of the discrete model, which is induced by the automated generation of the unstructured mesh. In view of transient inhomogeneous environmental and initial conditions, an asymmetry seems not unrealistic and can harm the operation. To prevent tilting, the foundations are stabilized by towing hawsers of the tugs operating nearby, see Fig. 1.1 (center). Regarding this, four numerical ropes were applied to the foundation's shaft and were bonded to fixed local points in a height of $10.5cm$ above the free-surface. The arrangement of the ropes was in a circular angle of 90° around the foundation, cf. Fig. 5.12. All ropes had a relaxed length of $98.5m$ and the employed rope parameters were $C = 6.7626 \cdot 10^4 N/m$ and $D = 2.9 \cdot 10^5 Ns/m$ for the spring and damping coefficient. In the beginning of the process, the ropes were already strained with an initialised rope length of $99m$. The simulation result by means of the flooding process and the velocity magnitudes inside the foundation at different time steps are shown in Fig. 5.13. As the water penetrated into the flooding compartments, the foundation

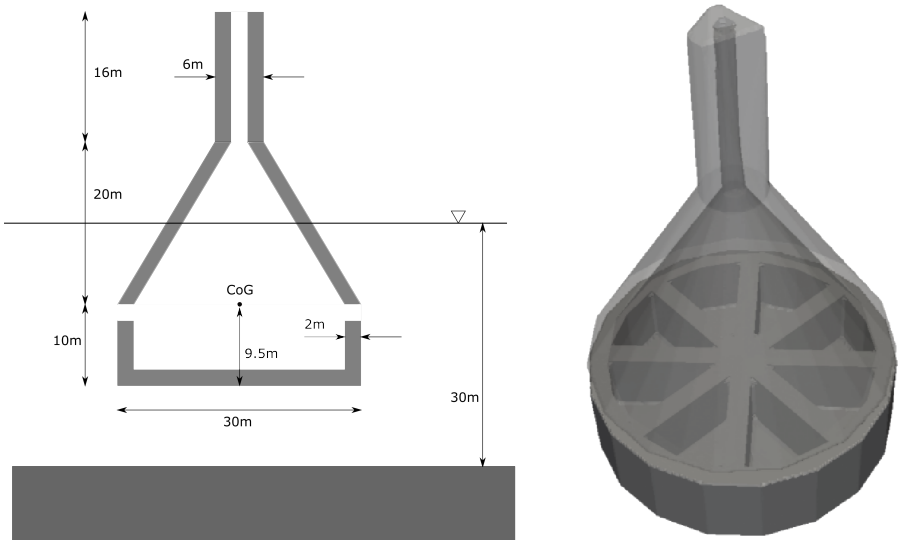

Figure 5.10: *Foundation dimensions and shape for the 3D simulation of the gravity foundation flooding process.*

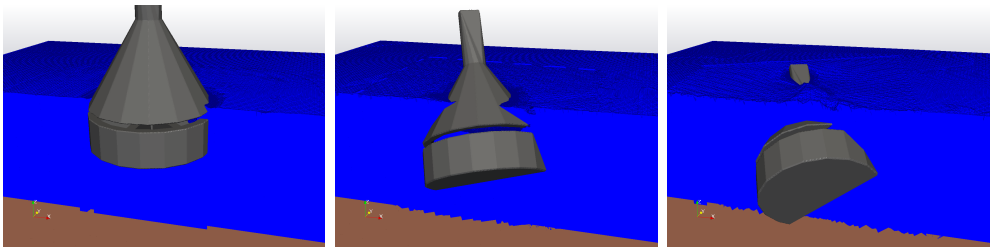

Figure 5.11: *Installation process without towing hawsers: the foundation is tilting due to the asymmetric flooding process.*

began to sink gradually until it hit the ground and was filled up completely. The top diagrams of Fig. 5.14 shows the corresponding motions. The vertical/sinking motion stopped at $21m$, i.e., the foundation subsided $1m$ into the seabed and the vertical velocity vanished as the foundation reached the ground. The rotational motion diagram reveals tilting in x- and y-direction at the time of highest sinking velocity. But this time, the foundation was stabilized by ropes, which can be seen in the bottom diagrams of Fig. 5.14. As expected, during the sinking phase of the foundation the rope forces decreased first, since the ropes got stress relief based on the ropes' arrangement. As soon as the foundation experienced pitch and roll, which led to tilting in the direction of rope 3, rope 2 was tightened again and forces of rope 3 were nearly vanishing. Finally the foundation sank to ground with a small final pitch and roll angle

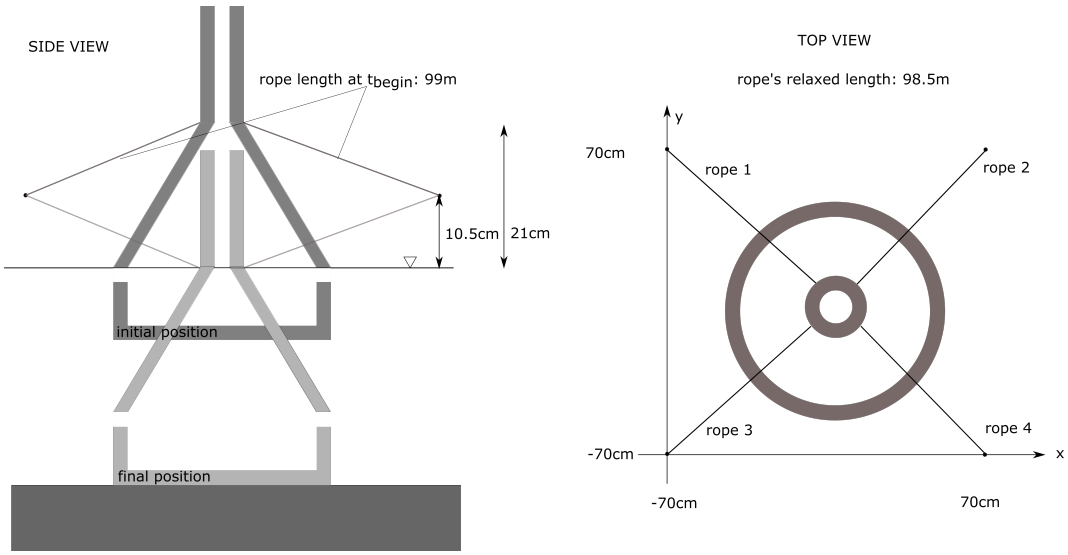

Figure 5.12: *Rope configuration for the installation process using towing hawsers.*

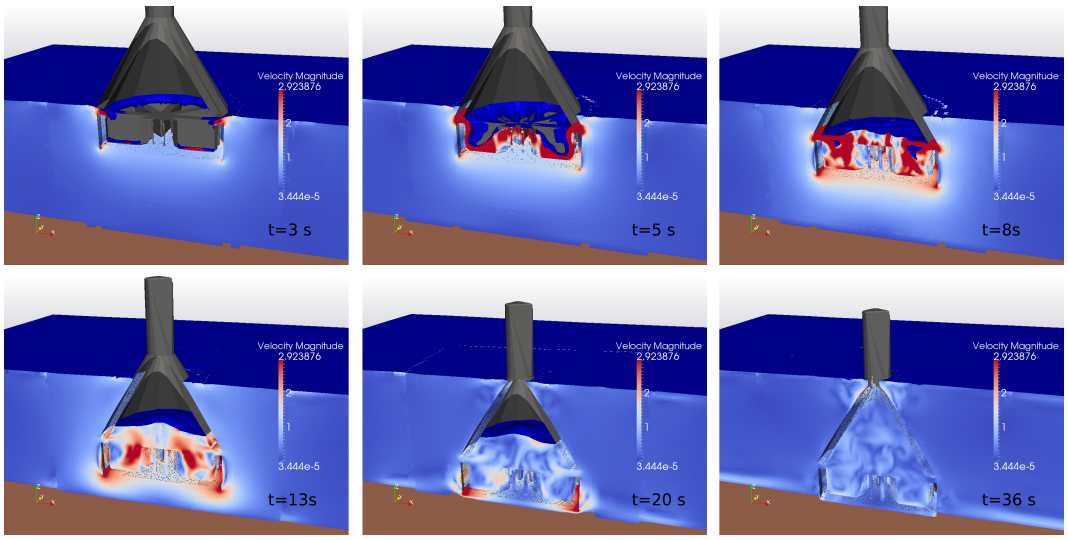

Figure 5.13: *Installation process using towing hawsers: velocity magnitudes inside the foundation at different timesteps.*

of 0.2°, which again strained all ropes. Note that the rope forces are expressed by the magnitudes of the forces. The force discrepancy in the final process was dominated by vertical components. Figure 5.15 depicts the velocity distribution in the installation process. The sinking motion induced translational velocities under the foundations bottom, i.e., in the suspension layer to the soil phase, which leads to a soil bulge around the foundation base.

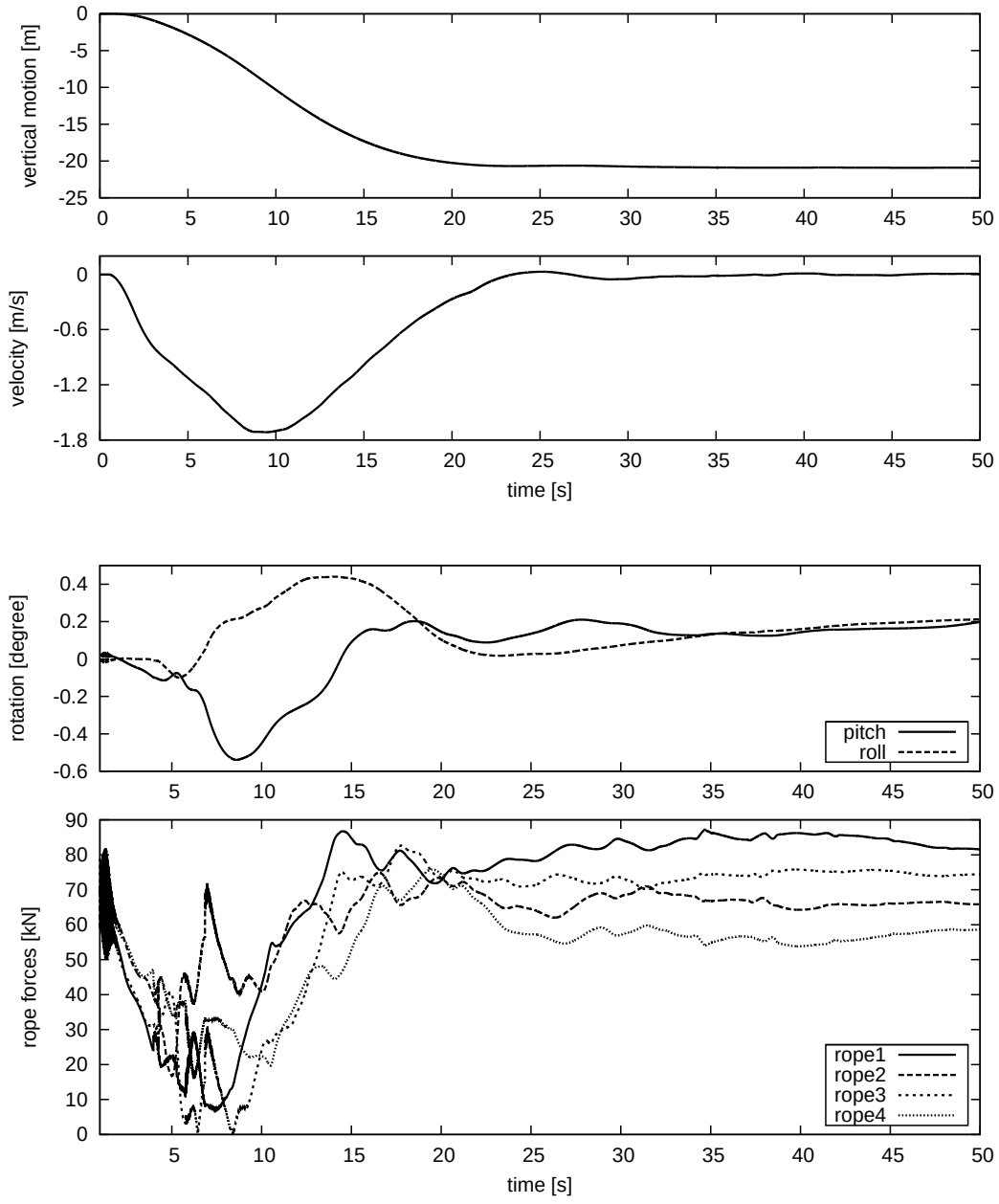

Figure 5.14: *Foundation grounding case: vertical motion, vertical velocity, as well as rotational motion and rope forces during the installation process.*

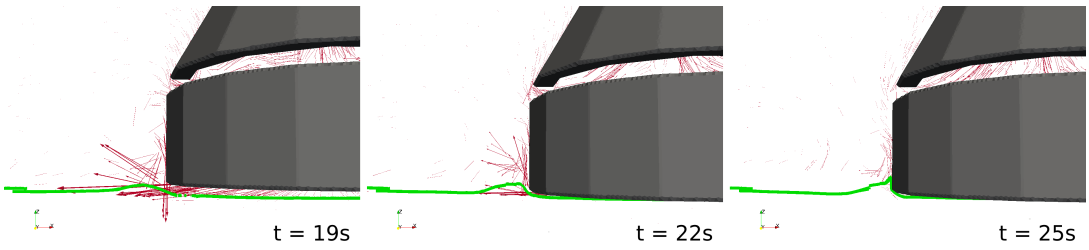

Figure 5.15: *Velocity distribution and soil bulge around the foundation.*

5.4 Jack-up elevation in seaway

The final application is concerned with the hydrodynamic performance during the installation process of a generic jack-up vessel. The aim was to analyse the hydrodynamic forces acting on the vessel and to examine potential operational limits. Herein, all components of the computational model were combined. Regarding the safety of the crew during operations, roll motion and large accelerations should be avoided.

Elevation process in natural seaway

The first investigations were concerned with the elevation process of the generic jack-up vessel [Kreuzer et al., 2014] depicted in 5.16. The main dimensions of the considered geometry are given in Tab. 5.4. Herein, VCG denotes the vertical distance from baseline to the center of gravity, which is horizontally at amidships. The jack-up consisted of a main platform, which had translational joints to its four legs. The employed coupling allowed the legs to move only perpendicular to the ships longitudinal axis. To lower the legs in reality, they are flooded and additionally pushed down by a hydraulic system. Since the flooding of the legs is not of interest, the simulation can be simplified by adding a time dependent mass conditioned by the lowering depth of the legs. This mimics a water flux that scales with the vertical motion.

$$m(t) = m_0 + \int \dot{m}\, dt = m_0 + \rho_w \cdot A_{wl} \cdot \int \dot{z}(t)\, dt = m_0 + \rho_w \cdot A_{wl} \cdot z(t). \quad (5.1)$$

Herein, m_0 denotes the initial mass of the leg, ρ_w is the water density and A_{wl} describes the leg's water line area. The time dependent vertical position of the leg's center of gravity refers to $z(t)$.

Figure 5.16: *Generic jack-up vessel.*

Six grids were used for this turbulent flow overset simulation. The background grid contained $8 \cdot 10^6$, the platform had $5 \cdot 10^6$ and each leg counted $2.62 \cdot 10^5$ cells. A fully developed JONSWAP spectrum of 200 wave components using $H_s = 2m$ and $T_s = 5s$ was applied. The extent of the compact computational domain is $200m \times 300m$ and the water depth was $30m$. The initial positions of the legs were assigned to $5m$ above the seabed. To model the compressibility of the seabed, additional fenders were applied to the penetration area of each leg, cf. Sec. 3.3. The fenders act right beneath the seabed surface. As soon as each single leg hit the ground, the fenders will be compressed. Without loss of generality, each fender's spring stiffness denotes to $C_1 = 35 \cdot 10^6 N/m$ and $C_2 = 80 \cdot 10^6 N/m$, the damping coefficients are $D_1 = 20 \cdot 10^5 kg/s$ and $D_2 = 20 \cdot 10^5 kg/s$. Again, note that any desired soil resistivity/characteristic can be applied here. For this application, the given combination were chosen for reasonable sinkage depth.
After the legs penetrated into the soil, the main ship lifted itself up to a given

Table 5.4: *Dimensions of the generic jack-up vessel for numerical investigations.*

$length$	$breadth$	$draught$	$length_{leg}$	$diameter_{leg}$	$mass$	VCG
$130m$	$36m$	$6m$	$60m$	$5m$	$24\,614t$	$5m$

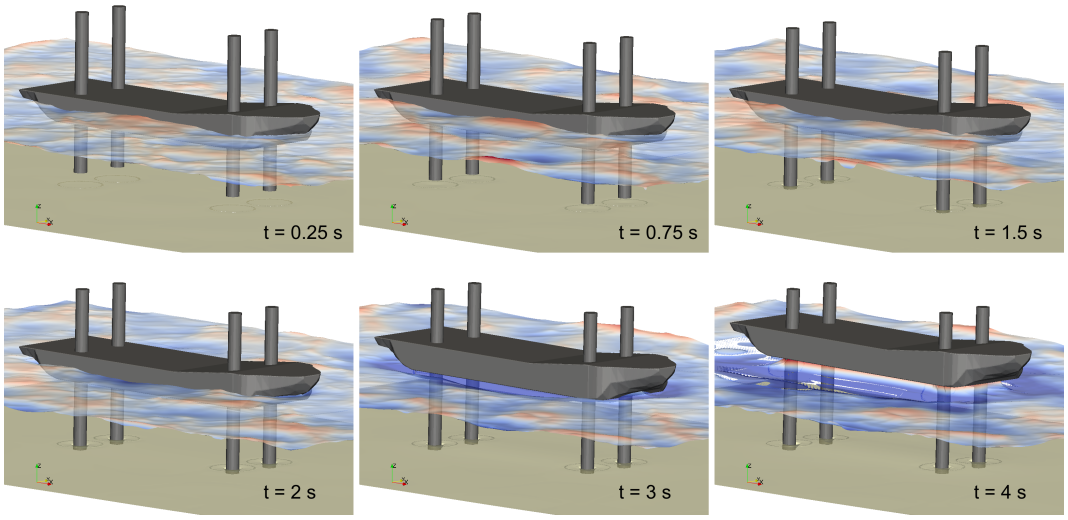

Figure 5.17: *Three phase overset simulation (air, water and soil) of a generic jack-up vessel and its elevation process in natural seaway: leg flooding/lowering* $(0.25s-1.5s)$*, seabed penetration* $(2s)$ *and platform elevation* $(3s-4s)$.

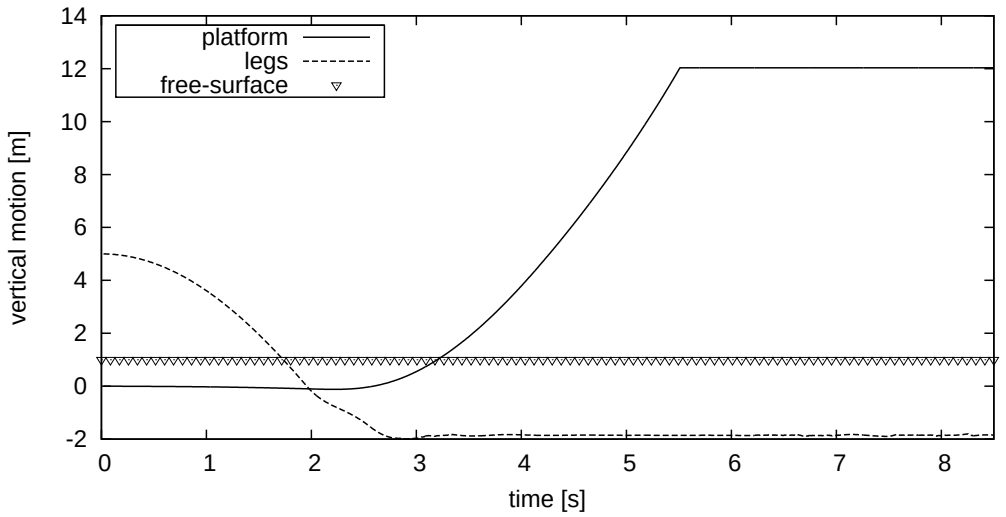

Figure 5.18: *Vertical motion of the jack-up vessel and its legs during elevation process.*

height by adding a ramp force to the platform and correlating moments at the leg joint positions to ensure stability. While the platform was lifting up, the legs experienced supplementary stability forces by the weight of the platform. Fig. 5.17 illustrates the overall jacking procedure of a generic jack-up vessel in a natural seaway and Fig. 5.18 shows the corresponding vertical motion of the platform and the legs. Mind that actual leg velocities typically refer to $1.2m/min$ and the legs were lowered much faster in the present study. Due to the flooding the legs hit the seabed for the first time at $t = 2s$ and come at rest at a penetration depth of $2m$, while the platform started to jack up itself to a defined height of $12m$. The jacking forces, which lifted up the platform, were also applied to all legs in the opposite direction. These forces and induced moments contribute to the stability of the vessel. Due to a draught of $6m$, an air gap of $5m$ was achieved at the end.

Loads on the platform

The final investigations refer to the loads on the platform due to beam waves. Therefore, the jack-up vessel was exposed to harmonic waves of same wave length $\lambda = 35m$ and wave height of $H_w = 6m$ during the elevation process. The wave crest was supposed to hit the platform before the legs reach the ground, at the time of the penetration and after the legs already dived into the seabed. Therefore three different phases $\varphi_1 = 12.07$, $\varphi_2 = 10.74$ and $\varphi_3 = 9.41$ were of particular interest.

Fig. 5.19 exemplifies the free-surface elevation at $t = 1.5s$, when a wave crest reached the platform. Fig. 5.20 compares the lateral forces of the beam waves for different wave phases, as well as the corresponding roll moments and roll motion of the vessel. The maximum amplitudes of the hydrodynamic forces and moments acting on the vessel were assigned to the wave impacts. Since the bulk of the vessel was submerged in water at the time of impact for all three cases, the platform got excited and hence, performed a roll motion. In the case of φ_1 the roll motion was exclusively dominated by hydrodynamic forces. For φ_2 and φ_3 the legs already had contact to the ground. Thus, the wave impact forces could cause a tilting of the vessel by the down jacked legs during subsequent lowering, which was rather a mechanical effect. In these cases safe working condition is not assured and jacking would not be performed. Mind

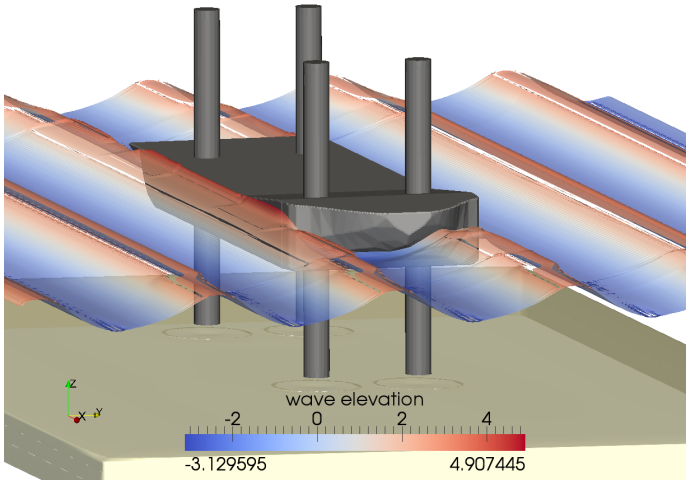

Figure 5.19: *Load investigation on jack-up platform: wave impact at* $t = 1.5s$ *for wave phase* φ_1.

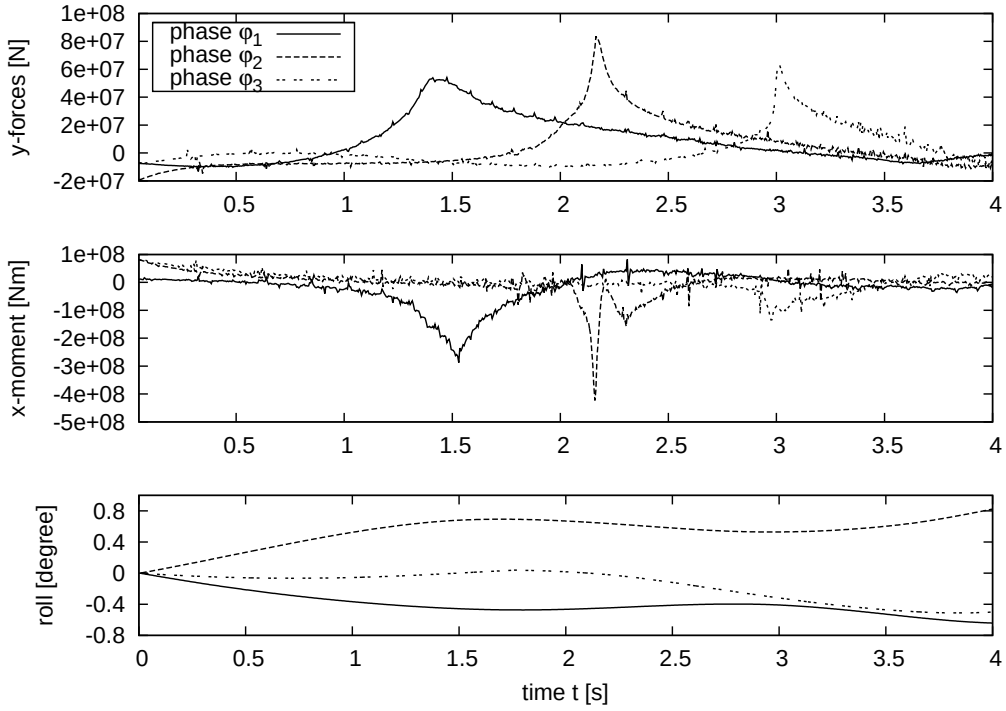

Figure 5.20: *Computed lateral forces, roll moments and roll motion experienced by the investigated platform during elevation for different wave phases.*

that a critical significant wave height for jacking operation is typically $2.5m$ maximum [Swire Blue Ocean, 2013], [Öster, 2016]. These cases illustrated and predicted the hydrodynamic performance of jack-up rigs in extreme seaway conditions.

6 Summary and Perspectives

In this thesis the development and application of mechanically coupled bodies in seaway and multi-phase environments are presented. The hydrodynamic effects on multi-body systems have been analysed in simulations of complex offshore installation procedures, while taking into account the dynamics of three phases, i.e., air, water and soil.

The numerical treatment of the Reynolds-averaged-Navier-Stokes equations for the incompressible viscous flow simulation is carried out by use of the Finite-Volume method. Turbulent flows are modelled by the $k-\omega$ turbulence model and the free-surface is determined by the Volume-of-Fluid method. Implicit seaway boundary conditions, which combine viscous solutions in the near-field and inviscid solutions in the far-field, were used to avoid undesirable reflections from the boundaries and allowed for the use of relatively compact domain sizes and variable headings against the incident wave. To overcome the challenge of large relative motions in a multi-body set-up, implicitly coupled overset-grids with multiple overlapping layers were applied. A motion module based on the quaternion formulation, which aimed to avoid the effect of the Gimbal Lock, including constraint conditions and models of several basic mechanical joint elements have been successfully implemented. With the help of the mechanical joints, three-phase flow simulations including (rigid) structure-seabed interactions have been modelled. The characteristics of the seabed can be modelled by using a combination of linear fenders and a soil model, in which the seabed is treated as a visco-plastic fluid with a variable viscosity. Followed by a yield criterion, the granular soil phase manifests a strain-rate driven deformation if a certain yield stress is achieved.

The algorithm was successfully validated and verified against numerical and experimental reference data. Particular interest was directed to simulation cases

involving mechanical joints. Examples included refer to a sliding wedge, which was modelled by the 6DoF motion module using a translational joint. Seabed penetration of Jackup legs involving granular soil was investigated. Fair to satisfactory agreement was obtained through out all investigations. Thus, the procedure is shown to be capable of predicting body motions, body forces and fluid forces with encouraging accuracies.

Finally, combining and utilizing all features of the computational framework in the application to full scale two- or three-phase simulations, application cases including wave tests of a floating tug, which had to be stabilized by numerical ropes, boat landing manoeuvres using fenders for safe transfer, installation process of a gravity foundation and a jack-up rig to study safety margins were analysed. The aim is to investigate the entire operation/installation process within one simulation, including rigid structure motions in irregular waves and seabed penetration. The results indicate that the combination of generic mechanical joints between multiple moving objects and overset-grid methods in a multi-phase environment are a viable option to analyse complex hydrodynamic scenarios at reasonable computational costs if a short-time analysis is sufficient.

Future investigations could involve numerical analysis of maneuvering in confined water, which is important for ships opertating amongst others in harbours or channels. The effect on ship motion is crucial for safety and optimum work flow. By the use of the implemented methods and mechanical joints, simulations on the dynamics of mooring systems [Wilke, 2003] or hydrodynamic loads on tugs in escort operations [Artyszuk, 2014] are attractive and feasible. The latter is commonly investigated using fixed yaw angles [Jahra et al., 2015]. With the present module, loads and flow patterns near escort tugs can be examined dynamically. Further interest could be directed towards crane/heavy-lift operations on sea [Cha et al., 2010], [Halse et al., 2014]. Swinging of suspended loads or even loss of loads have big impact of the ship motion and stability, thus dynamic response simulations are essential.

Concerning physical modelling, the implementation of a dynamic tensor of inertia would be desirable. In the present procedure a body with multiple moving parts, e.g. jackup vessel with moving legs, is modelled as a system of coupled bodies with separate constant tensor of inertia assigned to each moving part.

For more violent motions one time dependent inertia assigned to the complete system would be valuable for its dynamic description. Considering the seabed model, elastic reaction forces can be obtained by the supplemented fender combination, if the penetration direction is known. The contour of a realistic seabed is uneven and can have different inclinations. Thus, one-dimensional reaction forces could be inaccurate. A more flexible model capable of treating different penetration angles should be investigated.

Further attention should be turned to an increase of computational performance. To gain meaningful results, long time simulations are beneficial. The present code is already parallelized and efficient in its CPU performance, but could be improved with a adequate GPGPU implementation.

This thesis demonstrates the applicability of the procedure for the simulation of multi-body hydrodynamic problems. The use of appropriate combinations of mechanical joints allows not only to analyse the consequences of holonomic constraints, but also to supplement a soil model in an incompressible flow solver. The procedure can serve as an attractive tool for a wide range of applications.

Bibliography

[Artyszuk, 2014] Artyszuk, J. (2014). Steady-state Manoeuvring of a Generic ASD Tug in Escort Pull and Bow-rope Aided Push Operation. *International Journal on Marine Navigation and Safety of Sea Transportation*, 8:449–457.

[Balay et al., 1997] Balay, S., Gropp, W. D., McInnes, L. C., and Smith, B. F. (1997). Efficient Management of Parallelism in Object Oriented Numerical Software Libraries. *Modern Software Tools in Scientific Computing*, pages 163–202.

[Barnes et al., 1989] Barnes, H. A., Hutton, J. F., and Walters, K. (1989). *An introduction to rheology*, volume 3. Elsevier.

[Bauchau, 2011] Bauchau, O. A. (2011). *Solid Mechanics and Its Applications: Flexible Multibody Dynamics*. Springer-Verlag.

[Baumgarte, 1972] Baumgarte, J. (1972). Stabilization of constraints and integrals of motion in dynamical systems. *Computer Methods in Applied Mechanics and Engineering*, 1:1–16.

[Bertram, 2000] Bertram, V. (2000). *Practical Ship Hydrodynamics*. Butterworth Heinemann, Oxford.

[Bienen and Cassidy, 2006] Bienen, B. and Cassidy, M. J. (2006). Advances in the three-dimensional fluid-structure-soil interaction analysis of offshore jack-up structures. *Marine Structures*, 19(2):110–140.

[Bienen et al., 2015] Bienen, B., Qiu, G., and Pucker, T. (2015). CPT correlation developed from numerical analysis to predict jack-up foundation penetration into sand overlying clay. *Ocean Engineering*, 108:216–226.

[Böbs, 2013] Böbs, A. (2013). *Belastung vertäuter Schiffe durch vorbeifahrende Schiffe in engem Fahrwasser*. Diploma thesis, Hamburg University of Technology.

[Bölle, 2014] Bölle, T. (2014). *Simulation eines generischen Jackup-Vorgangs in einem RANSE Verfahren*. Bachelor thesis, Universität Hamburg-Harburg.

[Brunswig et al., 2014] Brunswig, J., Matin, F., Luo, X., and Rung, T. (2014). *TUG-Design - Entwicklung eines Entwurfsverfahrens für kleine völlige Schiffe unter Berücksichtigung des Seegangsverhaltens, Teilvorhaben: TUG-HYDRO-Design - Viskose Mehrkörper-Hydrodynamik für Offshore-Schlepper im Seegang : Abschlussbericht zum Forschungsvorhaben*. Technische Universität Hamburg-Harburg, Institut für Fluiddynamik und Schiffstheorie. DOI: 10.2314/GBV:837850606.

[Brunswig and Rung, 2011] Brunswig, J. and Rung, T. (2011). RANS Simulations using Overset Meshes. In *4th International Conference on Computational Methods in Marine Engineering*, Lisbon, Portugal.

[Cha et al., 2010] Cha, J.-H., Roh, M.-I., and Lee, K.-Y. (2010). Dynamic response simulation of a heavy cargo suspended by a floating crane based on multibody system dynamics. *Ocean Engineering*, 37:1273–1291.

[Choi and Hong, 2002] Choi, Y. R. and Hong, S. Y. (2002). An Analysis of Hydrodynamic Interaction of Floating Multi-Body Using Higher-Order Boundary Element Method. In *The Twelfth International Offshore and Polar Engineering Conference*, Kitakyushu, Japan. International Society of Offshore and Polar Engineers.

[Clauss et al., 1988] Clauss, G., Lehmann, E., and Oestergaard, C. (1988). *Meerestechnische Konstruktionen*. Springer-Verlag, Berlin, Heidelberg.

[Clauss and Jacobsen, 2005] Clauss, G. F. and Jacobsen, K. (2005). Multibody Systems in Waves - Impact of Hydrodynamic Coupling on Motions. In *12th International Congress of the International Maritime Association of the Mediterranean (IMAM)*, Lisbon, Portugal.

[DNV, 1996] DNV (1996). *Guidelines for Offshore Structural Reliability-Application to Jackup Structures*.

[DNV, 2012] DNV (2012). *Recommended Practice-Self-elevating Units.*

[Faltinsen, 1990] Faltinsen, O. M. (1990). *SEA LOADS ON SHIPS AND OFFSHORE STRUCTURES.* Cambridge University Press.

[Feikens et al., 2011] Feikens, H., Verwey, R., Serraris, J., and Huijsmans, R. (2011). Wet handshake: Workability study of an offshore thruster exchange operation. In *ASME 30th International Mechanical Engineering Congress & Exposition*, Denver, Colorado, USA.

[Ferrant et al., 2003] Ferrant, P., Gentaz, L., Allesandrini, B., and Touze, D. L. (2003). A Potential/RANSE Approach for Regular Water Wave Diffraction about 2-d Structures. *Ship Technology Research*, 50(4):165–171.

[Ferziger and Peric, 2002] Ferziger, J. H. and Peric, M. (2002). *Computational Methods for Fluid Dynamics.* Springer-Verlag.

[Fitriadhy et al., 2011] Fitriadhy, A., Yasukawa, H., and Masaki, Y. (2011). SLACK TOWLINE ON TOW-TOWED SHIPS INTERACTION DURING MANEUVERING. In *2nd International Conference on Ship Manoeuvring in Shallow and Confined Water: Ship to Ship Interaction*, Trondheim, Norway.

[Fraccarollo and Capart, 2002] Fraccarollo, L. and Capart, H. (2002). Riemann wave description of erosional dam-break flows. *Journal of Fluid Mechanics*, 461:183–228.

[Gentaz et al., 2004] Gentaz, L., Allesandrini, B., Ferrant, P., and Luquet, R. (2004). Numerical Simulation of the 3D Viscous Flow around a Vertical Cylinder in non-linear Waves using Explicit Incident Wave Model. In *International Conference on Offshore Mechanics and Acrtic Engineering*, Vancouver, Canada.

[GleisteinRopes, 2014] GleisteinRopes (2014). *GeoMarine - Ropes for commercial marine.* Geo. Gleistein und Sohn GmbH, http://www.gleistein.com/de-geo-marine/.

[Goldstein, 2006] Goldstein, H. (2006). *Klassische Mechanik.* John Wiley & Sons.

[González et al., 2015a] González, D. F., König, M., Abdel-Maksoud, M., and Düster, A. (2015a). Simulation of Safety-Relevant Situations regarding the Interaction of Service Ships with Offshore Wind Turbine Plants. In *34th International Conference on Ocean, Offshore and Arctic Engineering (OMAE)*, St John's, Newfoundland, Canada.

[González et al., 2015b] González, D. F., Loebus, S., and Abdel-Maksoud, M. (2015b). Application of a boundary element method for hydrodynamic simulations of landing manoeuvres at an offshore foundation. In *9th International Workshop on Ship and Marine Hydrodynamics (IWSH)*, Glasgow, UK.

[Hadzic, 2006] Hadzic, H. (2006). *Development and Application of Finite Volume Method for the Computationof Flows Around Moving Bodies on Unstructured, Overlapping Grids.* 633 Schriftenreihe Schiffbau, TU Hamburg-Harburg.

[Hafermann, 2007] Hafermann, D. (2007). The new RANSE Code FreSCO for Ship Applications. *Jahrbuch der Schiffbautechnischen Gesellschaft*, 101:103–109.

[Halse et al., 2014] Halse, K. H., Æsøy, V., Ponkratov, D., Chu, Y., Xu, J., and Pedersen, E. (2014). Lifting Operations for Subsea Installations Using Small Construction Vessels and Active Heave Compensation Systems: A Simulation Approach. In *ASME: 33rd International Conference on Ocean, Offshore and Arctic Engineering*, volume 1A: Offshore Technology, San Francisco, California, USA. Ocean, Offshore and Arctic Engineering Division.

[Hess and Smith, 1967] Hess, J. L. and Smith, A. (1967). Calculation of potential flow about arbitrary bodies. *Progress in Aerospace Sciences*, 8:1–138.

[Hirt and Nichols, 1981] Hirt, C. W. and Nichols, B. D. (1981). Volume of fluid (VOF) method for the dynamics of free boundaries. *Journal of Computational Physics*, 39(1):201–225.

[Jacobsen, 2005] Jacobsen, K. (2005). *Hydrodynamisch gekoppelte Mehrk"orpersysteme im Seegang - Bewegungssimulationen im Frequenz- und Zeitbereich.* PhD thesis, Technische Universit"at Berlin.

[Jacobsen et al., 2012] Jacobsen, N. G., Fuhrmann, D. R., and Fredsœ, J. (2012). A wave generation toolbox for the open-source CFD library: OpenFoam®. *International Journal for Numerical Methods in Fluids*, 70:1073–1088.

[Jahra et al., 2015] Jahra, F., Islam, M., Thanyamanta, W., and Molyneux, D. (2015). Investigation of Hydrodynamic Loads and Flow Patterns Near an Escort Tug in Oblique Flows. *ASME. International Conference on Offshore Mechanics and Arctic Engineering*, 7.

[Jensen and Capul, 2006] Jensen, J. J. and Capul, J. (2006). Extreme response predictions for jack-up units in second order stochastic waves by FORM. *Probabilistic Engineering Mechanics*, 21(2):330–337.

[Josse et al., 2011] Josse, T., Billet, A., and Leen, S. (2011). Prediction of supply vessel motion during transfer to a fixed structure. In *ASME 30th International Mechanical Engineering Congress & Exposition*, Denver, Colorado, USA.

[Journeé, 1992] Journeé, J. (1992). *Experiments and Calculations on 4 Wigley Hull Forms in Head Waves.* Report; Delft University of Technology, Ship Hydromechanics Laboratory.

[Kang et al., 2016] Kang, W., Zhang, C., and Yu, J. (2016). Stochastic extreme motion analysis of jack-up responses during wet towing. *Ocean Engineering*, 111:56–66.

[Klemt, 2004] Klemt, M. (2004). *Bewegungssimulation schwimmender Körper in viskoser Strömung.* 630 Schriftenreihe Schiffbau, TU Hamburg-Harburg.

[Koliha, 2011] Koliha, N. (2011). *Entwicklung eines 6DOF-Moduls auf Basis von Quaternionen zur Simulation freier Bewegungen schwimmender Körper.* Bachelor thesis, Hamburg University of Technology.

[Kraskowski, 2009] Kraskowski, M. (2009). Validation of the RANSE Rigid Body Motion Computations. In *12th Numerical Towing Tank Symposium*, Cortona, Italy.

[Kreuzer et al., 2014] Kreuzer, E., Solowjow, E., Qiu, G., Hamann, T., and Grabe, J. (2014). Leg-seabed Interactions of Jack-up Vessels due to Motions

in irregular Waves. In *ASME 33rd International Conference on Ocean, Offshore and Arctic Engineering (OMAE)*, San Francisco, USA.

[Leonard, 1979] Leonard, B. (1979). A stable and accurate convective modelling procedure based on quadratic upstream interpolation. *Computer Methods in Applied Mechanics and Engineering*, 19(1):59–98.

[Liu et al., 2005] Liu, P. L.-F., Wu, T.-R., Raichlen, F., Synolakis, C. E., and Borrero, J. C. (2005). Runup and rundown generated by three-dimensional sliding masses. *Journal of Fluid Mechanics*, 536:107–144.

[Luo et al., 2012] Luo, X., Brunswig, J., Manzke, M., Koliha, N., Matin, F., Janssen, C. F., and Rung, T. (2012). Analyses of Coupled Floating Bodies in Seaway. In *2nd International Conference on Violent Flows*, Nantes, France.

[Luo-Theilen and Rung, 2017] Luo-Theilen, X. and Rung, T. (2017). Computation of mechanically coupled bodies in a seaway. *Journal of Ship Technology Research*, 64:129–143.

[Luo-Theilen and Rung, 2019] Luo-Theilen, X. and Rung, T. (2019). Numerical analysis of the installation procedures of offshore structures. *Ocean Engineering*, 179:1.

[Luquet et al., 2007] Luquet, R., Ducrozet, G., Gentaz, L., Ferrant, P., and Allesandrini, B. (2007). Applications of SWENSE method to seakeeping simulations in irregular waves. In *9th Internatinal Conference on Numerical Ship Hydrodynamics*.

[Magnus and Müller, 1990] Magnus, K. and Müller, H. H. (1990). *Grundlagen der Tehnischen Mechanik*. Teubner, Stuttgart.

[Manners and Rainey, 1992] Manners, W. and Rainey, R. C. T. (1992). Hydrodynamic Forces on Fixed Submerged Cylinders. *Proceedings: Mathematical and Physical Sciences*, 436:13–32.

[Marckmann, 2013] Marckmann, H. (2013). *Entwicklung und Implementierung eines Simulationsverfahrens zur effizienten Berechnung von schwimmenden Körpern in Seegang*. Master thesis, Hamburg University of Technology.

[Mierke, 2012] Mierke, D. (2012). *Simulation der Bewegung mechanisch gekoppelter schwimmender Körper mit Hilfe von Quaternionen in einem RANSE-Verfahren.* Bachelor thesis, Hamburg University of Technology.

[Mirzadeh et al., 2016] Mirzadeh, J., Kimiaei, M., and Cassidy, M. J. (2016). Performance of an example jack-up platform under directional random ocean waves. *Applied Ocean Research*, 54:87–100.

[Moctar et al., 2010] Moctar, O., Shigunov, V., Kaufmann, J., and Schellin, T. E. (2010). Computations for Seakeeping of an Offshore Supply Vessel and Loads on a Jack-Up Platform. *Jahrbuch der Schiffbautechnischen Gesellschaft*, 104:191–201.

[Moran, 1984] Moran, J. (1984). *An Introduction to Theoretical and Computational Aerodynamics.* John Wiley & Sons, New York.

[Nair and Kanso, 2007] Nair, S. and Kanso, E. (2007). Hydrodynamically coupled rigid bodies. *Journal of Fluid Mechanics*, 592:393–411.

[Nikravesh, 1988] Nikravesh, P. E. (1988). *Computer-Aided Analysis of Mechanical Systems.* Prentice-Hall, New Jersey, USA.

[Nikravesh et al., 1985a] Nikravesh, P. E., Wehage, R. A., and Kwon, O. K. (1985a). Euler Parameters in Computational Kinematics and Dynamics. Part 1. *Journal of Mechanisms, Transmissions and Automation in Design*, 107:358–365.

[Nikravesh et al., 1985b] Nikravesh, P. E., Wehage, R. A., and Kwon, O. K. (1985b). Euler Parameters in Computational Kinematics and Dynamics. Part 2. *Journal of Mechanisms, Transmissions and Automation in Design*, 107:366–369.

[Öster, 2016] Öster, H. (2016). *New Generation Jack-up Vessel.* Wartsila SP a Tw Wind HPTIV. www.scribd.com (call in Nov 2016).

[Patankar, 1980] Patankar, S. V. (1980). *Numerical Heat Transfer and Fluid Flow.* Hemisphere Publishing Corporation, New York.

[Qiu and Grabe, 2012] Qiu, G. and Grabe, J. (2012). Numerical investigation of bearing capacity due to spudcan penetration in sand overlying clay. *Canadian Geotechnical Journal*, 49:1393–1407.

[Radhakrishnan and Hindmarsh, 1993] Radhakrishnan, K. and Hindmarsh, A. C. (1993). *Description and Use of LSODE, the Livermore Solver for Ordinary Differential Equations*. LLNL report UCRL-ID-113855.

[Reynolds, 1895] Reynolds, O. (1895). On the Dynamical Theory of Incompressible Viscous Fluids and the Determination of the Criterion. *Philosophical Transactions of the Royal Society of London*, 186:123–164.

[Rung, 2008] Rung, T. (2008). *Numerische Methoden der Thermofluiddynamik 2 (CFD2)*. Inst. Fluid Dynamics and Ship Theory, Hamburg University of Technology.

[Rung et al., 2013a] Rung, T., Luo, X., and Matin, F. (2013a). Multi-body Hydrodynamics using Parallel Overset-Grid Technique. In *V International Conference on Computational Methods in Marine Engineering*, Hamburg, Germany.

[Rung et al., 2013b] Rung, T., Ulrich, C., and Luo, X. (2013b). Multi-body Hydrodynamics for Offshore Applications using Advanved Viscous Flow Simulation Techniques. In *Conference on Maritime Energy*, Hamburg, Germany.

[Rung et al., 2009] Rung, T., Wöckner, K., Manzke, M., Stück, A., Brunswig, J., and Ulrich, C. (2009). Challenges and Perspectives for Maritime CFD Applications. *Jahrbuch der Schiffbautechnischen Gesellschaft*, Vol. 103.

[Simonsen et al., 2008] Simonsen, C., Otzen, J., and Stern, F. (2008). EFD and CFD for KCS Heaving and Pitching in Regular Head Waves. In *27th Symposium on Naval Hydrodynamics*, Seoul, Korea.

[SVA Potsdam Model Basin, 2013] SVA Potsdam Model Basin (2013). *Seakeeping Tests for a Voith Water Tractor*. Report; SVAtech GmbH.

[Swire Blue Ocean, 2013] Swire Blue Ocean (2013). *Windfarm Installation Vessels (WIVs). Pacific Orca & Pacific Osprey*. Technical Specifications.

[Tajali and Shafieefar, 2011] Tajali, Z. and Shafieefar, M. (2011). Hydrodynamic analysis of multi-body floating piers under wave action. *Ocean Engineering*, 38(17-18):1925–1933.

[Thomsen, 2012] Thomsen, K. (2012). *Offshore Wind. A Comprehensive Guide to Successful Offshore Wind Farm Installation.* Academic PressElsevier Inc.

[Trelleborg Marine Systems, 2017] Trelleborg Marine Systems (2017). *Fender Systems.* Product Brochure.

[Ulrich et al., 2013] Ulrich, C., Leonardi, M., and Rung, T. (2013). Muli-Physics SPH Simulation of Complex Marine-Engineering Hydrodynamic Problems. *Ocean Engineering*, 64:109–121.

[Ulrich and Rung, 2012] Ulrich, C. and Rung, T. (2012). A Simple SPH Model of Water-Soil Interaction in Porous Media. In *7th International SPHERIC Workshop*, Prato, Italy.

[Völkner, 2013] Völkner, S. (2013). *Modellierung granularer Bodenphase in maritimen Mehrphasensimulationen.* Master thesis, Hamburg University of Technology.

[Völkner et al., 2017] Völkner, S., Brunswig, J., and Rung, T. (2017). Analysis of non-conservative interpolation techniques in overset grid finite-volume methods. *Computers and Fluids*, 148:39–55.

[Völkner et al., 2015] Völkner, S., Wriggers, W. R., Luo-Theilen, X., and Rung, T. (2015). An Overset-Grid Three-Phase Flow Model for Offshore Operations. In *VI International Conference on Computational Methods in Marine Engineering*, Rome, Italy.

[von Wolffersdorff, 1996] von Wolffersdorff, P.-A. (1996). A hypoplastic relation for granular material with a predefined limitstate surface. *Mechanics of Cohesive-frictional Materials*, 1:251–271.

[Wang et al., 2005] Wang, J., Li, J., Cai, X., Tian, M., and Hao, J. (2005). Hydrodynamic interactions between two bodies in waves in 3D timedomain. *Journal of Marine Science and Application*, 4:15–20.

[Wilcox, 1988] Wilcox, D. C. (1988). *Turbulence Modeling for CFD.* DCW Industries.

[Wilke, 2003] Wilke, U. (2003). *Untersuchungen zur Dynamik verankerter meerestechnischer Systeme*, volume 18:286. VDI Verlag.

[Wittenberg, 2008] Wittenberg, J. (2008). *Dynamics of Multibody Systems*. Springer-Verlag.

[Wöckner et al., 2010] Wöckner, K., Drazyk, W., and Rung, T. (2010). An Efficient VOF-Based RANS Method to Capture Complex Sea States. In *29th International Conference on Ocean, Offshore and Arctic Engineering (OMAE)*, Shanghai, China.

[Woernle, 2011] Woernle, C. (2011). *Mehrkörpersysteme - Eine Einführung in die Kinematik und Dynamik von Systemen starrer Körper*. Springer-Verlag.

ISBN: 978-3-89220-721-4